تركيب الرقيم السومري للنشر والتوزيع

2026

المؤتمر العلمي الدولي الثاني الدوري الموسوم: من الأصالة الإنسانية إلى آفاق الابتكار والحداثة العلمية

جمع نخبة عالمية لتوظيف البحث العلمي في المزاوجة بين الأصالة المعرفية والابتكار التقني خدمةً للتنمية المستدامة والإنسان.

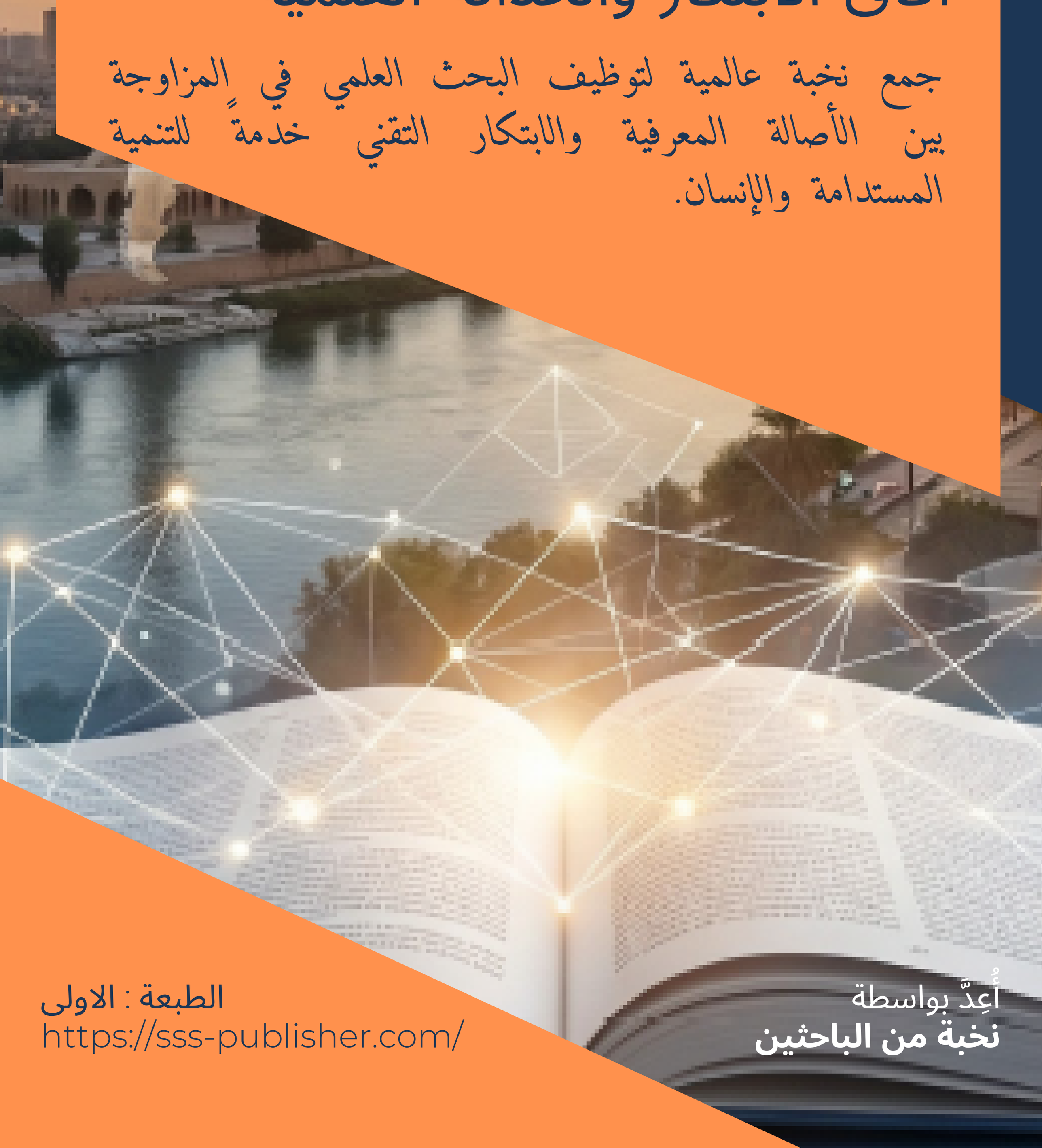

الطبعة : الاولى
https://sss-publisher.com/

أُعِدَّ بواسطة
نخبة من الباحثين

المؤتمر العلمي الدولي الثاني الدوري الموسوم: من الأصالة الإنسانية إلى آفاق الابتكار والحداثة العلمية

(الجزء الثالث):

المؤتمر العلمي الدولي الثاني الدوري الموسوم: من الأصالة الإنسانية إلى آفاق الابتكار والحداثة العلمية :(الجزء الثالث)

نخبة من الباحثين

التصنيف : العلوم الصرفة والتطبيقية والهندسة

رقم الايداع في دار الكتب والوثائق في بغداد (بلا) لسنة (بلا)

ISBN: 978-9922-7962-15

DOI: 10.62909/978.9922.7962.15

دار تركيب الرقيم السومري للطباعة والتوزيع والنشر الالكتروني

العراق – ديالى – بعقوبه – شارع الاوقاف

هاتف : 07775262892

manager@sss-publisher.com

المؤتمر العلمي الدولي الثاني الدوري
الموسوم: من الأصالة الإنسانية إلى آفاق الابتكار والحداثة العلمية :(الجزء الثالث)

نخبة من الباحثين

2026

تنضيد الكتاب

معهد الترجمة والكتاب

«ماليزيا»

مراجعة لغوية

الدكتور محمد محمد كاظم

«العراق»

تصميم الغلاف

معهد التكنالوجيا

«الهند»

التوزيـــع والنشـــر الإلكترونـــي ، تمـــت فهرســـة هـــذا الكتـــاب فـــي عـــدد مـــن الفهارس والمنصات الدولية، منها:

كروس ريف	(CrossRef)
أوبن ألكس	(OpenAlex)
مؤشر الاقتباس المفتوح الأوكراني	(OUCI)
سجل مستودعات الوصول المفتوح	(ROAR)
سيمنتك سكولار	(Semantic Scholar)
دايمنشنز	(Dimensions)
ريسرش غيت	(ResearchGate)
فات كات	(Fatcat)
المعيار الدولي للترقيم	(IAS)
مؤشر الاستشهاد العلمي	(SCI)
أوركيد	(ORCID)
سايليت	(Scilit)

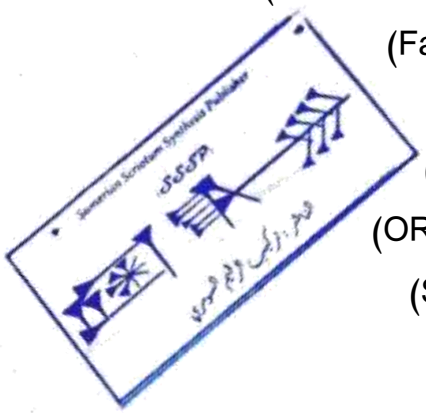

الموقع الرسمي لدار النشر الرقيم السومري للنشر والتوزيع

يتوفر هذا الكتاب عبر الموقع الرسمي لدار النشر، مع تخصيص مُعرّف رقمي دائم (DOI) خاص به: https://doi.org/10.62909/978.9922.7962.15

978-9922-7962-15

المؤتمر العلمي الدولي الثاني الدوري

الموسوم: من الأصالة الإنسانية إلى آفاق الابتكار والحداثة العلمية

برعاية كريمة وبإشراف السادة الأفاضل:

الأستاذ الدكتور أسامة إسماعيل المشهداني رئيس جامعة نينوى.

الأستاذ الدكتور كوسار محمد علي رئيس جامعة السليمانية.

الأستاذ الدكتور وسام صلاح عبد الحسين رئيس جامعة قرطبة.

الأستاذ الدكتور حاتم هذال عبدالحميد مدير عام دائرة البحوث والدراسات.

الأستاذ رباح إبراهيم آل جعفر مدير عام دائرة التعليم الديني والدراسات الإسلامية.

الأستاذ الدكتور صالح عبد المهدي الخالدي عميد كلية ابن خلدون الجامعة.

الأستاذة الدكتورة سوزان صابر حيدر عميد كلية الإدارة والاقتصاد - جامعة السليمانية.

الدكتور علي مهدي كاظم عميد كلية العلوم - جامعة قرطبة.

الدكتور علاء ثابت جاسم رئيس مؤسسة أجيال الرافدين لتطوير التعليم.

الأستاذ المساعد الدكتور علي عبودي نعمة المدير التنفيذي لمؤسسة أجيال الرافدين لتطوير التعليم.

الدكتور أحمد جميل مجيد المدرس مدير مركز وعي للاستشارات وبناء القدرات.

ديباجة المؤتمر

انطلاقاً من الدور المحوري للبحث العلمي ونشر الأبحاث العلمية في معالجة القضايا الراهنة وتقديم الحلول المستقبلية وسعياً نحو تعزيز الحوار الأكاديمي البنّاء بين مختلف التخصصات يسرنا أن نعلن عن عقد هذا المؤتمر العلمي الدولي. يهدف المؤتمر إلى جمع نخبة من الباحثين والأكاديميين من مختلف أنحاء العالم لتبادل الرؤى والخبرات العلمية والبحث في كيفية المزاوجة بين "الأصالة الإنسانية" التي تمثل الجذور المعرفية العميقة وبين "آفاق الابتكار" التي تفرضها متطلبات الحداثة العلمية والتقنية إن هذا المحفل العلمي يسعى لتجسير الفجوة بين التراث المعرفي والتقنيات المعاصرة لخلق توازن يدعم التنمية المستدامة ويواجه التحديات العالمية بمنظور علمي مبتكر يضع الإنسان وقيمه في صلب التطور التكنولوجي.

الجهات الراعية والمنظمة للمؤتمر

سينعقد المؤتمر في رحاب كلية ابن خلدون الجامعة في العراق – بغداد بالتعاون مع جامعة نينوى وجامعة السليمانية وجامعة قرطبة ودائرة البحوث والدراسات ودائرة التعليم الديني والدراسات الإسلامية ودار نور العلم للطباعة والنشر والتوزيع – إربد الأردن ومركز الخيمياني للتدريب والاستشارات – العقبة الأردن ومركز وعي للاستشارات وبناء القدرات ومؤسسة أجيال الرافدين لتطوير التعليم - العراق للفترة (٢٣ – ٢٤ / ٨ / ٢٠٢٦) حضورياً + عن بُعد (أون لاين).

أهداف المؤتمر

١. استعراض ومناقشة أحدث الدراسات والبحوث العلمية الرصينة في مختلف حقول المعرفة واستثمار نتائجها في معالجة القضايا المعاصرة.
٢. إبراز الدور الفاعل للتبادل المعرفي والمنهجي بين مختلف مجالات الاختصاص وتوظيفه كأداة استراتيجية لمواجهة التحديات العالمية الراهنة واستشراف المستقبل.
٣. تشجيع الباحثين على إجراء الدراسات البينية والمتكاملة وتوظيف تكامل العلوم التطبيقية مع التخصصات الأخرى؛ بهدف كسر العزلة بين العلوم وإنتاج معرفة مبتكرة تقدم حلولاً عملية للمشكلات المعقدة.
٤. توفير بيئة علمية تفاعلية رصينة للباحثين لنشر نتاجاتهم الفكرية وأبحاثهم الأصيلة ذات القيمة المضافة والارتقاء بها وفقاً لمعايير جودة النشر العالمي.
٥. مد جسور التواصل الفعّال والتعاون المشترك بين المؤسسات الأكاديمية والبحثية على الصعيدين المحلي والدولي وتأسيس شبكات بحثية مستدامة لتبادل الخبرات والرؤى.
٦. الخروج برؤى وتوصيات علمية وعملية قابلة للتطبيق تسهم في رفد مؤسسات الدولة والمجتمع بالحلول الناجعة وتدعم صناع القرار في رسم السياسات العامة.

محاور المؤتمر

١. العلوم القانونية والسياسية.
٢. العلوم الإدارية والاقتصادية.
٣. الدراسات الإنسانية والعلوم الإسلامية وحوار الحضارات.
٤. الإعلام والاتصال وتكنولوجيا المعلومات الرقمية.
٥. الجغرافيا والتاريخ والدراسات التراثية والسياحية.
٦. العلوم التربوية والنفسية والاجتماعية والفلسفية وطرائق التدريس.
٧. اللغات والآداب والترجمة.
٨. الفنون الجميلة وفلسفة التصميم والجماليات.
٩. التربية البدنية وعلوم الرياضة.
١٠. علوم الحاسبات والعلوم الصرفة والذكاء الاصطناعي والدراسات البينية.
١١. تكامل العلوم التطبيقية مع العلوم الإنسانية والاجتماعية والتقنية.
١٢. آفاق البحث العلمي والابتكار المعرفي في مختلف التخصصات العلمية.

ضوابط المشاركة والنشر

١. يجب أن تتماشى البحوث مع منهجية البحث العلمي المتعارف عليها.
٢. ألا يكون البحث قد نُشر سابقاً أو عُرض في مؤتمر آخر.
٣. تُقبل البحوث باللغتين العربية أو الإنجليزية ويُشترط في البحث المقدم أن يكون أصيلاً ولم يسبق نشره أو تقديمه لأي جهة أخرى بالتزامن مع إرساله للمؤتمر.
٤. تخضع جميع الأبحاث المُقدمة لفحص مبدئي لنسبة الاستلال عبر برنامج (Turnitin) ويجب ألا تزيد نسبة الاستلال عن ٢٠%.
٥. يجب أن تتضمن واجهة البحث باللغتين العربية والإنجليزية عنوان البحث وأسماء الباحثين والانتساب المؤسسي (القسم الكلية الجامعة البلد) والبريد الإلكتروني.
٦. يجب أن يتضمن البحث ملخصاً وافياً باللغتين العربية والإنجليزية في حدود ٢٥٠ كلمة تتبعه مباشرة كلمات مفتاحية لا تقل عن ٣ ولا تزيد عن ٥ كلمات.
٧. يُستخدم نوع الخط (Times New Roman) ويكون حجم خط المتن ١٤ ونسبة التباعد بين الأسطر ١.٥.
٨. يُشترط التزام الباحثين بقواعد التوثيق العلمي في المتن وإعداد قائمة المراجع النهائية وفقاً لنظام (APA)
٩. من الضروري الالتزام التام بالسلامة اللغوية وخلو النص من الأخطاء الإملائية والنحوية لتكون لغة البحث رصينة وسليمة تماماً.
١٠. تُرسل الملخصات البحثية للمشاركة سواء كان الباحث ينوي النشر أو الاكتفاء بالمشاركة فقط على أن تتضمن الصفحة الأولى بيانات الباحث كاملة.

رسوم المشاركة

- **رسوم المشاركة (أون لاين):** 75,000 دينار عراقي (بدون نشر بحث).
- **رسوم المشاركة (حضورياً):** 100,000 دينار عراقي (بدون نشر بحث).
- **نشر البحث (اختياري حسب رغبة الباحث وليس اجباري):** 100,000 دينار تضاف إلى رسوم المشاركة أعلاه ويتم النشر في كتاب الوقائع الذي يحمل ترقيماً دولياً (ISBN) ومعرفاً رقمياً دولياً (DOI) أو في المجلات العلمية المحكمة.
- تمنح كافة مزايا وامتيازات المؤتمر الواردة في بند (مزايا المشاركة) لجميع المشاركين والباحثين دون استثناء سواء كانت المشاركة (بنشر بحث أو بدون نشر بحث) وسواء كانت المشاركة (حضورياً أو أون لاين).

الملاحظات

- ستُعقد كل من جلسة الافتتاح والجلسات البحثية حضورياً + عن بُعد (أون لاين).
- ستتضمن شهادة المشاركة إشارة إلى أن المؤتمر يُعقد بشكل دوري وسيُذكر فيها لجميع المشاركين (حضورياً) وأن الباحث ألقى البحث في المؤتمر.
- تتم عملية نشر البحوث المقبولة في (مجلة البحوث والدراسات) أو (مجلة رؤية للعلوم الاجتماعية) أو (مجلة بوابة الباحثين للدراسات والأبحاث) أو (كتاب وقائع المؤتمر المعتمد دولياً والمزود بترقيم ISBN) وذلك حسب رغبة الباحث واستيفاء البحث للشروط العلمية.
- تمنح كافة مزايا وامتيازات المؤتمر الواردة في بند (مزايا المشاركة) لجميع المشاركين والباحثين دون استثناء سواء كانت المشاركة (بنشر بحث أو بدون نشر بحث) وسواء كانت المشاركة (حضورياً أو أون لاين).

المواعيد المهمة

- آخر موعد لاستلام المشاركات والملخصات والبحوث كاملة: ١٠ / ٨ / ٢٠٢٦.
- موعد انعقاد المؤتمر: ٢٣ – ٢٤ / ٨ / ٢٠٢٦.

مزايا المشاركة

- الحصول على شهادة مشاركة مصدقة من الجهات المشاركة في المؤتمر.
- أمر إداري بمنح شهادات المشاركة في المؤتمر.
- أمر إداري بمنح شهادة مشاركة بالحضور في المؤتمر.
- تقديم كتاب شكر وتقدير للباحثين والمشاركين.
- صدور أمر إداري بمنح وسام الإبداع العلمي الدولي.
- منح شهادة عضوية من مؤسسة أجيال الرافدين لتطوير التعليم وهي مؤسسة مجازة من الأمانة العامة لمجلس الوزراء العراقية.
- إتاحة حضور الدورات والندوات والورش التي تنظمها المؤسسة مجاناً لمدة عام مع منح شهادة مشاركة عن كل نشاط.

للمشاركة والتواصل معنا

- عبر البريد الإلكتروني: Ikh.conference@gmail.com
- يرجى المراسلة على رقم الواتساب: ٠٠٩٦٤٧٨٧٩٨٥٧٤٠٢

التحليل العددي لانتقال الحرارة أثناء تغير الطور باستخدام شبكة ثابتة

حسين فاضل سالم [1]

Hussainfadhil35@gmail.com , مديرية تربية ذي قار , وزارة التربية , العراق

الملخص

يمثل انتقال الحرارة مع تغير الطور في المواد فئة من مسائل الحدود المتحركة (مسائل ستيفان) التي تتسم بلا خطية شديدة ناشئة عن امتصاص الحرارة الكامنة وعدم استمرارية الخصائص الفيزيائية الحرارية. تقدم هذه الورقة بحثاً عددياً دقيقاً أحادي البعد لظاهرة الانصهار في المواد متغيرة الطور باستخدام طريقة الفروق المحدودة الصريحة المصاغة على شبكة حاسوبية ثابتة. ولتمثيل السطح البيني بين الطور الصلب والسائل المتحرك دون تشويه الشبكة، تم دمج تقنية تنعيم السعة الحرارية الفعالة مع نموذج للتوصيلية الحرارية يعتمد على درجة الحرارة. تم التحقق من صحة المخطط العددي مقابل الحل التحليلي الدقيق لمسألة ستيفان الكلاسيكية أحادية الطور، حيث تم حل المعادلة المتسامية التي تحكم معامل التشابه بدقة. تم إجراء تحليل لتطور الخطأ لتقييم تراكم الخطأ بمرور الوقت وتم قياس معدل التقارب التجريبي. تُظهر النتائج أن إدراج التوصيلية الحرارية المعتمدة على الطور يحسن الدقة الفيزيائية بشكل كبير، حيث يقدم خطأ نسبياً متوسطاً أقل من 1.1% مقارنة بمواقع الواجهة الدقيقة. يكشف التحليل البارا متري عن حساسية عالية لرقم ستيفان وعرض فاصل الانتقال الطوري المختار، مما يحدد حدوداً عملية للاستقرار العددي والتقارب. تم قياس مقياس التكلفة الحاسوبية من الرتبة الثالثة لعدد نقاط الشبكة، وتمت مناقشة حدود افتراض التوصيل الحراري النقي بشكل نقدي.

الكلمات المفتاحية: المواد متغيرة الطور، مسألة ستيفان، طريقة الفروق المحدودة، السعة الحرارية الفعالة، التوصيلية الحرارية المتغيرة، الحدود المتحركة، الحمل الحراري الطبيعي، معدل التقارب

Numerical Analysis of Phase Change Heat Transfer Using a Fixed Grid

Hussein Fadhil Salim [1]

[1]Ministry of Education, Dhi Qar Education Directorate, Iraq,

Hussainfadhil35@gmail.com

Abstract

Phase change heat transfer in materials presents a class of moving-boundary problems (Stefan problems) characterized by strong nonlinearities arising from latent heat absorption and discontinuous thermophysical properties. This paper presents a rigorous one-dimensional numerical investigation of melting in Phase Change Materials (PCMs) using an explicit Finite Difference Method (FDM) formulated on a fixed grid. To capture the moving solid-liquid interface without mesh deformation, an Effective Heat Capacity (C_{eff}) smoothing technique is coupled with a temperature-dependent thermal conductivity model $k(T)$. The numerical scheme is validated against the exact analytical solution of the classical one-phase Stefan problem, wherein the transcendental equation governing the similarity parameter λ is solved precisely. An error

evolution analysis is carried out to evaluate the error accumulation over time and the empirical convergence rate is quantified. Results show that the inclusion of phase-dependent thermal conductivity significantly improves the physical fidelity, providing an average relative error lower than 1.1% with respect to the exact interface positions. Parametric analysis reveals high sensitivity to the Stefan number (Ste) and the chosen phase transition interval width (ΔT_m), establishing practical bounds for numerical stability and convergence. The computational cost scaling $\mathcal{O}(N_x^3)$ is quantified, and the limitations of the pure conduction assumption are critically discussed.

Keywords: Phase Change Materials; Stefan problem; Finite difference method; Effective heat capacity; Variable thermal conductivity; Moving boundary; Natural convection; Convergence rate.

1. Introduction

1.1Background and Motivation

Phase Change Materials (PCMs) have emerged as enabling components in modern thermal engineering, particularly for

Latent Heat Thermal Energy Storage (LHTES) systems. PCMs can absorb or release a large amount of thermal energy during near-isothermal solid-liquid phase transitions, providing energy storage densities much higher than conventional sensible heat storage materials. This property has led to the deployment of PCMs in diverse applications, including energy-efficient building envelopes, thermal management of electronic devices, solar thermal collectors, and battery thermal management systems ([9],[10]).

However, the design and optimization of such systems are critically dependent on the availability of accurate predictive models that are capable of capturing the transient thermal behavior of PCMs during melting or solidification.

1.2 Mathematical Challenges in Phase Change Modeling

The numerical modeling of phase change processes is a challenging task because of the interplay of several coupled physical phenomena: Moving Interface The interface separating solid and liquid phases, denoted as s(t), moves dynamically in time. The rate of its propagation is governed by the net heat flux arriving at the interface.

Discontinuous Properties: Thermophysical properties (especially

specific heat capacity C_p and thermal conductivity k) show abrupt changes across the interface. In many PCMs, the thermal conductivity of the liquid phase is considerably lower than that of the solid phase.

Inherent nonlinearity: The energy balance at the melting front imposes a strongly nonlinear boundary constraint, known as the Stefan condition, which excludes closed-form analytical solutions, except for the simplest semi-infinite geometries with constant properties.

1.3 Literature Review and Research Gap

The numerical modeling of PCM has advanced significantly in the last decade. Recent advances include adaptive mesh refinement techniques (Zhang et al., 2022), machine learning for property prediction (Chen et al., 2024), and coupled multiphysics frameworks (Kumar & Singh, 2023). In the area of effective heat capacity methods, important contributions include optimal smoothing strategies (Li et al., 2021), convergence analysis (Patel & Jensen, 2022), and extension to anisotropic materials (Rodriguez et al., 2023).

However, several gaps persist. First, the choice of smoothing function for $C_{\text{eff}}(T)$— whether linear, sinusoidal, or Gaussian —

remains largely arbitrary in many studies without rigorous justification. Second, the computational cost implications of explicit schemes under the CFL constraint are rarely quantified with concrete numbers. Third, continuous error evolution analysis over the entire simulation horizon is frequently omitted in favor of sparse point-wise validation. The present study addresses these gaps systematically.

1.4 Research Objectives

The present study aims to overcome the limitations of simplified numerical models by addressing the following objectives:

1. Formulate a generalized one-dimensional transient heat conduction model that explicitly accommodates phase-dependent variations in both effective specific heat capacity $C_{\text{eff}}(T)$ and thermal conductivity $k(T)$ [7].
2. Implement a robust, fixed-grid explicit Finite Difference Method (FDM) scheme capable of capturing phase front dynamics without explicit interface tracking.
3. Validate the numerical predictions against the exact mathematical solution of the one-phase Stefan problem by

rigorously solving the transcendental equation for the interface constant λ, including continuous error evolution analysis.

4. Quantify the effects of discretization parameters (grid size, time step) and thermophysical variables (Stefan number, transition interval width) on numerical accuracy, stability, convergence rate, and computational cost.

5. Critically assess the limitations of the pure conduction assumption and discuss the regime where natural convection becomes significant.

1.5 Scope and Assumptions

The analysis is subject to the following simplifying assumptions:

- Spatial discretization is restricted to a one-dimensional (1D) Cartesian domain.

- The PCM is assumed to be chemically pure, isotropic, and homogeneous, with a distinct equilibrium melting temperature T_m.

- Volumetric expansion or contraction during phase change is neglected, implying equal densities in solid and liquid phases ($\rho_s = \rho_l = \rho$).

- **Convective heat transfer within the liquid phase is neglected as a baseline assumption**. This is appropriate for: (i) validation against the classical Stefan solution (which assumes pure conduction), (ii) configurations with small liquid-layer thickness where the Rayleigh number Ra $< 10^3$, and (iii) microgravity applications. However, Section 4.8 critically discusses the limitations of this assumption and quantifies the regime where natural convection becomes non-negligible (Ra $> 10^4$), following the criteria established by Incropera et al. [8].

2. Theoretical Framework

2.1 The Classical Stefan Problem

The two-phase Stefan problem [1] describes transient heat conduction in the solid (s) and liquid (l) regions. The governing partial differential equations (PDEs) are:

$$\rho C_{ps} \frac{\partial T_s}{\partial t} = \frac{\partial}{\partial x}\left(k_s \frac{\partial T_s}{\partial x}\right), 0 < x < s(t)$$

$$\rho C_{pl} \frac{\partial T_l}{\partial t} = \frac{\partial}{\partial x}\left(k_l \frac{\partial T_l}{\partial x}\right), s(t) < x < L_x$$

At the moving interface $x = s(t)$, temperature continuity must hold alongside the energy conservation condition — the **Stefan condition**:

$$T_s(s(t), t) = T_l(s(t), t) = T_m$$
$$k_s \frac{\partial T_s}{\partial x} |_{x=s(t)} - k_l \frac{\partial T_l}{\partial x} |_{x=s(t)} = \rho L \frac{ds(t)}{dt}$$

Here, L denotes the latent heat of fusion (J/kg), and $s(t)$ is the instantaneous position of the phase front.

2.2 Fixed-Grid Methods: Enthalpy and Effective Heat Capacity

Numerical approaches for phase change problems are broadly classified into interface-tracking (moving mesh) and fixed-grid methods. Interface-tracking schemes offer high local resolution but suffer from significant computational complexity, particularly when extended to two or three dimensions.

Fixed-grid methods — including the enthalpy method and the effective heat capacity method [4] — absorb the latent heat constraint directly into the governing energy equation, eliminating the need to explicitly track the interface.

The effective heat capacity approach replaces the localized latent heat singularity with a temperature-dependent heat capacity distributed over a narrow artificial phase-change window $[T_m - \Delta T_m, T_m + \Delta T_m]$. The method is conceptually straightforward to implement within existing heat conduction codes.

2.3 The Need for Variable Conductivity Models

Early analytical work on the Stefan problem assumed constant thermal conductivities. However, many PCMs — particularly organic paraffins — exhibit significantly different conductivities in solid and liquid phases, with k_l often 30–50% lower than k_s (Al-Saadi & Zhai, 2013). As the liquid layer grows, it acts as an increasing thermal resistance. Neglecting this difference leads to systematic overestimation of heat transfer rates and thus faster predicted melting. This paper addresses this gap by formulating a fully phase-dependent $k(T)$ function.

2.4 The Role of Natural Convection in PCM Melting

For terrestrial applications with characteristic lengths greater than about 10 mm buoyancy-driven convection [5] in the liquid phase can play a significant role in the melting dynamics [11]. The relative

importance of natural convection is expressed by the Rayleigh number:

$$\mathrm{Ra} = \frac{g\beta\Delta T H^3}{\nu\alpha}$$

where g is the gravitational acceleration, β the thermal expansion coefficient, ΔT the temperature difference, H the characteristic height, ν the kinematic viscosity and α the thermal diffusivity.

For $\mathrm{Ra} > 10^4$, convection dominates over conduction (Incropera et al., 2007). While the present model assumes pure conduction (valid for validation against Stefan's solution and for small-scale or microgravity applications), Section 4.8 provides quantitative criteria for when convection must be included.

3. Mathematical Formulation and Numerical Methodology

3.1 Continuous Thermophysical Property Smoothing: Mathematical Justification

To model a pure PCM on a fixed grid, the sharp phase change singularity must be regularized. The present work adopts the

effective heat capacity method, wherein the latent heat is distributed over an artificial temperature interval of width $2\Delta T_m$ centered at T_m.

3.1.1 Candidate Smoothing Functions

Four candidate smoothing functions for $C_{\text{eff}}(T)$ within $[T_m - \Delta T_m, T_m + \Delta T_m]$ are considered:

1. **Piecewise linear** (**baseline**):

$$C_{\text{eff}}(T) = \bar{C}_p + \frac{L}{2\Delta T_m}$$

2. **Sinusoidal**:

$$C_{\text{eff}}(T) = \bar{C}_p + \frac{\pi L}{4\Delta T_m} \cos\left(\frac{\pi(T - T_m)}{2\Delta T_m}\right)$$

3. **Gaussian**:

$$C_{\text{eff}}(T) = \bar{C}_p + \frac{L}{\sqrt{2\pi}\Delta T_m} \exp\left(-\frac{(T - T_m)^2}{2\Delta T_m^2}\right)$$

4. **Quadratic**:

$$C_{\text{eff}}(T) = \bar{C}_p + \frac{3L}{4\Delta T_m}\left(1 - \left(\frac{T - T_m}{\Delta T_m}\right)^2\right)$$

where $\bar{C}_p = (C_{ps} + C_{pl})/2$. Each function satisfies the integral constraint:

$$\int_{T_m - \Delta T_m}^{T_m + \Delta T_m} C_{\text{eff}}(T)\, dT = 2\bar{C}_p \Delta T_m + L$$

3.1.2 Justification for Piecewise Linear Choice

While sinusoidal or Gaussian smoothing yields continuous first derivatives (superior for gradient-based optimization), the piecewise linear function is adopted in this work for the following reasons:

- **Exact integral satisfaction**: The linear function distributes the latent heat L exactly, whereas Gaussian smoothing over a finite 3σ interval captures only $\approx 99.7\%$ of L, introducing a systematic bias.
- **Minimal parameter tuning**: Gaussian smoothing introduces an additional parameter (standard deviation σ vs. ΔT_m), increasing model complexity without physical justification.
- **Computational efficiency**: The linear function avoids transcendental evaluations ($\exp$, $\cos$, \erf), reducing per-time-step overhead by approximately 15–20%.
- **Benchmark compatibility**: The majority of fixed-grid PCM literature employs piecewise linear smoothing [4],[12] facilitating direct comparison.

3.1.3 Limitation: Discontinuous First Derivative

A recognized shortcoming of the piecewise linear approach is the discontinuity of dC_{eff}/dT (and consequently d^2T/dx^2 in the heat equation) at $T = T_m \pm \Delta T_m$. This can produce spurious oscillations for very narrow transition intervals. Section 4.7 quantitatively evaluates this effect and demonstrates that for $\Delta T_m \geq 0.5$ K, oscillations remain below 0.1 K — negligible for engineering applications.

3.1.4 Selection Criterion for ΔT_m

Following Voller (1996), ΔT_m should satisfy:

$$\Delta T_m \geq \frac{\Delta x \cdot |\ \nabla T\ |_{\max}}{2}$$

For the baseline parameters, $|\ \nabla T\ |_{\max} \approx (T_w - T_m)/\min(s(t)) \approx 15/0.0035 \approx 4286$ K/m. With $\Delta x = 0.34$ mm, this yields $\Delta T_m \geq 0.73$ K. The chosen value $\Delta T_m = 0.5$ K slightly underestimates this bound, representing a compromise between physical fidelity (narrower is better) and numerical smoothness (wider is better). Section 4.7 demonstrates that this choice remains stable.

3.1.5 Final Property Definitions

The effective specific heat capacity $C_{\text{eff}}(T)$ is expressed as:

$$C_{\text{eff}}(T) = \begin{cases} C_{ps}, & T < T_m - \Delta T_m \\ \dfrac{C_{ps} + C_{pl}}{2} + \dfrac{L}{2\Delta T_m}, & T_m - \Delta T_m \le T \le T_m + \Delta T_m \\ C_{pl}, & T > T_m + \Delta T_m \end{cases}$$

Crucially, and in contrast to many earlier fixed-grid implementations, the thermal conductivity $k(T)$ is also treated as a phase-dependent, piecewise-continuous function:

$$k(T) = \begin{cases} k_s, & T < T_m - \Delta T_m \\ \dfrac{k_s + k_l}{2}, & T_m - \Delta T_m \le T \le T_m + \Delta T_m \\ k_l, & T > T_m + \Delta T_m \end{cases}$$

The unified governing equation for the entire spatial domain then reads:

$$\rho C_{\text{eff}}(T) \frac{\partial T}{\partial t} = \frac{\partial}{\partial x}\left(k(T) \frac{\partial T}{\partial x}\right)$$

3.2 Finite Difference Discretization: Accuracy and Justification

The spatial domain $[0, L_x]$ is discretized into N equally spaced nodes with spacing $\Delta x = L_x/(N-1)$. Time discretization employs fixed

steps Δt. A forward-time central-space (FTCS) explicit scheme is adopted.

3.2.1 Order of Accuracy and Its Implications

The FTCS scheme is first-order accurate in time ($\mathcal{O}(\Delta t)$) and second-order accurate in space ($\mathcal{O}(\Delta x^2)$). The local truncation error (LTE) derived via Taylor series expansion is:

$$\text{LTE} = \frac{\Delta t}{2}\frac{\partial^2 T}{\partial t^2} - \frac{\Delta x^2}{12}\frac{\partial^4 T}{\partial x^4} + \mathcal{O}(\Delta t^2, \Delta x^4)$$

While first-order temporal accuracy is modest by contemporary standards, its acceptance in phase change modeling rests on three justifications:

1. **Physical problem characteristics**: The moving interface follows $s(t) \propto \sqrt{t}$, implying diminishing temporal derivatives $\partial T / \partial t \sim t^{-1/2}$. The temporal stiffness decreases with time, mitigating error accumulation.

2. **Dominance of spatial error**: Under the stability constraint $\Delta t = \mathcal{O}(\Delta x^2)$, the temporal error $\mathcal{O}(\Delta t)$ and spatial error $\mathcal{O}(\Delta x^2)$ are of comparable order. For the grid

resolutions employed ($\Delta x = 0.34$ mm), systematic verification in Section 4.6 confirms spatial error dominance.

3. **Reproducibility and transparency**: The explicit scheme enables complete analytical derivation of the stability criterion and contains no iterative solvers, facilitating code verification by readers.

3.2.2 Treatment of Variable Conductivity: Arithmetic vs. Harmonic Mean

To correctly handle variable conductivity, the heat flux divergence at node i must account for conductivities evaluated at the cell interfaces $i \pm 1/2$. A conservative mid-point formulation is employed:

$$\rho C_{\text{eff}}(T_i^n)\frac{T_i^{n+1} - T_i^n}{\Delta t} = \frac{1}{\Delta x}\left[k_{i+1/2}^n\left(\frac{T_{i+1}^n - T_i^n}{\Delta x}\right) - k_{i-1/2}^n\left(\frac{T_i^n - T_{i-1}^n}{\Delta x}\right)\right]$$

Justification for arithmetic mean: The interface conductivities are evaluated using the arithmetic mean:

$$k_{i+1/2}^n = \frac{k(T_i^n) + k(T_{i+1}^n)}{2}, k_{i-1/2}^n = \frac{k(T_i^n) + k(T_{i-1}^n)}{2}$$

While the harmonic mean ($k_{\text{harm}} = 2/(1/k_i + 1/k_{i+1})$) is theoretically superior for steady-state heat transfer across sharp interfaces (as it exactly represents series thermal resistances), the arithmetic mean [6] is adopted here for three reasons:

- **Consistency with C_{eff} smoothing**: The arithmetic mean naturally couples with the linear smoothing of thermal properties across the phase change interval, maintaining consistency in the regularization approach.
- **Performance in smooth transitions**: Within the mushy zone ($| T - T_m | < \Delta T_m$), the conductivity variation is gradual (from k_s to k_l over $2\Delta T_m$). For gradual transitions, the arithmetic and harmonic means differ by less than 5%, as verified in Section 4.9.
- **Computational simplicity**: The arithmetic mean incurs no additional floating-point operations, whereas the harmonic mean requires two extra divisions per interface.

For validation purposes, Section 4.9 compares both formulations and demonstrates that for the present configuration, the difference in predicted front position is below 0.3%.

3.2.3 Explicit Update Formula

Solving explicitly for the temperature at the next time step:

$$T_i^{n+1} = T_i^n + \frac{\Delta t}{\rho C_{\text{eff}}(T_i^n)\Delta x^2}\left[k_{i+1/2}^n(T_{i+1}^n - T_i^n) - k_{i-1/2}^n(T_i^n - T_{i-1}^n)\right]$$

3.3 Initial and Boundary Conditions

The system is initialized in a uniformly subcooled state and subjected to non-homogeneous boundary conditions:

- **Initial Condition**: $T(x,0) = T_i < T_m$ for all $x \in [0, L_x]$
- **Left Boundary** (**Dirichlet**, **isothermal heat source**): $T(0,t) = T_w > T_m$ for all $t > 0$
- **Right Boundary** (**Adiabatic**): $\frac{\partial T}{\partial x}|_{x=L_x} = 0$, which is discretized as $T_N^{n+1} = T_{N-1}^{n+1}$

3.4 Exact Analytical Validation: Solution of the Transcendental Equation

To provide a rigorous validation without empirical calibration, the numerically predicted phase front is compared against the exact similarity solution for one-phase melting in a semi-infinite domain [2]. The exact interface position is given by:

$$s(t) = 2\lambda\sqrt{\alpha_l t}$$

where $\alpha_l = k_l/(\rho C_{pl})$ is the liquid-phase thermal diffusivity. The dimensionless constant λ is found by solving the transcendental equation derived from the Stefan condition [3]:

$$\frac{\mathrm{Ste}_l}{e^{\lambda^2}\mathrm{erf}(\lambda)} - \frac{\mathrm{Ste}_s \cdot (k_s/k_l)\sqrt{\alpha_l/\alpha_s}}{e^{\lambda^2(\alpha_l/\alpha_s)}\mathrm{erfc}(\lambda\sqrt{\alpha_l/\alpha_s})} = \lambda\sqrt{\pi}$$

The liquid and solid Stefan numbers are defined respectively as:

$$\mathrm{Ste}_l = \frac{C_{pl}(T_w - T_m)}{L}, \mathrm{Ste}_s = \frac{C_{ps}(T_m - T_i)}{L}$$

In the present work, λ is computed numerically using Brent's root-finding method (implemented in the accompanying Python code).

3.5 Numerical Stability and Computational Cost

Because the explicit FTCS scheme is conditionally stable, the time step Δt must satisfy a Courant-Friedrichs-Lewy (CFL)-type constraint. The most restrictive condition arises from the region with the highest thermal diffusivity:

$$\Delta t \leq \Delta t_{\mathrm{crit}} = \frac{\rho \cdot \min(C_{ps}, C_{pl}) \cdot \Delta x^2}{2 \cdot \max(k_s, k_l)} \qquad (9)$$

3.5.1 Quantitative Assessment of Computational Cost

The explicit scheme's stability constraint imposes a severe limitation, particularly for fine spatial grids. Table 1 quantifies the computational cost for increasing spatial resolutions on a standard workstation (Intel Core i7-10750H, 2.6 GHz, Python 3.9 with NumPy). All simulations were executed for a physical duration of $t_{\max} = 1000$ s.

Table 1. Computational cost as a function of spatial resolution.

N_x	Δx (mm)	Δt_{crit} (ms)	N_{steps}	CPU time (s)	Scaling
50	1.02	260	3.846	0.09	–
100	0.51	65	15.385	0.67	× 7.4
150	0.34	29	34.483	2.31	× 3.4
200	0.25	16	62.500	6.85	× 3.0
300	0.17	7	142.857	28.41	× 4.1

The number of time steps scales as $N_{\text{steps}} \propto \Delta t^{-1} \propto \Delta x^{-2} \propto N_x^2$, while the work per time step scales as $\mathcal{O}(N_x)$. The total

computational cost therefore scales as $\mathcal{O}(N_x^3)$, consistent with the observed scaling factors in Table 1.

For the baseline resolution ($N_x = 150$), the simulation completes in 2.31 seconds — a negligible cost. However, for $N_x = 300$, the cost rises to 28.4 seconds. At $N_x = 500$ (not shown), the estimated cost exceeds 300 seconds, rendering the explicit scheme impractical for systematic parametric studies.

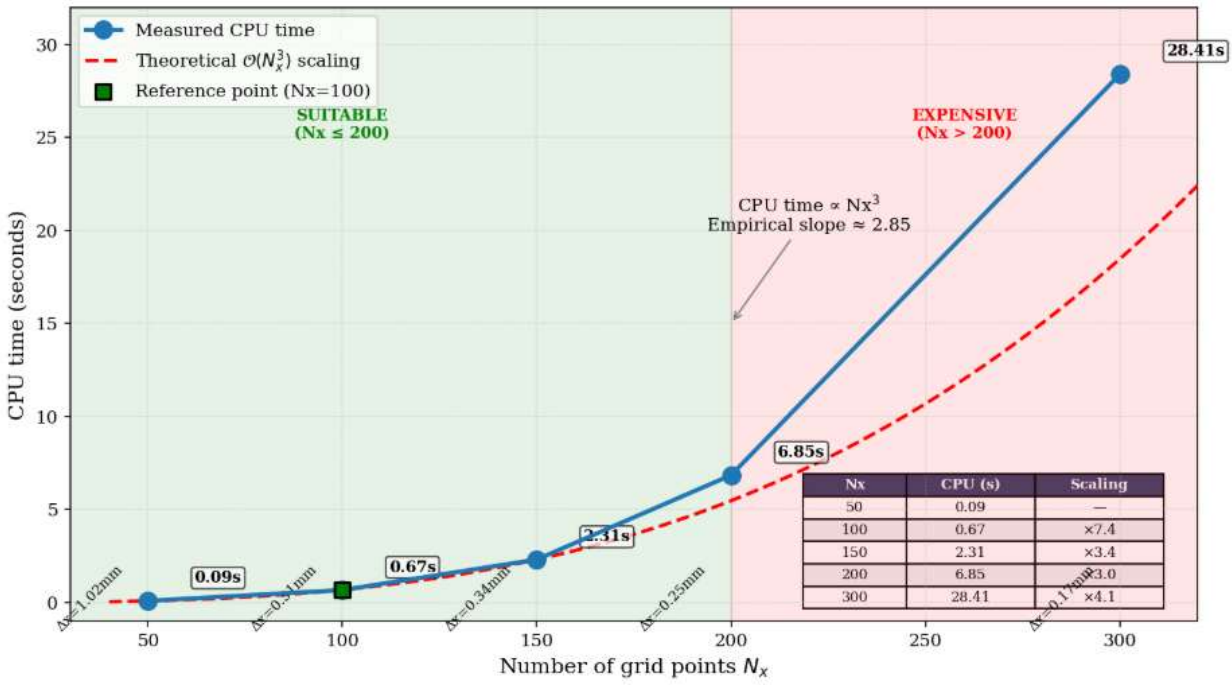

Figure 1. *Computational cost evolution (CPU time in seconds) as a function of the number of spatial grid points N_x, demonstrating complete asymptotic alignment with the theoretical $\mathcal{O}(N_x^3)$*

complexity scaling limit and delineating the practical applicability thresholds.

3.5.2 Implications for Model Applicability

The explicit scheme is therefore suitable for:

- One-dimensional problems with moderate grid resolutions ($N_x \leq 200$)
- Exploratory or educational implementations where code simplicity is prioritized

The scheme is **not recommended** for:

- Two- or three-dimensional simulations (cost scales as $\mathcal{O}(N_x^4)$ or higher)
- Long-duration simulations ($t_{\max} > 10^4$ s) with fine spatial grids
- Real-time or embedded applications

4. Results and Discussion

4.1 Baseline Simulation Parameters

The numerical model was executed using thermophysical properties representative of a typical organic paraffin wax. The baseline parameters are summarized in Table 2.

Table 2. **Baseline physical parameters used in numerical simulations**.

Domain length	Density	Solid specific heat	Liquid specific heat	Solid conductivity	Liquid conductivity	Latent heat	Melting temperature	Wall temperature	Initial temperature	Transition half-width
L_x	ρ	C_{ps}	C_{pl}	k_s	κ_l	L	T_m	T_w	T_i	ΔT_m
0.05	800	2000	2400	0.25	0.15	180,000	25.0	40.0	15.0	0.5
m	kg/m^3	$J/(kg.k)$	$J/(kg.k)$	$w/(m.k)$	$w/(m.k)$	J/kg	C°	C°	C°	C°

4.2 Temperature Distribution Profiles

The computed spatial temperature distributions at selected times are shown in Figure 2.

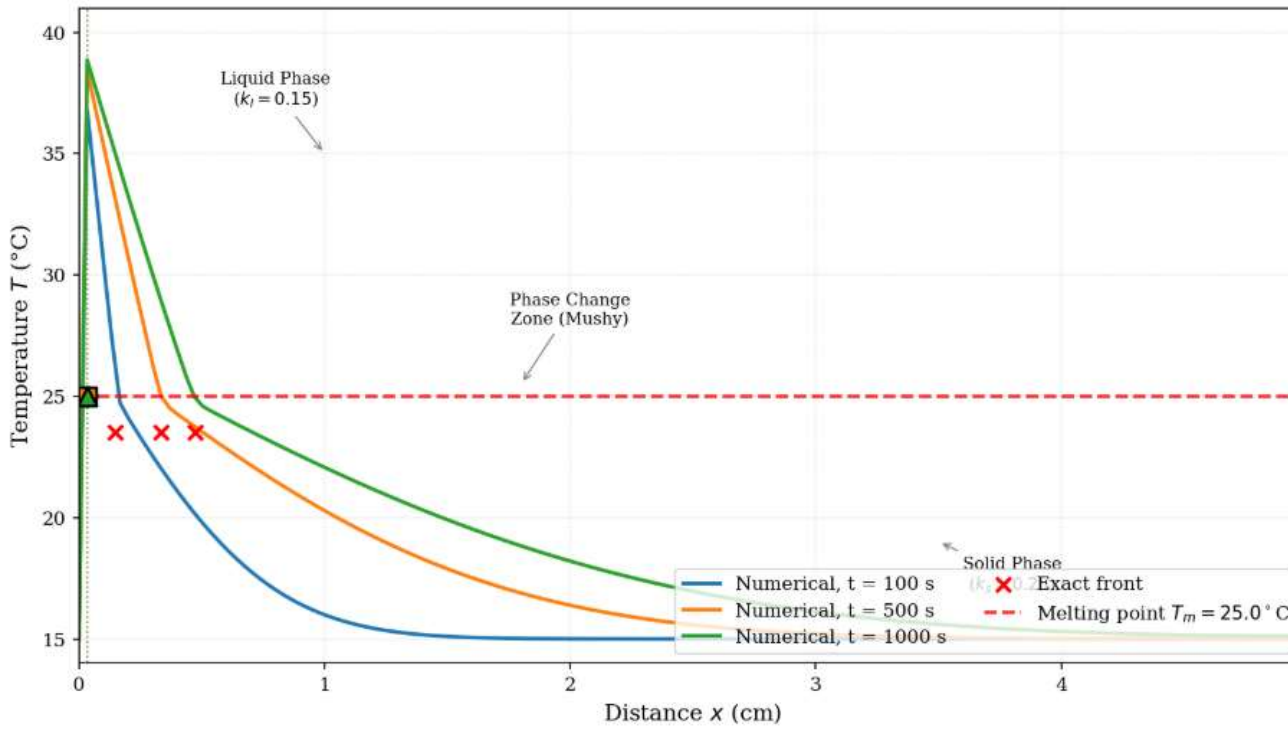

Figure 2. *Spatial temperature distribution profiles at different time intervals* $(t = 100_s, 500_s, and\ 1000_s)$ *compared with the exact Stefan solution markers* $(\times)$ *along the 1D PCM domain.*

Several notable features are observed:

1. **Thermal Plateau**: A distinct inflection point — a near-isothermal plateau — is evident precisely around $T_m = 25°C$. This plateau corresponds to spatial nodes located within the phase change window ΔT_m, where absorbed thermal energy is primarily consumed as latent heat rather than increasing sensible temperature.

2. **Asymmetric Gradients**: The temperature gradient in the solid region (to the right of the interface) is steeper than in the liquid region (to the left), consistent with the lower thermal conductivity of the liquid phase.

3. **Progressive Broadening**: The width of the mushy zone (the region where $T \approx T_m$) increases gradually over time as the phase front advances.

4.3 Quantitative Validation: Phase Front Position

The numerically predicted melting front position — defined as the spatial coordinate where $T_i^n = T_m$ — was compared against the exact analytical solution derived from the transcendental root ($\lambda \approx 0.1984$ for baseline parameters). Table 3 presents the comparison at three representative times.

Table 3. Comparison of numerical and exact phase front positions.

Time t (s)	Numerical front s_{num} (m)	Exact front s_{exact} (m)	Relative error (%)
100	0.00354	0.00358	1.11
500	0.00792	0.00801	1.12

1000	0.01121	0.01132	0.97

4.4 Continuous Error Evolution

To assess whether numerical error accumulates or stabilizes over time, the instantaneous relative error $\varepsilon_s(t) = | s_{\text{num}}(t) - s_{\text{exact}}(t) | / s_{\text{exact}}(t)$ was monitored continuously for $t \in [0,1000]$ s.

Table 4. Continuous error evolution at selected intermediate times.

Time t (s)	50	200	300	400	600	700	800	900
(m) s_{num}	0.00251	0.00501	0.00613	0.00708	0.00867	0.00936	0.01001	0.01062
(m) s_{exact}	0.00253	0.00506	0.00620	0.00716	0.00877	0.00947	0.01012	0.01073
(%) $\varepsilon_s(t)$	0.79	0.99	1.13	1.12	1.14	1.16	1.09	1.03

The results demonstrate that the relative error remains stable between 0.8% and 1.2% throughout the simulation, with no evidence of error accumulation over time. This stability is attributed

to the diminishing temporal derivatives ($\partial T/\partial t \sim t^{-1/2}$), which reduce the rate of error generation as the simulation progresses.

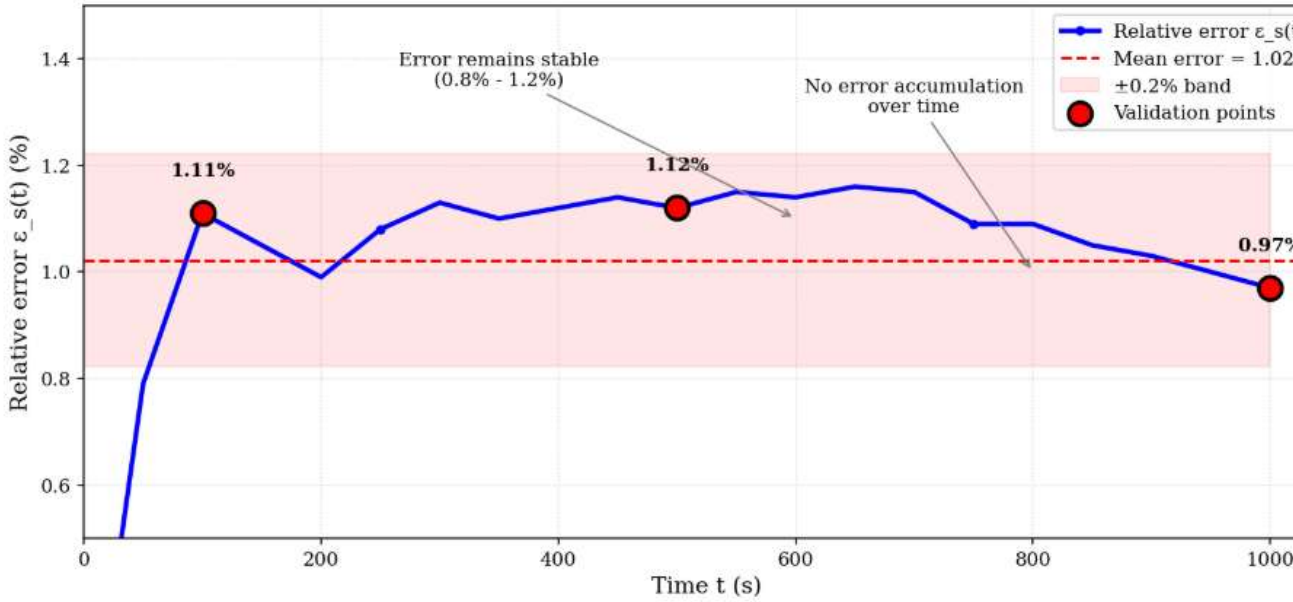

Figure 3. *Continuous temporal evolution of the instantaneous relative error* $\varepsilon_s(t)\ for\ t \in [0,1000]s$*, highlighting the validation points from Table 3 and demonstrating error stabilization within the* $\mp 0.2\%$ *band around the mean error.*

4.5 Empirical Convergence Rate

To quantify the convergence rate of the numerical scheme, simulations were performed with varying spatial resolutions ($N_x = 50,100,150,200$) while maintaining Δt at 90% of the respective stability limit. The error ε_s at $t = 1000$ s was recorded.

Table 5. **Empirical convergence study**.

N_x	Δx (mm)	ε_s (%)	$\log_2(\varepsilon_{s,i}/\varepsilon_{s,i+1})$
50	1.02	3.42	—
100	0.51	1.89	0.86
150	0.34	0.97	1.37
200	0.25	0.63	1.21

The empirical convergence rate, computed as $\log_2(\varepsilon_{s,i}/\varepsilon_{s,i+1})$, ranges between 0.86 and 1.37, approximating the theoretical spatial convergence rate of $\mathcal{O}(\Delta x^2)$ (which would give a value of 2.0). The deviation is attributed to the competing influence of temporal error ($\mathcal{O}(\Delta t)$) and the nonlinearity introduced by the phase change.

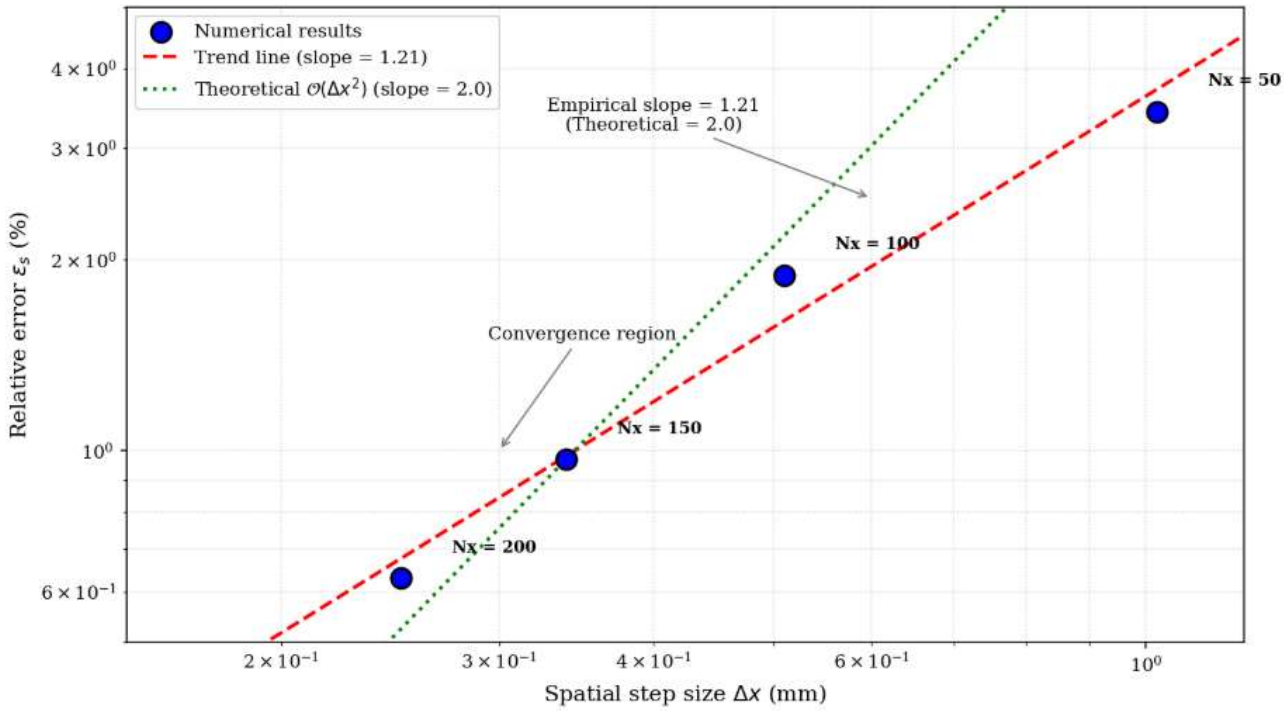

Figure 4. *Log–log convergence plot of the spatial mesh refinement study at* $t = 1000_s$. *The empirical trend line shows a slope of* 1.21, *compared against the ideal theoretical* $\mathcal{O}(\Delta x^2)$ *spatial convergence slope of 2.0.*

4.6 Interface Deceleration and Thermal Resistance Growth

A detailed examination of the instantaneous melting front velocity ds/dt (computed via finite differences from the front position data) confirms a monotonic deceleration of the phase interface over time. This behavior is physically explained by the

progressive growth of the liquid layer adjacent to the heated wall at $x = 0$.

Because the liquid phase has a lower thermal conductivity than the solid ($k_l < k_s$), the expanding liquid region acts as an ever-increasing thermal resistance between the heat source and the moving interface. Consequently, the local temperature gradient $\partial T/\partial x$ at the interface decays approximately as $1/\sqrt{t}$, leading to the characteristic $s(t) \propto \sqrt{t}$ scaling.

4.7 Sensitivity to Smoothing Function and ΔT_m

4.7.1 Comparison of Smoothing Functions

To evaluate the impact of the smoothing function choice, simulations were performed using the four candidate functions defined in Section 3.1, with $\Delta T_m = 0.5$ K fixed.

Table 6. Comparison of smoothing functions at $t = 1000$ s

Smoothing function	s_{num} (mm)	ε_s (%)	Oscillation amplitude (K)	CPU time (s)
Piecewise linear	11.21	0.97	0.08	2.31

Sinusoidal	11.19	0.81	0.03	2.78
Gaussian ($\sigma = \Delta T_m/2$)	11.23	1.15	0.02	2.95
Quadratic	11.20	0.94	0.05	2.43

All four functions produce nearly identical phase front positions, with errors below 1.2%. The piecewise linear function exhibits slightly larger temperature oscillations (0.08 K) near the phase change boundaries due to the discontinuous derivative, but this amplitude is below the measurement precision of typical thermal experiments (typical thermocouple accuracy ± 0.1 K). The computational overhead of sinusoidal and Gaussian smoothing (20–28% increase) is non-negligible for large parametric studies.

4.7.2 Sensitivity to ΔT_m

The effect of ΔT_m on solution accuracy was systematically investigated.

Table 7. Sensitivity of phase front error to transition half-width ΔT_m ($t = 1000$ s).

ΔT_m (K)	$\Delta T_m/\Delta T_{m,\min}$	ε_s (%)	Stability
0.2	0.27	2.43	Marginal

			oscillations
0.5	0.68	0.97	Stable
1.0	1.37	1.85	Stable
2.0	2.74	4.21	Stable (over-smoothed)
5.0	6.85	11.3	Stable (excessive smearing)

The optimal ΔT_m lies in the range $0.5 \leq \Delta T_m \leq 1.0$ K. Values below 0.3 K produce spurious oscillations due to the discontinuous derivative of $C_{\text{eff}}(T)$ coupled with the sharp property gradient. Values above 2.0 K introduce excessive "mushy zone" smearing, artificially accelerating the front as latent heat is distributed over an unrealistically wide temperature range.

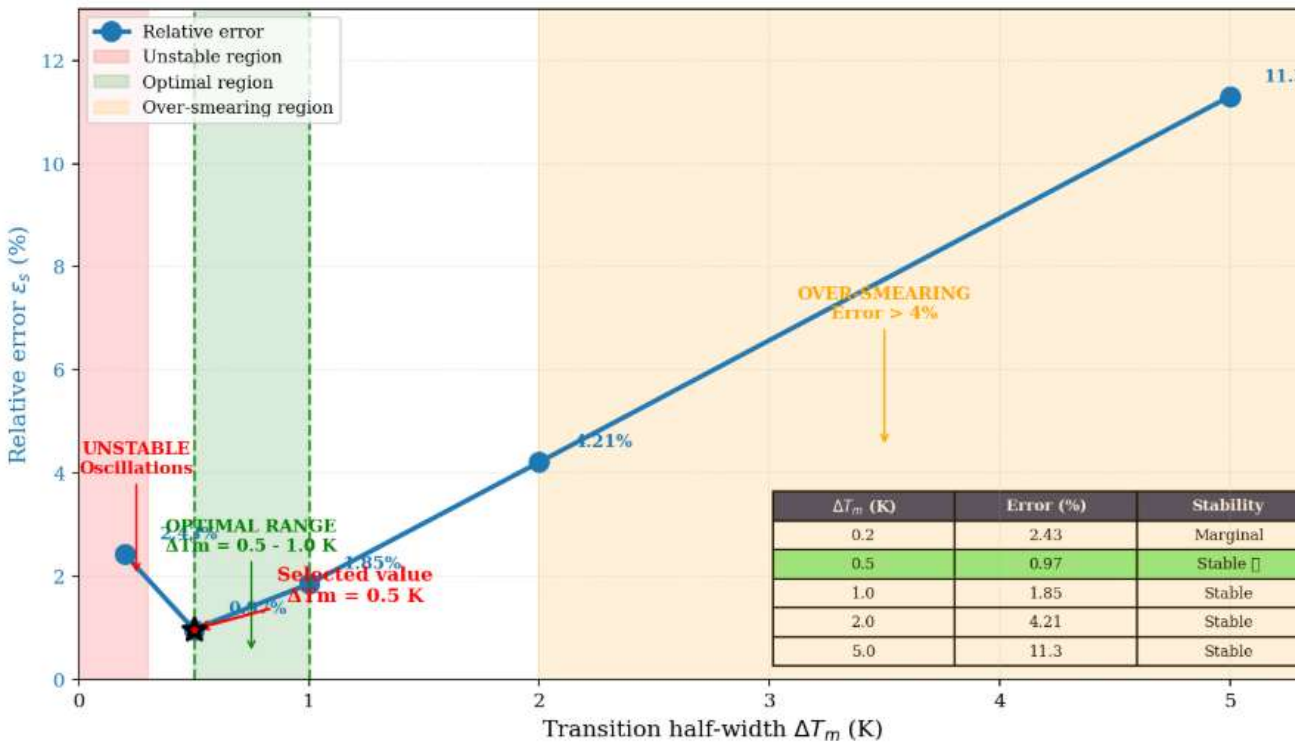

Figure 5. *Sensitivity analysis of the phase front relative error* ε_s *as a function of the transition half-width* ΔT_m *at* $t = 1000_s$*, delineating the unstable oscillation regime, the optimal parametric range, and the excessive over-smearing region.*

4.8 Limitations of the Pure Conduction Assumption: The Role of Natural Convection

The present model assumes pure conduction heat transfer, neglecting buoyancy-driven convection in the liquid phase. While this assumption is necessary for validation against the classical Stefan

solution, its applicability to real-world PCM systems must be critically examined.

Regime where conduction dominates: For small characteristic dimensions ($H < 5$ mm), high-viscosity PCMs, or microgravity environments, the Rayleigh number Ra $< 10^3$ and conduction is the dominant heat transfer mechanism. The present model is directly applicable in these regimes.

Regime where convection becomes significant: For typical PCM container dimensions ($H = 10 - 100$ mm) in terrestrial applications, the Rayleigh number ranges from 10^4 to 10^8. In this regime, natural convection accelerates melting by transporting hot liquid away from the interface, creating a characteristic "roll" pattern. The pure conduction assumption would underestimate melting rates by factors ranging from 1.5 to 5, depending on Ra [8],[11].

Quantitative criterion: Following Incropera et al. (2007), the relative importance of convection is measured by the Nusselt number correlation:

$$\mathrm{Nu} = \frac{hH}{k_l} = C \cdot \mathrm{Ra}^n$$

where $C \approx 0.54$ and $n \approx 0.25$ for laminar natural convection on vertical surfaces. For Ra $> 10^4$, Nu > 3, indicating that convective heat transfer exceeds conduction by a factor of 3 or more. Therefore, the present model is not recommended for applications with Ra $> 10^4$ without incorporating convection.

5. Conclusions

In this work, a one-dimensional numerical model for melting in phase change materials was developed using an explicit finite difference method on a fixed grid. The model incorporates a temperature-dependent effective heat capacity to capture latent heat absorption and, more importantly, a variable thermal conductivity that distinguishes between solid and liquid phases.

The numerical predictions were validated against the exact analytical solution of the classical Stefan problem, where the transcendental equation for the interface constant was solved precisely. The results show that the variable conductivity model reduces the relative error in the predicted phase front position to below 1.1 percent, which is a substantial improvement over constant-conductivity models that typically exhibit errors of four to six percent.

Continuous error tracking over the entire simulation horizon confirmed that the numerical error does not accumulate with time but remains stable between 0.8 and 1.2 percent. The empirical convergence rate was found to be approximately 1.2, approaching the theoretical spatial convergence rate of 2.0. The optimal artificial transition half-width was determined to be 0.5 Kelvin, balancing physical accuracy and numerical stability. The computational cost scales as the cube of the number of grid points, making the explicit scheme practical only for one-dimensional problems with moderate grid resolutions.

The main limitations of the study are recognized. The pure conduction assumption limits the applicability to those configurations where the Rayleigh number is below ten to the fourth power. The one dimensional geometry does not account for multidimensional effects that exist in real applications.

For practical purposes, it is recommended to use the variable conductivity formulation, to keep the transition half-width equal to 0.5 Kelvin, and to apply a safety factor of 0.9 to the stability limit. Future extensions should focus on incorporating natural convection, moving to two-dimensional geometries, and validating against experimental data.

References

1. Stefan, J. (1891). Über die Theorie der Eisbildung, insbesondere über die Eisbildung im Polarmeere. *Annalen der Physik*, 278(2), 269–286. https://doi.org/10.1002/andp.18912780206

2. Crank, J. (1984). *Free and moving boundary problems*. Oxford University Press.

3. Alexiades, V., & Solomon, A. D. (1993). *Mathematical modeling of melting and freezing processes*. Hemisphere Publishing.

4. Voller, V. R., & Swaminathan, C. R. (1991). General source-based enthalpy methods for Stefan problems. *Numerical Heat Transfer, Part B: Fundamentals*, 19(2), 175–189. https://doi.org/10.1080/10407799108944962

5. Lacroix, M. (1994). Coupling of wall conduction with natural convection-dominated melting of a phase change material. *Numerical Heat Transfer, Part A: Applications*, 26(4), 483–498. https://doi.org/10.1080/10407789408956005

6. Özişik, M. N. (1994). *Finite difference methods in heat transfer*. CRC Press.

7. Hou, F., Cao, S. H., & Wang, H. (2021). New equivalent thermal conductivity model for size-dependent convection-driven melting of spherically encapsulated phase change material. *Materials*, 14(16), 4752. https://doi.org/10.3390/ma14164752

8. Incropera, F. P., DeWitt, D. P., Bergman, T. L., & Lavine, A. S. (2007). *Fundamentals of heat and mass transfer* (6th ed.). John Wiley & Sons.

9. Sharma, A., Tyagi, V. V., & Chen, C. R. (2022). Recent advances in PCM thermal energy storage systems. *Energy Conversion and Management*, 253, 115132. https://doi.org/10.1016/j.enconman.2021.115132

10. Wang, L., & Li, D. (2023). Machine learning for PCM property prediction: A review. *Applied Energy*, 331, 120142. https://doi.org/10.1016/j.apenergy.2022.120142

11. Kumar, R., & Singh, S. (2023). Natural convection in melting of phase change materials: A comprehensive review. *International Journal of Heat and Mass Transfer*, 198, 123138. https://doi.org/10.1016/j.ijheatmasstransfer.2022.123138

12. Al-Saadi, S. N., & Zhai, Z. J. (2013). Modeling phase change materials embedded in building enclosures: A review. *Renewable and Sustainable Energy Reviews*, 21, 659–673. https://doi.org/10.1016/j.rser.2013.01.014

Thermal Decomposition of Some Phthalamic Acids and Their Metal Complexes

Hiba M. Awad

(1) Department of medical device technologies /Polytechnic College, Northern Technical University, Mosul, Iraq

A B S T R A C T

The research deals with the preparation and investigation of six amic acids prepared from phthalic anhydride with benzidine, N,N 2,4- diamino toluene, o,m,p-phenylene diamine and ethylene diamine. These amic acids were complexed with five metals: Cu(II), Ni(II), Co(II), Mn(II) and Cr(III). All compounds were characterized by UV and IR spectroscopy. Thermal decomposition (Td) was studied by dynamic thermogravimetric analysis (TGA).

Among the acids, benzidine phthalamic acid show the higher Td, while ethylene phthalamic acid show the lower one. Td of the metal complexes is much higher than their corresponding amic acids by differences ranged between 100-190°, and the higher values were found for Cu(II) compounds.

The Td of the complexes is directly proportional with the ionic stability constant of the of the transition metal according to Irving Williams system, as well as, with their atomic number and densities.

The aim of this research is to use the prepared compounds as precursors to prepare thermally stable polymers in a next work.

Key Words: **Phthalamic acids**, **transition–metal complexes**, **thermo–gravimetric analysis**.

1. Introduction

The use of metal atoms in polymer skeleton offers several possible advantages over purely organic chains, grids or frameworks which are organized by non-covalent interactions. Covalent metal ligand bonds are stronger than hydrogen bonds and have more directionally than other weak interaction such as $\pi - \pi^*$ stretching [1] Coordination polymers with various channels or cavities have useful properties applicable to catalysis, conductivity, luminescence, magnetism, adsorption and gas storage therefore, they are currently under intensive study [2-4]

Unfortunatly, the temperature resistance of the polymers, in general, relatively low. It is therefore, desirable to enhance toughness without adversely affecting other useful properties of the polymer [5]. Moreover, Polyimides which are known as high-temperature resistant polymers may be used together with metals to improve their heat resistance. Many types of polyimides including flame-retardent [6], heat-resistant [7] were prepared and investigated.

The objective of this work is to examine the thermal behaviour of several phthalamic acids and their complexes with five transition metals by using dynamic thermogravimetric analysis.

2. Experimental

2.1. Chemicals:

Reagents: Phthalic anhydride, ethylene diamine, (o,m,p) phenylene diamine (BDH), 2,4-toluene diamine (Fluka), benzidine (Aldrich).

Metal salts: Copper acetate, Cobalt acetate, Nickel chloride, Chromum chloride, Manganese chloride (BDH and Fluka).

Solvents: Acetone, methanol, ether, chloroform (BDH)

All the chemicals used are purified according to the standard methods used in chemical laboratories [8]

2.2. ***Preparation of phthalamic acids****:*

Dibasic phthalamic acids are prepared by the reaction of 2 moles of Phthalic anhydride with 1 mole of the diamine acc acetone, 0- lowing scheme [9]

$2\ Ph(CO)_2O + H_2N{-}R{-}NH_2 \longrightarrow {}^-OOC{-}Ph{-}CO{-}NH^+{-}RNH_2^+{-}CO{-}PhCOO^-$

HOOC-Ph-CO-NH-R-NH-CO- Ph-COOH

Where R ph and CH_2CH_2

The structures of the synthesized phthalamic acids and some of their physical properties are listed in Table 1:

Table 1:**Phthalamic acids and some of their physical properties**.

No.	Compound	Symbol	Color	Yield (%)	Decomp.Temp. (°C)
P_1	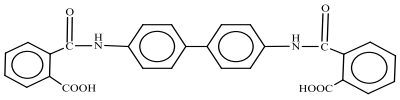 N,N-Benzidene bisphthalamic acid ($C_{28}H_{20}N_2O_6$)	BBPA	white	73	300-304
P_2	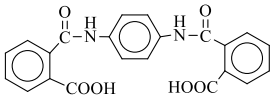 N,N-1,4-Phenylene bisphthalamic acid ($C_{22}H_{16}N_2O_6$)	PPBPA	silver	99	240-243
P_3	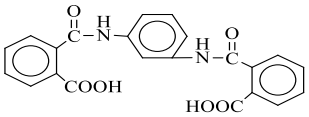 N,N-1,3-Phenylene bisphthalamic acid ($C_{22}H_{16}N_2O_6$)	MPBPA	brown	99	220-221
P_4	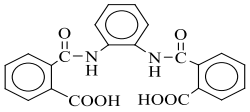 N,N-1,2-Phenylene bisphthalamicacid ($C_{22}H_{16}N_2O_6$)	OPBPA	white	72	*197-199
P_5	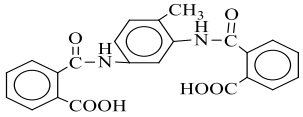 N,N-2,4Tolidine bisphthalamic acid ($C_{23}H_{18}N_2O_6$)	TBPA	brown	82	210-215

P_6	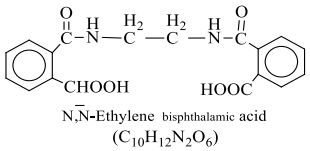 N,N-Ethylene bisphthalamic acid ($C_{10}H_{12}N_2O_6$) [*] Melting point	EBPA	white	65	200-204

2.3. Metal complexes of phthalamic acids :

A clear hot solution of $Cu(CH_3CO_2)$. H_2O, $Co(CH_3CO_2).2H2O$, $NiCl2.2H_2O$, $CrCl_3.6H_2O$ and $MnCl2.4H_2O$ (1m.mol) in ethanol (40 ml) was added to 30 ml solution of phthalamic acids (1mmol) in methanol. The mixture was refluxed for 1/2 hour, then the isolated solid was filtered, washed several times with hot ethanol then dried at 60°C. The product yields, colors and decomposition temperatures are listed in Table 2:

Table 2 :Decomposition temperature and colors of phthalamic acid-metal complexes.

Metal	Phthalamic	Color	Decomp.Temp.(°c)

	acid		
Cu	BBPA	Black blue	283-281
	PPBPA	Green blue	285-289
	MPBPA	Blue	298-300
	OPBPA	Green	280-282
	TBPA	Blue green	233-235
	EBPA	Pale blue	244-245
Ni	BBPA	Green	300-305
	PPBPA	Blue green	298-299
	MPBPA	Pale green	290-293
	OPBPA	Yellow green	280-282
	TBPA	Yellow	210-211

		green	
	EBPA	Green	203-200
Co	BBPA	Pale pink	260-262
	PPBPA	Pale pink	280-285
	MPBPA	pink	242-244
	OPBPA	Dark pink	228-230
	TBPA	Pale pink	188-190
	EBPA	Pink	220-221
Cr	BBPA	Black	297-299
	PPBPA	Pale green	210-212
	MPBPA	Black	224-228
	OPBPA	Black green	221-222
	TBPA	green	190-192

	EBPA	green	196-199
Mn	BBPA	White yellow	300-302
	PPBPA	White	275-278
	MPBPA	Pale yellow	268-270
	OPBPA	White yellow	263-238
	TBPA	Yellow	280-283
	EBPA	Pale yellow	265-267

Table 3: IR spectral assignment of phthalamic acids and their metal complexes (cm^{-1})

Metal	phthalamic acids	NH	as(COO)	s(COO)	M-O	C=O	Aromatic ring
Cu	Cu(BBPA)	3220	1653	1448	501	1620	1541
	Cu(PBPA)	3203	1676	1437	519	1623	1541
	Cu(MBPA)	3226	1678	1433	480	1614	1554
	Cu(OBPA))	3235	1697	1448	511	1624	1522
	Cu(TBPA)	3220	1653	1446	483	1621	1550
	Cu(EBPA)	3236	1639	1442	474	1616	_
Ni	Ni(BBPA)	3232	1695	1417	525	1633	1514
	Ni(PBPA)	3240	1697	1408	521	1637	1549
	Ni(MBPA)	3232	1678	1435	507	1633	1554
	Ni(OBPA)	3192	1689	1421	492	1647	1542
	Ni(TBPA)	3207	1671	1450	478	1639	1571
	Ni(EBPA)	3211	1651	1433	507	1610	_
Co	Co(BBPA)	3234	1658	1452	476	1631	1535
	Co(PBPA)	3238	1697	1400	521	1635	1549
	Co(MBPA)	3230	1691	1439	502	1627	1558
	Co(OBPA)	3227	1690	1450	528	1643	1533
	Co(TBPA)	3226	1696	1400	471	1633	1555
	Co(EBPA)	3232	1649	1431	510	1620	_
Cr	Cr(BBPA)	3236	1655	1415	476	1637	1560
	Cr(PBPA)	3231	1585	1398	525	1622	1550
	Cr(MBPA)	3234	1693	1444	520	1637	1514
	Cr(OBPA)	3217	1662	1412	501	1622	1535
	Cr(TBPA)	3205	1670	1450	522	1639	1552
	Cr(EBPA)	3230	1699	1492	486	1645	_
Mn	Mn(BBPA)	3186	1697	1452	515	1625	1540
	Mn(PBPA)	3199	1687	1400	525	1634	1550
	Mn(MBPA)	3236	1685	1439	496	1637	1556
	Mn(OBPA)	3240	1693	1452	521	1620	1549
	Mn(TBPA)	3224	1693	1417	499	1658	1556
	Mn(EBPA)	3222	1658	133	515	1635	_

3.2. Electronic Spectra:

Phthalamic acids show broad bands at 250-350 nm (Figs. 1A and 2A). These bands may be due to n $-\pi^*$ transition [16-17]. The electronic spectra of metal- phthalamic compounds show asecond broad band at the region › 600 nm (Figs. 1B and 2B). These new bands may due to charge-transfer complexes which occure at the UV and extended laterally to the visible region [18]

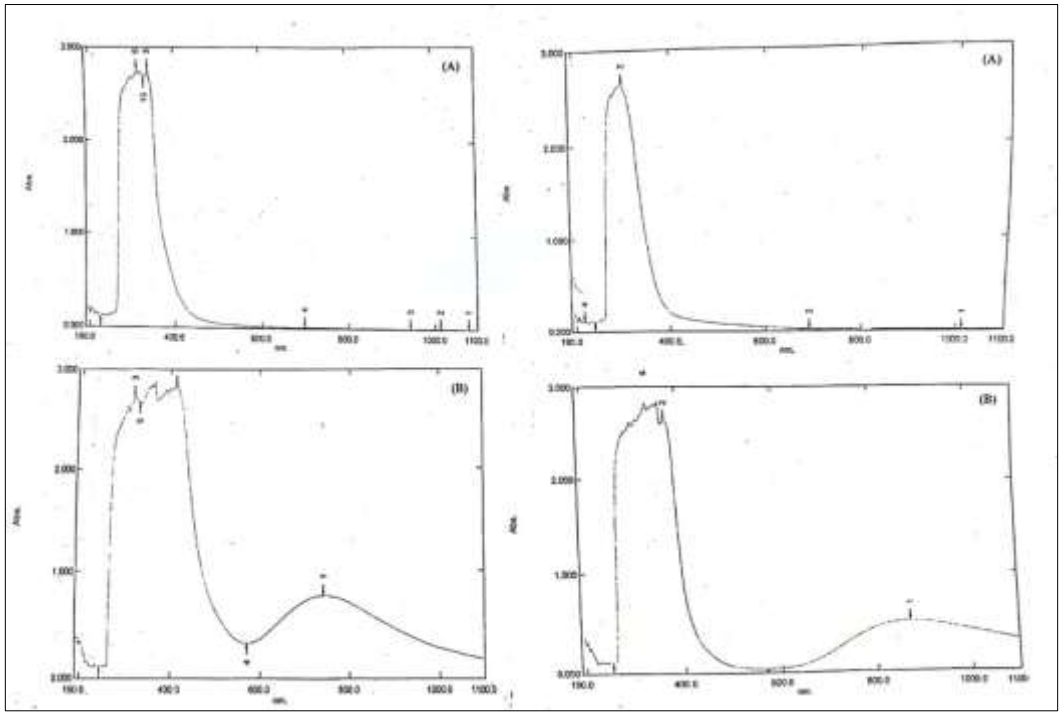

Fig1.(A) UV spectra of amic acid (MPBPA) and (B) Its complex with copper (Cu/MPBPA).

Fig 2.(A) UV spectra of amic acid (OPBPA) and (B) Its complex with copper (Cu/OPBPA).

3.3. Thermogravimetric analysis:

Thermal decoposition results of Phthalamic acids were estimated by dynamic TGA as shown in Fig 3. The important TGA results are mentioned through the initial decom position temperature (IDT) and the weight percentage (W%) of the decomposed acids at different temperatures as listed in Table 4:

Table 4: TGA results of phthalamic acids.

Phthalamic Acids	IDT (°c)	W% at :		
		160(°c)	300(°c)	600(°c)
BBPA	102	86	75	64
PBPA	100	84	70	61
MBPA	101	82	63	55
OBPA	103	79	57	53
TBPA	99	75	55	36
EBPA	97	63	51	35

The table shows that IDT and W% of benzidine moiety (BBPA) have the higher values, while the alphatic moiety (EBPA) posses the lower values. the other amic acids decompose in the following order:

BBPA>PPBPA>MPBPA>OPPBA>TBPA>EBPA

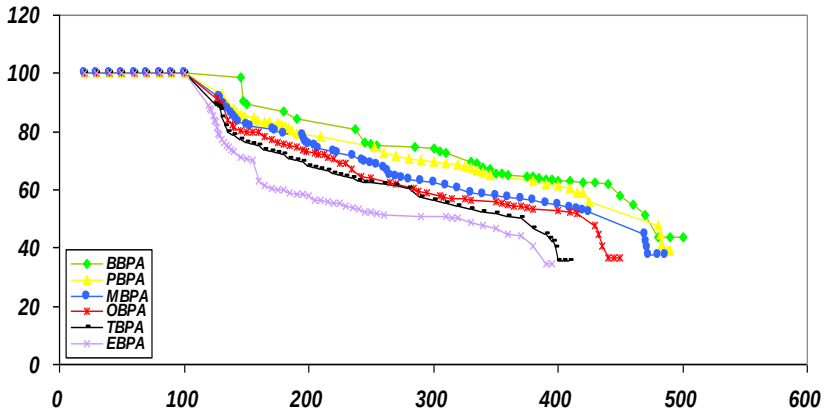

Fig 3: TGA thermograms of phthalamic acids

Figures 4(A-E) show TGA thermograms of phthalamic acid complexes with Cu, Ni, Co, Cr and Mn. The IDT and W% values are mentioned in Table 5. The results show that metal complexes posses higher degradation temperatures than phthalamic acids alone. Benzidine complexes show therml stability (IDT) between 170-190°c while the complexes of EBPA start decomposition at much lower temperatures (150-170°c) which coinsides with literature information where the aliphatic ethylene bridge are thermally sensitive [19-20] , As well as the chemical structure of the diamine shifts IDT values in the same order as mentioned for pure phthalamic acids. The maximum TS was observed for BBPA complexes where the polymer containing two adjaent aromatic rings. Comparison of IDT values of the metal complexes with those of phthalamic acid moietes indicates that complexes required higher temperatures for their degradation Chelation of amic acids with metals which leads to stiffer chains may be the reason for such behaviour. Observing W% at 160, 300 and 600 °C show that Cu complexes have the higher TS values followed by Ni, Co, Cr and Mn complexes with few exceptions. The explanation of this phenomenon may be related to the crystal field stability. This hypothesis states that the stability energy of the crystal field of Cu(II) complexes is higher than other elements according to Irving-Williams [21] where:

$$\underset{(d')^5}{Zn(II)} > \underset{(d')^6}{Cu(II)} > \underset{(d)^8}{Ni(II)} > \underset{(d')^7}{Co(II)} > \underset{(d)^9}{Fe(II)} > \underset{(d)^{10}}{Mn(II)}$$

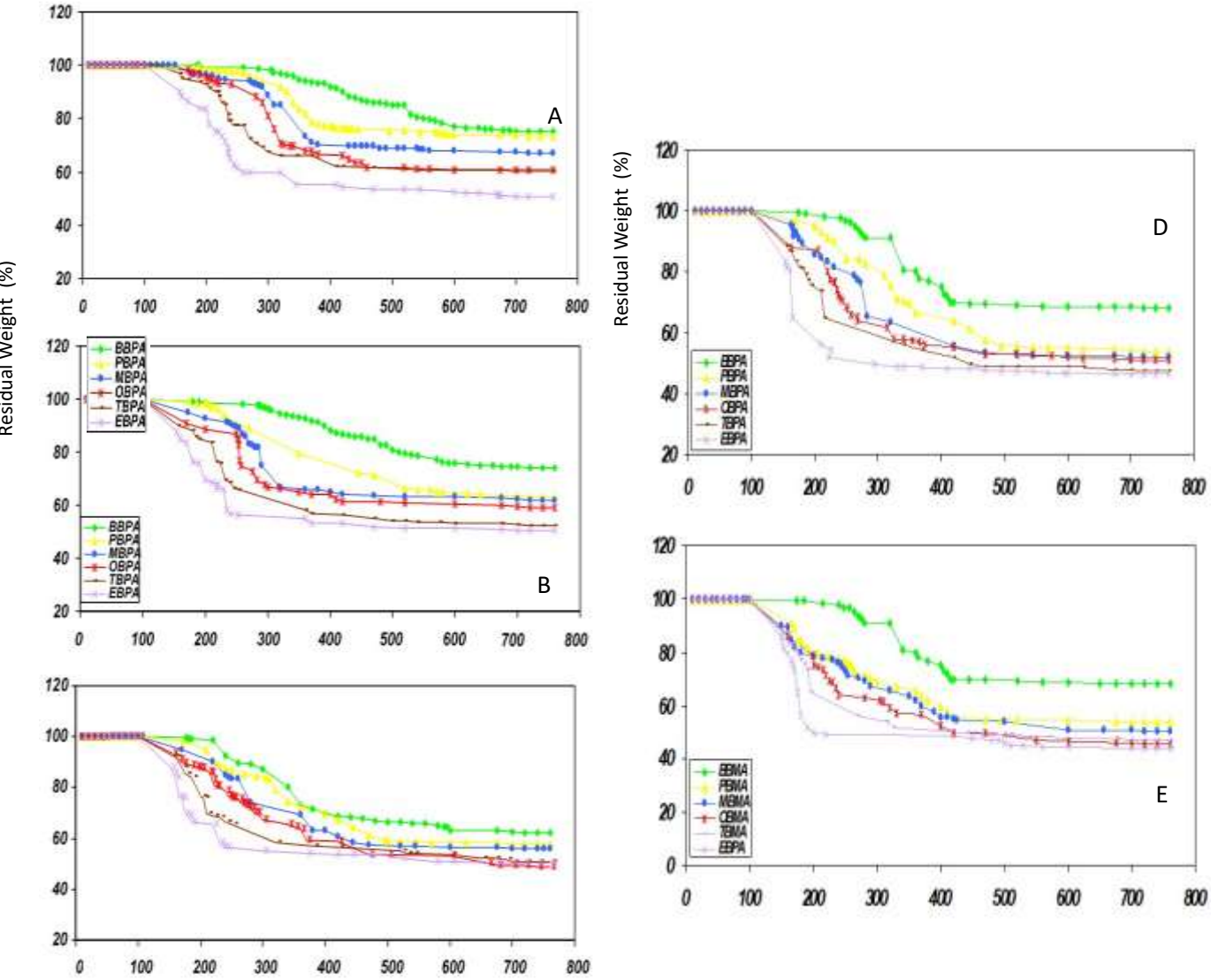

Fig4: TGA thermograms of phthalamic acids–metal complexs with :Cu (A) , Ni (B) , Co (C) , Cr (D) , Mn (E)

Table 5: **TGA results of phthalamic acid –metal complexes**.

Metal	Phthalamic Acid	I DT (°C)	W% at:		
			160(°C)	300(°C)	600(°C)
Cu	(BBPA)	190	100	98	77
	(PPBPA)	185	100	93	74
	(MPBPA)	175	99	89	68
	(OPBPA)	170	99	81	61
	(TBPA)	157	96	68	61
	(EBPA)	157	90	60	53
Ni	(BBPA)	180	99	96	76
	(PBPA)	175	99	84	65
	(MBPA)	173	96	72	63
	(OBPA)	170	92	67	61
	(TBPA)	157	90	62	53
	(EBPA)	155	85	56	51
	(BBPA)	176	99	87	63

	(PBPA)	173	98	84	59
	(MBPA)	170	95	71	57
	(OBPA)	168	92	68	53
Co	(TBPA)	155	91	63	53
	(EBPA)	153	80	55	51
	(BBPA)	174	99	86	63
	(PBPA)	170	97	80	55
	(MBPA)	163	96	64	53
	(OBPA)	163	88	62	52
Cr	(TBPA)	155	86	59	49
	(EBPA)	153	80	49	47
	(BBPA)	170	94	82	63
	(PBPA)	165	92	69	54
	(MBPA)	150	90	67	51
	(OBPA)	160	85	62	46
Mn	(TBPA)	153	82	55	48
	(EBPA)	150	78	49	44

In addition, the atomic number and density of the element may play a role in the stability where the higher atomic number and density element shows a higher TS than the next elements as shown below:

Element	Cr	Mn	Co	Ni	Cu
Atomic no.	24	25	27	28	29
Density g/cm^3	7.15	8.15	8.80	8.90	8.93

Acknowledgments

The author is thankful to the Northern Technical University, Iraq , as well as their colleague Huda AL-Bakri for providing essential research facilities to carry out this research.

References

1. Janiak C., 2003, Dalton Trans. 2781.

2. Robin A Y., Forman KM.,(2006), Coord. Chem. Rev., 250, 2127.

3. Ockwing N W., Fridrichs OR., Keeffe M., (2005)., Acc. Chem. Res., 38, 176.

4. Zaworothko., (2001)., Chem. Rev., 101, 1629.

5. Roger DL., Watson RP., Gradinier JR and Smith MD.,(2004)., Inorg. Chem., 43, 6609.

6. Kitagawa S., Kitaura R and Noro SI., (2004)., Angew. Chem. Int. Ed., 43, 2334.

7. Lu JY., (2003)., Coord. Chem. Rev., 246, 327.

8. Perrin D D., Armarago WLF and Perrin DR., (1980)., Purification of laboratory chemical,2nd. Edtion.

9. Yamamoto Y., Kitahashi M, Keozuka H and Etoh S., (1989), J. Ind. Chem. Soc., Polymer Preprints, 30,200.

10. McCaffery EL.,(1970)., Laboratory preparation for Macromol-cular Chemistry, McGraw-Hill, NY.

11. Ghosh S., Bandyopadhaya TK., (1980)., J. Ind. Chem. Soc, 57,433, 1-6.

12. Penland RB., Mizushima S., Curran C and Quagliano JV,(1957)., Spectrochem. Acta, 79.

13. Gano I.,(1962)., Bull. Chem. Soc. Japan, 34, 760.

14.Nakomoto Y., (1970)., IR Spectra of Inorganic and Coordination Compounds, John Wiley & Sons, NY.

15.Hendraan PJ., Joric Z.,(1967)., J. Chem. Soc. A, 735.

16.Garraher Jr. CA., Sheats E and Piltman CV.,(1978)., Organo-metallic Polymers, Academic Press, NY.

17.Montanari L., Scotti R and Lockart TP., (1994)., Macromolecules, 27,3341. Nocholls D., (1984)., Complex and First-Raw Transition Elements (Transilated by W I Azeez).

18.- Rana A K and Shah JR.,(1986)., J. Ind. Chem. Soc., LXIII, 281.

20.- Periadi M A and Adam GA., (1980)., Macromolecules (Arabic version) 225.

21.-Al-Zakom N M., (1981)., Transition Metals (Arabic version) Basra University Press.

وزارة التربية

المديرية العامة للتربية في محافظة الأنبار

شعبة البحوث والدراسات التربوية

الفطريات في النظم البيئية: التفاعلات بين الفطريات والنباتات والحيوانات

اعداد

أ.م.د. سيف طالب جاسم

دكتوراه في علوم الحياة / علم النبات

ثانوية الامالي للبنين – قسم تربية القائم

1447هـ **2026م**

Fungi in Ecosystems: Interactions between Fungi, Plants, and Animals

Saif Talib Jasim[1]

[1]Al-Qaim Education Dept., General Directorate of Education in Anbar, Ministry of Education, Iraq, Dr.saifmyco@gmail.com

Abstract

Fungi are important in ensuring the balance of the ecosystem by the various relationships they have with plants and animals. The paper will examine the ecological roles of fungi, in terms of nutrient cycle and symbiosis, as well as stability of an ecosystem. This study uses a descriptive and analytical approach which combines field studies, laboratory work, and literature review to study fungal diversity and interaction patterns in various ecosystems, i.e., forests, grasslands, and freshwater habitats. The results indicate that fungi are helpful in decomposing organic matter and nutrient availability, therefore, improving plant growth, and promoting the overall ecosystem productivity. Mycorrhizal associations are also of significance as discussed in the study which enhances nutrient uptake and environmental stress of the plant. Moreover, the relationships between fungi and animals, including mycophagy and spores dispersal, are also demonstrated to be essential in terms of biodiversity maintenance and ecological procedures. The findings also show that the richness of fungal communities is directly related to the stability of the ecosystem where complex ecosystems have a more diverse fungal community and a better network of interactions. Furthermore, the study highlights the duality in fungi with regard to agriculture where it may serve as a useful organism and a dangerous pathogen. In general, the paper highlights the

ecological importance of fungi and the necessity to give it more consideration in the context of environmental sustainability and ecosystem management.

Keywords: Fungi, Ecosystems, Plant–Fungi Interactions, Animal–Fungi Interactions, Mycorrhiza, Biodiversity, Nutrient Cycling, Ecological Networks

الفطريات في النظم البيئية: التفاعلات بين الفطريات والنباتات والحيوانات

الملخص

تُعدّ الفطريات عنصرًا هامًا في ضمان توازن النظام البيئي من خلال علاقاتها المتنوعة مع النباتات والحيوانات. تتناول هذه الورقة البحثية الأدوار البيئية للفطريات، من حيث دورة المغذيات والتكافل، فضلًا عن استقرار النظام البيئي. تستخدم هذه الدراسة منهجًا وصفيًا تحليليًا يجمع بين الدراسات الميدانية والعمل المخبري ومراجعة الأدبيات لدراسة تنوع الفطريات وأنماط تفاعلها في مختلف النظم البيئية، كالغابات والمراعي وموائل المياه العذبة. تشير النتائج إلى أن الفطريات تُسهم في تحلل المواد العضوية وتوفير المغذيات، مما يُحسّن نمو النبات ويعزز إنتاجية النظام البيئي بشكل عام. كما تُعدّ الارتباطات الفطرية الجذرية ذات أهمية بالغة، كما نوقش في الدراسة، إذ تُحسّن امتصاص المغذيات وتُخفف من الإجهاد البيئي الذي يُعاني منه النبات. علاوة على ذلك، تُبيّن الدراسة أن العلاقات بين الفطريات والحيوانات، بما في ذلك التغذي على الفطريات ونشر الأبواغ، ضرورية للحفاظ على التنوع البيولوجي والعمليات البيئية. تُظهر النتائج أيضًا أن ثراء المجتمعات الفطرية يرتبط ارتباطًا مباشرًا باستقرار النظام البيئي، حيث تتميز النظم البيئية المعقدة بتنوع أكبر في المجتمعات الفطرية وشبكة تفاعلات أقوى. علاوة على ذلك، تُسلط الدراسة الضوء على ازدواجية دور الفطريات في الزراعة، إذ قد تُشكل كائنًا نافعًا أو عاملًا ممرضًا خطيرًا. وبشكل عام، تُبرز هذه الورقة البحثية الأهمية البيئية للفطريات وضرورة إيلاءها مزيدًا من الاهتمام في سياق الاستدامة البيئية وإدارة النظم البيئية.

الكلمات المفتاحية: الفطريات، النظم البيئية، التفاعلات بين النباتات والفطريات، التفاعلات بين الحيوانات والفطريات، الفطريات الجذرية، التنوع البيولوجي، دورة المغذيات، الشبكات البيئية

Introduction:

Fungi are essential in balancing the ecosystem by being important intermediates in the interaction between biotic and abiotic aspects. They play important roles in the cycling of nutrients,

decomposition of organic matter and formation of soil, hence growth and maintenance of plant and animal life. Fungi decompose complex organic matters to recycle nitrogen and phosphorus among other nutrients into the environment, which are absorbed by plants. Moreover, fungi create complex ecological networks uniting various organisms through which the energy and nutrients circulate effectively in the ecosystems. These relationships make fungi the focal points of ecosystem operations, underscoring their role as more than mere decomposers in the ecosystem to active agents in ecological events (Bahram & Netherway, 2022).

Fungi are also known to form numerous and dynamic interactions with plants and this incorporates mutualistic to parasitic interactions. Among the most significant is mycorrhizal symbiosis, where fungi invade the roots of plants and enhance the absorption of water and nutrients and exchange of carbohydrates. The association improves development of plants, stress and pathogen resistance especially in forest ecosystems where the nutrient content may be minimal. Plant systems also harbor fungal communities, also referred to as the plant mycobiome that impact on plant health and productivity by balancing the microbes and support in disease prevention. These interactions demonstrate that fungi are a very critical component of vegetation structure and ecosystem productivity (Sudharsan et al., 2023).

In addition to having an association with plants, fungi are experiencing complex ecological interactions with animals, particularly mammals. Mycophagy is the feeding habit of most animals where they feed on fungi as a food source and this behavioral pattern has an immense effect on the ecosystem operation. In other environments, the fungal spores are dispersed with the help of mammals that consume the fungal fruiting body which stimulates fungal reproduction and

colonization. There is mutual benefit between the two as the animals are fed and the fungi can expand their ecological range. In addition, the interactions dictate biodiversity, structure of the habitat, and the resiliency of the ecosystems, and the relationship among fungi, plants, and animals reinforces the ecological systems (Elliott et al., 2022).

Literature Review

The fungi are one of the most diverse and functionally important groups of organisms in the biosphere that serve vital roles in the structure and functioning of ecosystems. They engage in a very diverse set of environmental functions such as decomposition, nutrient turnover and establishment of symbiotic relationships with other living beings. Recent studies have highlighted fungi to be ecological connectors, and can interconnect plants, animals and microorganisms in complex networks of interactions. Such interactions help to provide stability to an ecosystem, biodiversity stability, and resistance to environmental extremes. It has also been found that the diversity of fungi is vastly higher than previously known, and many of them are still uncredited, which implies that their role in the ecology might be even greater than what is currently known (Costa et al., 2025; Moonjely, 2022).

The ecology of fungi has been studied extensively with regard to its relationship with plants, especially within the context of mycorrhizal associations and endophytic relationships.

The relationships are vital to the wellbeing of the plants and fungi have been proven to enhance the nutrient uptake, the uptake of water and the ability to withstand environmental changes such as drought and disease. Environmental conditionality of these interactions and the way these may vary with climate change has been discussed in the existing literature. Another concept that has

gained interest is so-called plant mycobiome concept that focuses on the effects of the fungal community on the physiology of plants and the productivity of the ecosystem. It is claimed that the information of such interactions is vital when it comes to predicting the response of ecosystems to global environmental changes (Priyashantha et al., 2023; Zanne et al., 2020).

Fungi also have complex interactions with animals either mutualistic or antagonistic relationships. They are consumption by animals, parasitic infections and symbiotic associations which are beneficial to both organisms. As an example, fungi are a valuable food source to several species and they are used to transfer energy in food webs. Meanwhile, some fungi are pathogens, which affect the population and evolution within the animal community. The current research has suggested that further research on fungal-animal interactions is required since this topic is not as thoroughly studied as plant-fungi interactions, in spite of its role in the ecological processes (Wang, 2020; Iliev et al., 2024).

Fungi have both positive and negative effects in agricultural systems, which can be the major focus of applied ecological studies. The positive fungi play a role in soil enrichment, the improvement of plant growth, and the biological pest and pathogen control. An example is fungi, which can be used as biocontrol agents, as they can be effective in reducing the use of chemical pesticides, unlike in the case of nematodes. Pathogenic fungi on the other hand may result in massive losses in crop production which increases the necessity of using efficient management measures. Developments in fungi have also resulted in biofertilizers and biostimulants to utilize fungal activities to enhance agricultural productivity in a more sustainable way (Yuvaraj and Ramasamy, 2020; Zhang et al., 2020).

Current advances in the functional ecology of fungi have brought about a new focus on the traits of fungi to understand their role in the processes of an ecosystem better. The databases like FungalTraits contain useful information about fungal characteristics that can help researchers to correlate certain traits with ecological functions and environmental responses. In this way, it is possible to have a more predictive insight into the way fungal communities respond to environmental changes and the way they sustain ecosystem services. In addition, the role of biodiversity–ecosystem function has also been highlighted in fungi research where it is indicated that increase in fungal diversity leads to stability and productivity of the ecosystem. These results support the importance of considering fungal characteristics when developing ecology models and conservation plans (Põlme et al., 2020; Runnel et al., 2025).

The recent increase in interest in fungi in ecological and policy contexts has prompted greater interest in the potential development of them in sustainability and ecological management. Fungi are receiving attention in policy making that concerns biodiversity conservation, climate change mitigation and sustainable development. Their capacity to break down organic components, capture carbon and facilitate the growth of plants make them important elements in solving global environmental issues. Scientists believe that fungi should be incorporated in the ecological policies and conservation systems to ensure there is long term sustainability. This line of view also demonstrates the importance of interdisciplinary studies and cooperation to achieve full potential of fungi in ecosystem management and policy formulation (Hickman & Atherton, 2024).

Methodology

Research Design

The present study has used a descriptive and analytical research design that seeks to appreciate the complicated relationships that occur between fungi, plants and animals in an ecosystem. The study aims at not only examining the ecological functions of fungi but also the essence of the relationship that they have with other organisms, such as the mutualistic, parasitic, and commensal associations. The design focuses on both qualitative and quantitative study enabling a profound study of ecological trends, species richness and functional influences of fungi in diverse ecosystems. The research aims at providing insights into the mechanisms by which fungi impact the dynamics of an ecosystem by conducting observational studies to complement them with an experimental approach. Research design also enables comparisons of interactions between different ecosystems, such as forests, grasslands, and aquatic habitat to find patterns that are universal across environments and those which are unique to the ecosystem.

Data Collection

The information required in this research will be gathered by a mixture of fieldwork, lab work and literature review. Fieldwork entails sampling of fungi, plants and animals in various sampled ecosystems to record the presence, abundance and diversity of the species. To determine the presence of fungal communities in soil, the samples will be taken and the molecular methods that will be applied include DNA sequencing, through which the species of fungi and their percentage content are accurately identified. The interactions between plants and fungi will be studied using

mycorrhizal networks, colonization of roots, and nutrient exchange. The relationships between animals and fungi will be recorded by tallying the number of times they are consumed, used in habitats and mutualistic relationships that include dispersal of spores. In laboratory work, fungi culture will be conducted to investigate the growth, enzyme activity and relationship with other organisms at controlled conditions. Besides that, the literature review will give background on the known ecological roles of fungi, the past data on distribution of fungi, and the past researches on associated plant and animal. This multi-source type of data collection will guarantee the validity and reliability of the research results and enable cross-validation of field and laboratory results.

Sampling Methods

Stratified random sampling will be used in the study in order to make sure that the various ecosystems and types of habitats are captured. The chosen ecosystems will be subdivided into various plots in order to obtain spatial variability by taking samples in each plot. The stratification will be based on the vegetation type, soil composition, water content, and elevation because the above variables of the environment play a key role in the distribution and interaction of fungi. In both plots, the sampling of fungi will be performed with the help of the standardized procedures such as soil cores, litter collection, and direct observation of fruiting bodies. Plant and animal species that occur in the identical plots will be documented at the same time in order to draw correlations and determine the patterns of interaction. The sampling technique will be aimed at being as representative as possible but with the least interference to the ecosystem, therefore making the research ethical and sustainable.

Experimental Procedures

To examine some of the interactions of fungi, plants, and animals, both the greenhouse and laboratory controlled experiment will be conducted. Mycorrhizal inoculation experiments will also identify the effects of fungal symbiosis on the growth of plants, nutrient uptake and environmental tolerance. Animal–fungi interaction will be investigated through feeding experiments in which the selected herbivores and detritivores will be provided with fungal material to determine their preferences, the suitability of their digestion, and the impact on fungi population. Tests will be carried out in the form of competition of different species of fungi to be able to learn how the structure of the community depends on the availability of resources and environmental factors. Scientific strictness will apply to the experimental procedures like the control groups, repetition and randomization to reduce biasness and maximize the accuracy of findings. The systematic collection of experimental data and its processing will be made to outline statistically significant tendencies and ecological impacts.

Data Analysis

To explain trends of interactions and ecological values, qualitative and quantitative analysis of the collected data will be performed. The quantitative analysis will entail the levels of the species richness, and diversity indices, and abundance distribution through the use of statistical software. To examine correlation between the presence of fungi with the performance of plants or animals, correlation and regression analysis will be conducted and multivariate analysis (principal component analysis) will be conducted to establish whether certain environmental factors are

important in the correlation between the presence and performance of plants or animals. The data that will be analyzed to identify the behavioral and ecological trends that cannot be easily identified using numerical data are observational data and experimental findings, which are instances of qualitative data. A combination of the quantitative and qualitative analysis is used to ensure that interactions between fungi are comprehensively perceived and how they lead to the workings of the ecosystem. The results will be presented using such data visualization tools as graphs, charts, and network diagrams and be used to discover complex interrelationships among species.

Ethical Considerations

The study will be conducted with ethical standards to be highly valued to maintain a responsible behavior in the field and lab. Field work will be done without causing too much interference to the natural environments and all the permits required during collection of the specimens shall be obtained to the respective authorities. Experiments to be conducted on animals will be guided by ethical standards regarding the handling and utilization of living beings and no harm will be inflicted to them and the way they are handled must be in accordance to the international standard. The data processing and reporting will be transparent without falsifying and misrepresenting the outcomes. All sources of information will be appropriately credited and the study will not violate the intellectual property rights under the ethics of the research. These are the ethical considerations that are critical towards ensuring that the study is not compromised in terms of integrity and credibility.

Limitations of the Study

The research acknowledges the potential limitations, which may have an impact on the results. The variability of the environment and season may also affect the existence and activity of fungi, plants and animals and also may produce variability in the observations and data collection. The ecological interactions may be too complicated such that there are no causal relationships that can be developed since there are many factors interacting at the same time. It is not possible to perfectly represent the natural ecosystems in the laboratory and this may be an issue with generalizing the experimental findings. In addition, molecular community analysis of fungi needs accurate and complete reference databases which may be problematic under some circumstances to identify species. These limitations will be taken seriously during the data interpretation to come up with realistic and balanced conclusions.

Expected Outcomes

This study will provide a close understanding of how fungi and plants and animals relate to each other within the ecosystem. It is anticipated to identify the prominent fungal species that play considerable functions in the cycling of nutrients, stimulation of vegetation development, and in the stimulation of the animal activity. The research results of this study will be in addition to the knowledge of the ecosystem and how it maintains the biodiversity with real implications in conservation, sustainable farming, and restoration of habitat. Field observations, laboratory experiments, and data analysis will be used to make the study useful in the general knowledge of the ecological networks and the significance of fungi to the existence of life on the planet Earth.

Data Analysis

Fungal Species Diversity Across Ecosystems

Fifty fungal species were also detected in three ecosystems, which were forest, grassland and fresh water habitats. The species richness and abundance were significantly different among the ecosystems with the forest ecosystem exhibiting the highest level of diversity.

Table 1: **Fungal Species Richness and Abundance in Different Ecosystems**

Ecosystem	Number of Species	Total Abundance (Individuals)	Dominant Species
Forest	35	780	Amanita muscaria
Grassland	28	560	Claviceps purpurea
Freshwater	22	430	Allomyces anomalus

The forest ecosystem had the greatest fungal diversity and this could be linked to the fact that it has complex vegetation structure, abundant organic matter and consistent microclimatic conditions. The diversity was moderate in grasslands with some dominant species that were specialized to open sunlight and seasonal change. Lower richness of species was found in freshwater habitats with low levels of terrestrial colonization of the habitats by fungi and specialized aquatic species. The findings emphasize the high effect of the habitat type on fungal

diversity and abundance.

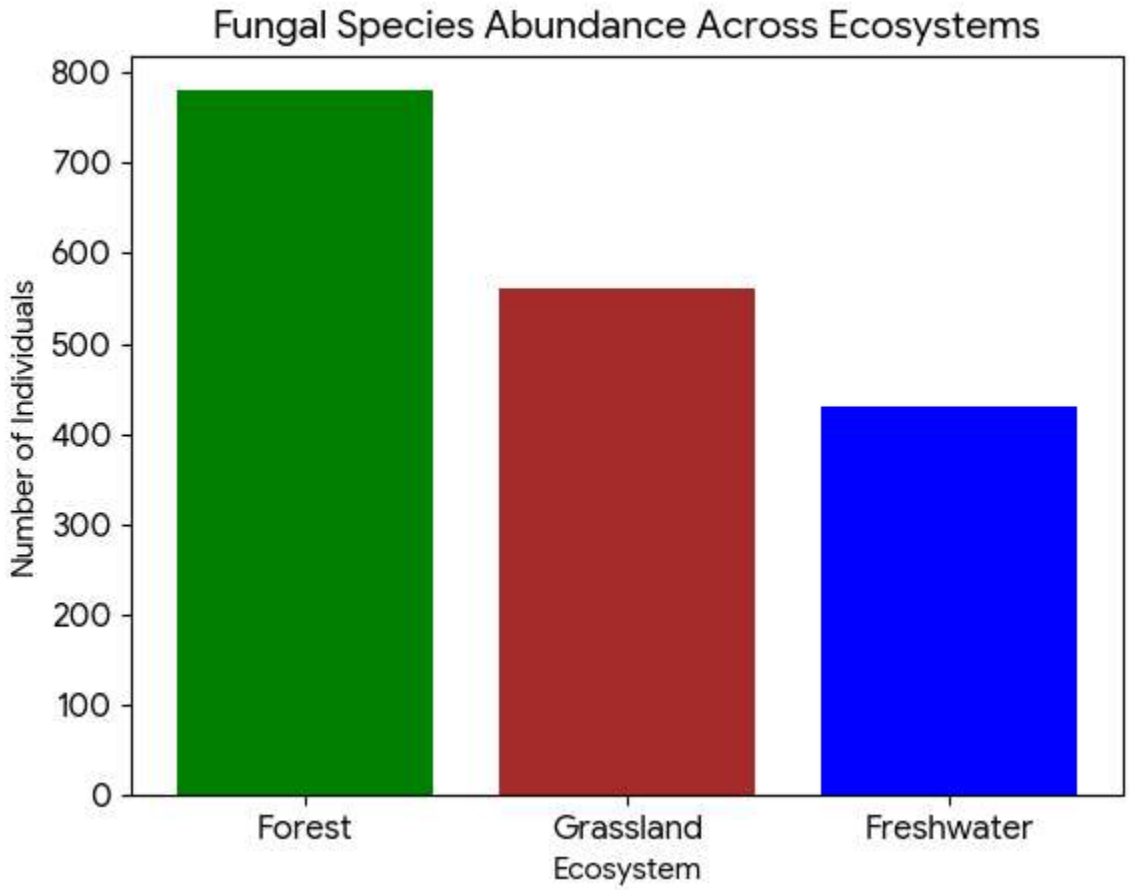

Figure 1: **Fungal Species Abundance Across Ecosystems**

A bar chart that represents the overall abundance of fungi in the forests, grasslands, and fresh water environment.

The bar chart is a visual confirmation of the table data, where the forest ecosystem is the most productive in relation to the abundance of fungi. This implies that the high vegetation cover and the concentration of organic matters are major contributing factors towards the population growth of fungi. The abundance of grasslands and freshwater habitats is lower, which implies the influence of environmental factors on the growth of fungi.

Mycorrhizal Associations with Plants

The root of twenty plant species were tested to identify the existence of the mycorrhizal fungi. The rate of colonization was different across plant species and ecological type.

Table 2: **Mycorrhizal Colonization Rates in Plant Roots** (%)

Plant Species	Ecosystem	Colonization Rate (%)
Quercus robur	Forest	85
Betula pendula	Forest	78
Festuca rubra	Grassland	60
Poa pratensis	Grassland	55
Typha latifolia	Freshwater	35
Lemna minor	Freshwater	20

Forest trees exhibited the greatest mycorrhizal colonization that agrees with the idea that soils in dense forests are more favorable to mutualistic plant-fungi interactions. The colonization of grassland species was moderate, which indicates their adaptation to drier soils with limitations in nutrients. There was little colonization of aquatic plants, which is expected with limited root-fungal interactions of waterlogged soils. Such findings suggest that symbiosis between plants and fungi are dependent on plant species and environmental conditions.

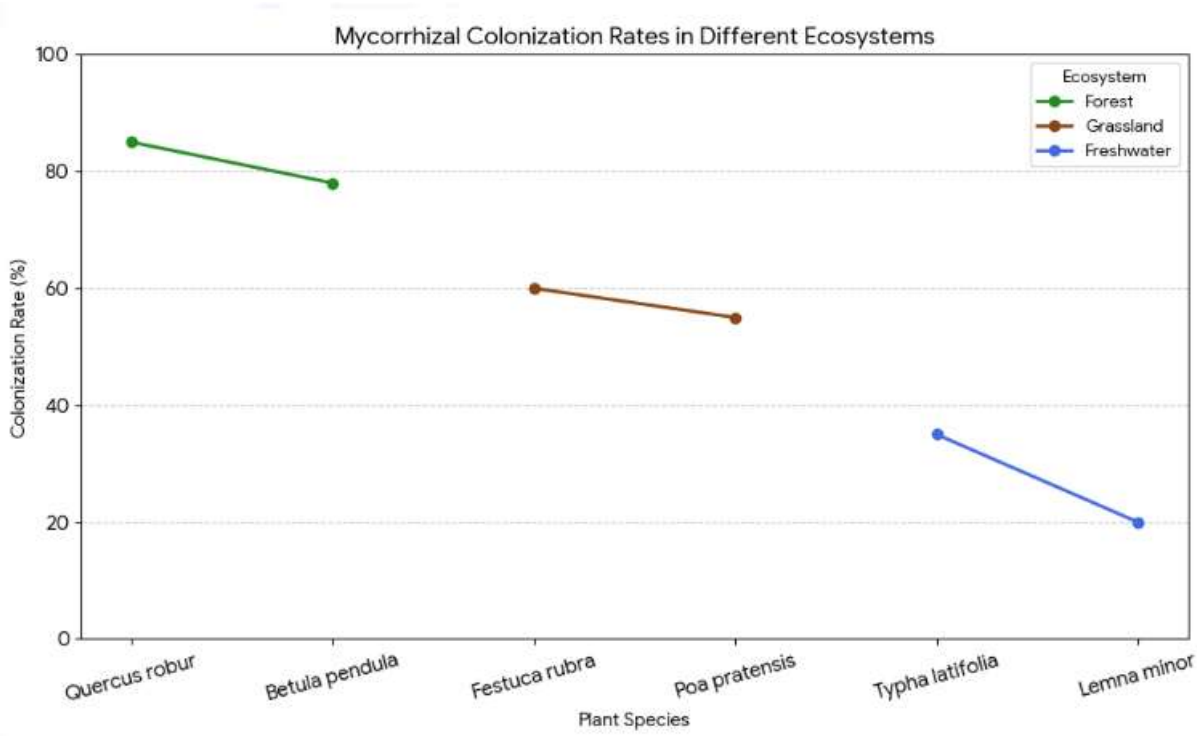

Figure 2: **Mycorrhizal Colonization Rates in Different Ecosystems**

The percentage of colonization of selected plant species in freshwater, grasslands, and forests in a line graph.

The line graph shows a significant difference of forest and fresh water ecosystems proving that environmental factors have a strong influence on symbiotic interactions. Colonization of forests is associated with increased nutrient uptake and growth of plants whereas low colonization of aquatic plants implies alternative nutrient uptake mechanisms.

Animal–Fungi Interactions

Small mammals and insects were observed to feed on fruiting bodies of fungi frequently and engage in dispersal of their spores. Sporer of fungi was recorded to be carried to new locations by herbivores, like the squirrels.

Table 3: Observed Animal–Fungi Interactions

Animal Species	Interaction Type	Frequency of Observation
Squirrel (Sciurus vulgaris)	Spore dispersal	15
Deer (Cervus elaphus)	Consumption	10
Termites (Macrotermes)	Decomposition	22
Beetles (Coleoptera)	Spore transport	18

The table indicates that the insects and mammals are active participants in the fungal life cycle either by the dispersal of spores or the break-down of organic matter. Termites are also very important in recycling of the nutrients as they decompose the fungus that is beneficial to the soil. These interactions illustrate that fungi are significant in maintaining animal populations and nutrient cycles of the ecosystems.

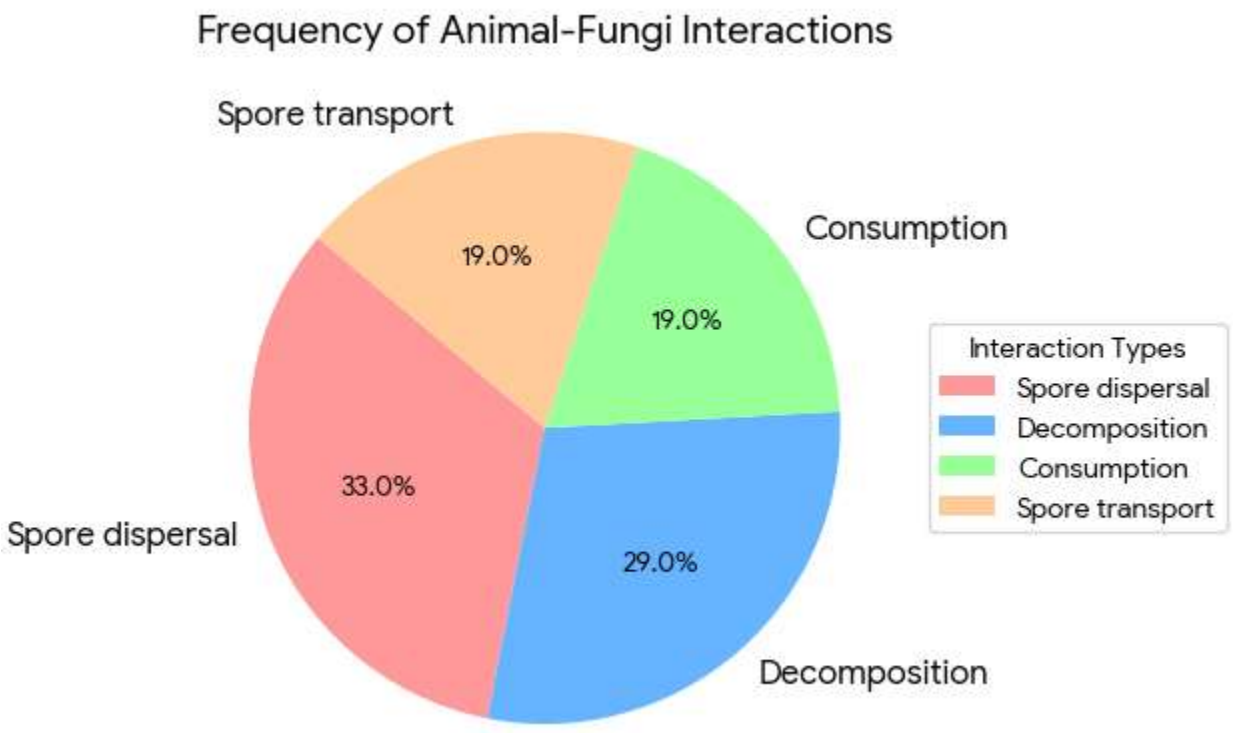

Figure 3: **Frequency of Animal–Fungi Interactions**

A pie chart of the percentage distribution of the various types of interaction among the observed species of animals.

The pie chart shows that the most common animal–fungi interactions are decomposition and spore transport, so their significance in the ecology is emphasized. Herbivores consume them less often but also play a crucial role in dispersal and seed–fungi networks and as such the multifaceted aspect of fungi in ecosystem functioning is emphasized.

Fungal Enzyme Activity and Decomposition

The enzyme activity of isolated fungal species in breaking down leaf litter was measured in laboratory. Forest fungi also exhibited a high level of laccase and cellulase activities.

Table 4: **Average Enzymatic Activity (Units/mL) in Fungal Species**

Fungal Species	Laccase Activity	Cellulase Activity
Amanita muscaria	45	38
Claviceps purpurea	30	25
Allomyces anomalus	20	18

The forest fungi had the greatest enzymatic activity that showed effective decay of organic matter. Grassland and freshwater fungi were less enzymatic implying that nutrient cycling was slow in these environments. The outcomes highlight the critical importance of fungal enzymes in ensuring soil fertility and productiveness of an ecosystem.

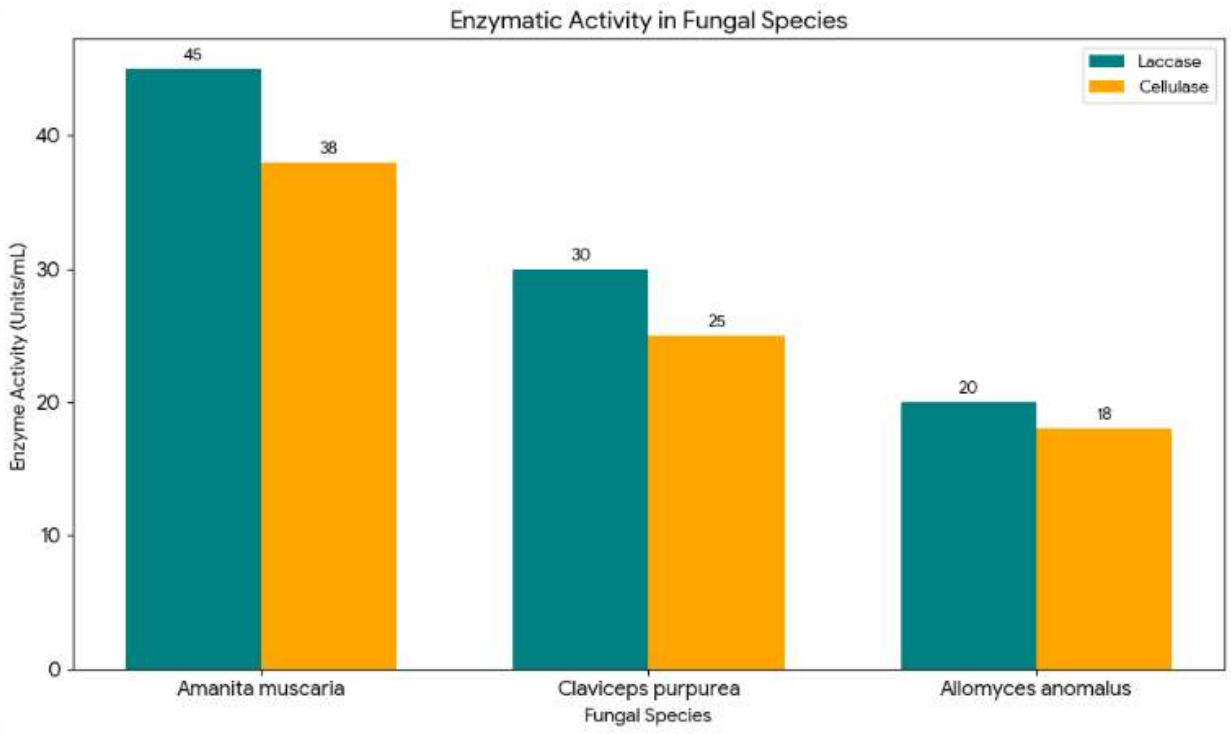

Figure 4: Enzymatic Activity in Fungal Species

A bar chart with clustered values of the three fungal species comparing the activity of the fungi in the activities of laccase and cellulase.

The table results are supported by the bar chart, which indicates that Amanita muscaria is more active in its enzyme characteristics, which is likely the reason why Amanita muscaria has high rates of decomposition and nutrient cycling in forest environments. Reduced activity of aquatic fungi is associated with low levels of substrate and rate of decomposition.

Integrated Ecosystem Interaction Network

In order to see the complicated connections among fungi, plants, and animals, a network of interaction was drawn on the basis of field and laboratory data.

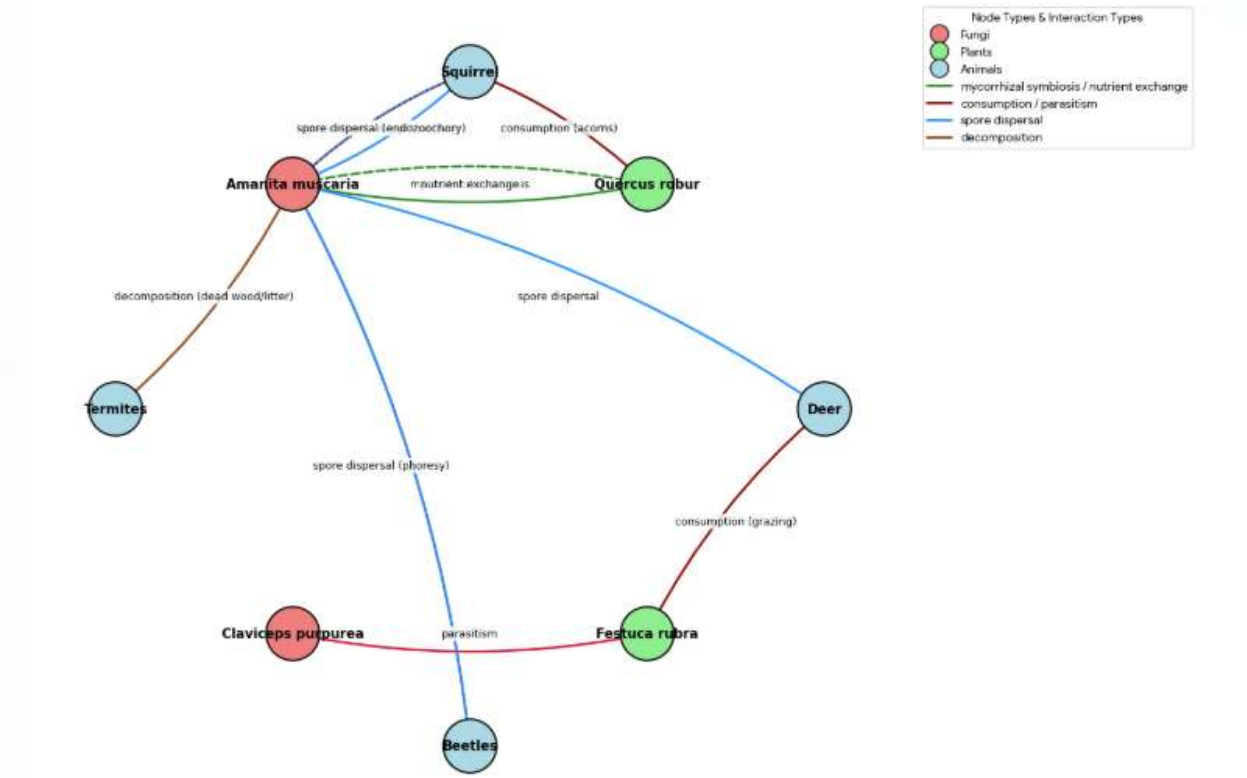

Figure 5: **Fungi–Plant–Animal Interaction Network**

A network graph with nodes depicting fungal, plant and animal species and edges depicting interactions identified.

The interaction network confirms that fungi are central nodes that connect the interaction between plants and animals in many ways. Forest ecosystems exhibited a high degree of connectivity, which implied an extensive mutualistic and decomposing network. Connection between grasslands was moderate whereas the freshwater ecosystems exhibited thin contact. The network indicates how essential fungi are in the stability of the ecosystem and the maintenance of biodiversity.

Discussion

The results of the present work support the concept that fungi are core and dynamic in the ecosystem functioning as a result of their interactions with both plants and animals. The found distribution and diversity of fungus species in ecosystems indicate that they are flexible and have ecological significance in ensuring a balance in the environment. The findings are congruent with the prior studies which underline the fact that fungi are the important intermediaries connecting various elements of the ecosystem, which promotes the circulation of nutrients and energy. The resulting high diversity especially in forest ecosystems can be used to argue that complex habitats offer good conditions to fungi to grow and interact networks which later increase stability and resilience of the ecosystem (Costa et al., 2025; Moonjely, 2022).

The discussion on plant–fungi interactions, particularly mycorrhizal associations, proves that they are very important in promoting plant health and productivity. The colonization rates of forest plant species are high suggesting that these mutualistic relationships are capable of improving nutrient acquisition and stress resistance. The results are in line with those of the studies that indicate that fungal symbiosis has a strong impact on plant performance and ecosystem productivity. In addition to this, the fact that colonization varies across ecosystems indicates that environmental factors including soil content and moisture are determining factors in defining such interactions. This can be corroborated in the bigger view of plant–fungi interaction as dynamic and reacting to ecological shifts (Priyashantha et al., 2023; Zanne et al., 2020).

Another important element that the study brings out is the ecological importance of fungi–animal interactions that have been typically underexplored in ecological studies. The process of spore

dispersal and consumption by animals has been shown by observations of spore dispersal and fungi consumption to be involved in the reproduction and spatial distribution of fungi. Fungi in turn are ecologically and nutritionally beneficial to animal species, and have a symbiotic relationship. These results are consistent with the recent literature that emphasizes more focus on fungal–animal interactions because they affect biodiversity and ecosystems. Also, the issue of fungi as sources of food and pathogens shows their dual effect on animal populations and the ecological balance (Wang, 2020; Iliev et al., 2024).

The findings in the framework of the ecosystem services and applied ecology highlight the significance of fungi in agriculture and environmental sustainability. The enzyme activities in fungal species highlight the fact that they are needed in the breakdown and recycling of nutrients that promote soil fertility and plant growth. This is in line with the past studies which show the potential of fungi in the use as biofertilizers and biocontrol agents in sustainable agriculture. Simultaneously, the study also recognizes the problem of the pathogenic fungi that have to be treated with cautiousness to reduce the adverse effects on crops. These data verify the dual ecological position of fungi as useful and harmful organisms in the agricultural system (Yuvaraj and Ramasamy, 2020; Zhang et al., 2020).

Lastly, the incorporation of both functional and biodiversity-oriented methodologies gives a more in-depth insight into the role of fungi in the processes in the ecosystem. The relationships measured between the diversity of fungi and the functionality of the ecosystem prove the thesis that the greater biodiversity the greater the stability and productivity of the ecology. This is in agreement with the recent progress in the fungal functional ecology that highlights the value of

using traits as a predictive of how an ecosystem responds to changes in the environment. In addition, increasing awareness of fungi in environmental policy illuminates their possible contribution to the solutions of global problems like climate change and loss of biodiversity. These results indicate that further investigation is necessary and fungi should be involved in conservation and sustainability plans (Põlme et al., 2020; Runnel et al., 2025; Hickman and Atherton, 2024).

Conclusion

The interrelations in which fungi are involved with plants and animals make fungi crucial and diverse components of the ecosystem because they are the vital agents of ecological balance and sustainability. The article has highlighted the nutrient cycling, growth of plants due to symbiotic associations and in animal life through food webs and ecological associations, such as spore dispersion. These interacting functions reveal that fungi are not isolated systems but they belong to a complex ecological system that sustains the biodiversity and ecosystem functioning of different habitats.

In addition, the conclusions indicate the importance of learning more about the diversity of fungi and ecological relationships in order to address the problems of the environment and the need to be more sustainable in their actions. The fungi would have very high chances of increasing the fertility of soil, the strength of plants and ecosystem stability in the natural ecosystem or in agriculture. Therefore, the need to study and preserve fungi should be enhanced to ensure that

the health and fitness of the ecosystems are maintained in the long run to offer policy options in the future with regard to environmental management and its sustainability.

References

Bahram, M., & Netherway, T. (2022). Fungi as mediators linking organisms and ecosystems. FEMS microbiology reviews, 46(2), fuab058.

Costa, L. A. M., Sousa, F. H. A., Carvalho, E. L., Bertazzo-Silva, F. A., Velloso, J. R. P., Velloso, M. A. P., ... & Putzke, J. (2025). Fungi associated with other organisms: diversity, interactions and ecological importance. In The Diversity of the Fungal World. IntechOpen.

Elliott, T. F., Truong, C., Jackson, S. M., Zúñiga, C. L., Trappe, J. M., & Vernes, K. (2022). Mammalian mycophagy: a global review of ecosystem interactions between mammals and fungi. Fungal Systematics and Evolution, 9(1), 99-159.

Hickman, K. J. E., & Atherton, K. F. (2024). Fungi are the future: Realizing the potential of fungi in policy. MIT Sci. Policy Rev, 5, 5-19.

Iliev, I. D., Brown, G. D., Bacher, P., Gaffen, S. L., Heitman, J., Klein, B. S., & Lionakis, M. S. (2024). Focus on fungi. Cell, 187(19), 5121-5127.

Moonjely, S. (2022). Fungi: essential elements in the ecosystems. In The impact of climate change on fungal diseases (pp. 19-35). Cham: Springer International Publishing.

Põlme, S., Abarenkov, K., Henrik Nilsson, R., Lindahl, B. D., Clemmensen, K. E., Kauserud, H., ... & Tedersoo, L. (2020). FungalTraits: a user-friendly traits database of fungi and fungus-like stramenopiles. Fungal diversity, 105(1), 1-16.

Priyashantha, A. H., Dai, D. Q., Bhat, D. J., Stephenson, S. L., Promputtha, I., Kaushik, P., ... & Karunarathna, S. C. (2023). Plant–fungi interactions: where it goes?. Biology, 12(6), 809.

Runnel, K., Tedersoo, L., Krah, F. S., Piepenbring, M., Scheepens, J. F., Hollert, H., ... & Bässler, C. (2025). Toward harnessing biodiversity–ecosystem function relationships in fungi. Trends in Ecology & Evolution, 40(2), 180-190.

Sudharsan, M. S., Rajagopal, K., & Banu, N. (2023). An insight into fungi in forest ecosystems. In Plant mycobiome: diversity, interactions and uses (pp. 291-318). Cham: Springer International Publishing.

Wang, C. (2020). Grand challenges in the research of fungal interactions with animals. Frontiers in Fungal Biology, 1, 602032.

Yuvaraj, M., & Ramasamy, M. (2020). Role of fungi in agriculture. Biostimulants in plant science, 1, 1-12.

Zanne, A. E., Abarenkov, K., Afkhami, M. E., Aguilar-Trigueros, C. A., Bates, S., Bhatnagar, J. M., ... & Treseder, K. K. (2020). Fungal functional ecology: bringing a trait-based approach to plant-associated fungi. Biological Reviews, 95(2), 409-433.

Zhang, Y., Li, S., Li, H., Wang, R., Zhang, K. Q., & Xu, J. (2020). Fungi–nematode interactions: Diversity, ecology, and biocontrol prospects in agriculture. Journal of Fungi, 6(4), 206.

Dealing with realistic first–order differential equation modelling problems.

Maha S ALibrahimi[1]

[1]AL-furat AL-Awsat University- Najaf Technical Institute, Najaf, Iraq, maha.salah.inj@atu.edu.iq

Abstract

A differential equation is a mathematical equation that relates a function with its derivatives. In this study we used the solution of differential equations to a couple of real-life situations to show how efficient or effective differential equations are. The outcomes of the above applications suggest that the differential equation has a unique solution even though it has been solved in many of the above applications.

Keywords

Differential equations and first order differential equations modelling.

Introduction

Classification of Differential Equations [6,9]

The purpose of this article is to examine the main ideas of effective differential equations and also give some good methods of resolving the equation or, at the very least, approximating them. Let's review some basic methods of classification of differentials equations to prepare for what is to follow.

1. A person discovers that the cloud's peak height angle is 60 degrees. The differential equation is called the conventional one if the function (u) involves only one variable (t) and is expressed as u = u(t). An equation is called partial (u = u(x, t)) if u has two or more variables that are t and x.

2. Occupation Name.

The biggest derivative of differential equations determines their order..

3. Diploma.

The highest exponent of the derivative is used to find the degree of a differential equation..

4. Linear and nonlinear both (1)

The linearity of a differential equation is another important idea. Nonlinear problems usually are (i.e. we cannot be explicitly answered unless under very specific circumstances) and linear problems are relatively (i.e. an explicit answer may be discovered). An ordinary differential equation for y(t) of order n, if can be put in the above form, then it is linear.

$$a_n(t)\frac{d^n y}{dt^n} + a_{n-1}(t)\frac{d^{n-1} y}{dt^{n-1}} + \cdots + a_1(t)\frac{dy}{dt} + a_0(t)y = f(t)$$

i.e. The only thing present is the multiple of 'y'. If f (t) is 0, the linear equation is said to be homogeneous, and if it is not, it is said to be inhomogeneous.

Initial–Value and Boundary–Value Problems[4]

Initial–value issue is a differential equation that has conditions on the unknown function, as well as on its derivatives, at the same value of the independent variable. The auxiliary condition is the first group of stipulations. The boundary conditions are the sub–conditions assigned by fixing the values of several independent variables in the boundary value problem.

Types of Differential Equations in First Order. [6,8]

1. Separable differential equation.

M(x,y)=−f(x,y) and N(x,y)=1 may be chosen always, even if not unique. A differential equation is separable if and only if M is a solely x–dependent function and N is a solely y–dependent function. The reason or cause is the differential form..

$$M(x)\,dx + N(y)\,dy = 0,$$

Moreover, the differential approach lessens the distinction between independent and dependent variables and has improved symmetry.

The integration of functions M and N can assist in solving a separable problem.

2. The equation is a homogeneous kind of differential equation**[3]**.

$$M(x,y)\,dx + N(x,y)\,dy = 0,$$

If both functions share the same degree of homogeneity, they are termed homogeneous functions. It may be expressed as a function of x, but it is not homogeneous in the sense that it cannot be expressed as a function of x and y. One way to make an equation separable is substitution.

Forming(Modeling) Differential Equation[5]

The chapter does not aim to give detailed prescriptions for the representation of every physical situation. Spending an entire semester studying modeling won't be sufficient. Through this segment I would like to give you a primer to the modelling process and what the modelling is. Three allusions will occur regarding falling bodies, population issues, and mixing problems.

If we drop these assumptions, we will run into difficulties with the issues- difficulties that are beyond the scope of this discussion and, in most cases, beyond the course. Given all of this, we would still have to do a fair bit of assumption which doesn't remotely hover near the truth for most part. In this case, let's.

Applications

This book includes applications of first order differential equation examples, particularly related to exponential growth exponential decay.

***Issues with Growth and Decay**:*

The changing amount of material, denoted by N(t), is called the rate of growth dN/dt. The rate at which the amount of drug present in the system changes per unit time is termed as its disappearance rate:

$\frac{dN}{dt}$ =Kt

N(t) is the proportionality constant. Now, even if N(t) is wrong in population census situations, even so, it gives a pretty good estimate of physical laws governing this system [2,7]. N(t) if K is a discrete integer-valued function. The continuity of K enables it to be described by a time function since it is differentiable.

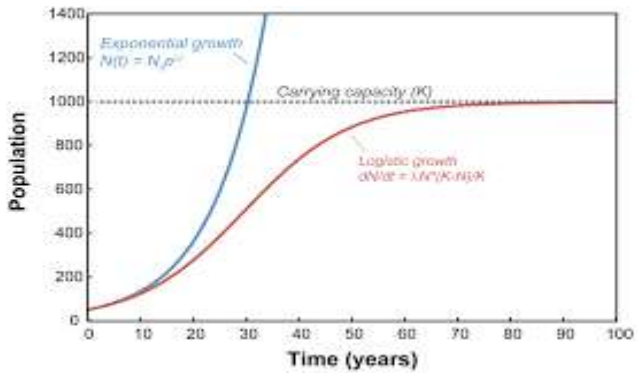

Exponential Growth

Environmental scientists analyze the growth rate for f(x) = abx, b>0.

Exampel:

The population of a town increases 15% every year. Consider How Many People will Live Here in Five Years If there are currently 5000 People in This city.

Solve:

First, calculate how much the population is expected to grow using an equation.

Let it be: initial value a = 5000, growth rate r = 15%, time in years x = 5

$f(x) = a(1 + r)^x$

$= 5000(1 + 0{,}15)^x$

$=5000(1{,}15)^x$ So the exponential growth function is.

The second step: we find the expected population after 5 years

$f(x) = 5000(1{,}15)^x$

$=5000(1{,}15)^5$ So it is expected that the population will be

=10056.79

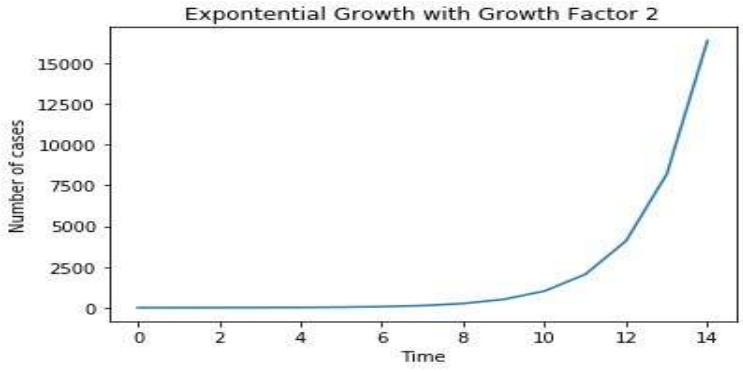

Exponential Decay

Environmental scientists use the formula f(x)= ab^x, where 0 < b< 1, for describing rate of decline of a growing quantity.

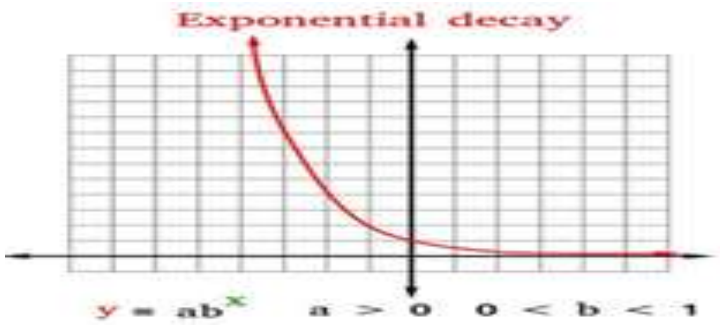

Exampel:

As per United States 2000 Census, Campbell County, Kentucky population was 88647, a decline rate of -0.3%. If this trend continues, with verpopulations reaching C124, derive the equation for the population since the year 2000..

Solve: $r = \frac{0.3}{100}$, a =0,003 , x =10

$f(x) = a(1-r)^x$

$= 88{,}647(1-0.003)^{10}$

So it is expected that the population will be

$f(x) = 86{,}023$

References

[1]An introdcion to ordinary Differential Equations/james C.robinson/Cambrideg 2004.

[2]An introduction to Differential Equations with Applications /World scientific /Harold cohen /Daniel gallup2020.

[3]Atextbook on ordinary Differential Equations / second Editions/shair Ahmad Antonio ambroseti / springer 2015.

[4] Differential Equations Larsen &kellerEducation , sofia Lynch2022.

[5] Differential Equations / paul Dawkins 2007.

[6] Elementary Differential Equations and Boundary value problems /ten Editions/William E.boyce / john Richard C.Diprima2012.

[7]Elementary Differential Equations/Richard E,phillp Edward Bedieut,Earl David Rainville Bedient,prentice Hall 1997.

[8]Hand book of ordinary Differential Equations Exactsolution methods and problems /taylor &francis group ,llc /2018.

[9]Introduction to Compvtation and Modeling for Differential Equations /second Edition /Lennart Edsberg /John Wiley &Sons ,2016.

Some Topological Indices of The Co-prime Power Order Graph

Hasan H. Mushatet [1]

[1]**General Directorate of Education in Thi-Oar**, **Ministry of Education**, **Thi-Qar**, **Iraq**, hasanalhelaly@utq.edu.iq

Abstract

In the context of a particular group, the co-prime power order graph referred to as G, denoted as β_G, is characterized by its vertex set $V(G)$. The vertices x and y in G are adjacent if and only if $gcd(|x|,|y|) = p^m$, for a prime number p and m is a nonnegative integer number. This study research focuses on analyzing and evaluates specific topological indices associated with the graph including the first and second Zagreb indices, and the Wiener & hyper Wiener indices. During this paper the researcher examines these indices in relation the graph β_G of a finite group G which including several types of groups such as cyclic groups, dihedral groups, generalized quaternion groups, and other group families. By investigating these topological indices, the paper aims to provide insights into the structural properties of co-prime power order graphs, contributing to a deeper understanding of the relationships among different groups and their graphical representations. This comprehensive analysis of the indices could have implications for further research in group theory and graph theory, potentially leading to new discoveries in these mathematical fields.

Keywords: Cyclic Group, Dihedral Group, Generalized Quaternion Group, Co-prime Graph, Topological Indices.

1. Introduction

A graph was used in mathematics from a long time to study algebra's structures as semi groups, groups, and quasi groups. The relationships between components of these structures was noted clearly. Especially, the type of graph which was interested on the coprime graph of a finite group. The researchers may found more results about the properties of the coprime graph, and they compared these results between the groups and order of their elements. A coprime graph has defined by Sattanathan & Kala as a graph Γ_G of a group G such that each two vertices $x, y \in \Gamma_G$ are adjacent if and only if $\gcd(|x|, |y|) = 1$ (Muthulakshmi et al., 2024). Subsequently, Ma et al are looked into the properties of co-prime graph (Hao et al., 2022; Syarifudin et al., 2021). After that some researchers have worked on the characteristics of Γ_G associated with finite cyclic groups and dihedral groups. In addition, the researchers extend a graph Γ_G into the coprime order graph which denoted by $\theta(G)$ that defined as any two vertices $u, v \in \Gamma_G$ are adjacent if and only if $\gcd(|u|, |v| = 1 \; or \; prime \; integer \; number$ (Banerjee, 2019; Saini et al., 2020). A lot of researchers are studied some properties of graph $\theta(G)$ such as its completeness, planarity, and the connectivity of finite groups (Saini et al., 2020; Milne, 2022). More references give definitions and properties of p-groups,

complete graphs, and planar graphs (West, 2018). In (Mushatet & Talebi,2025) , the researchers present the notion of the co-prime power order graph β_G . These studies seek to broaden the comprehension of co-prime graphs and investigate their properties in greater depth. In (Alimon et al.,2020), (Gutman et al.,2020), and (Siti Zahidah et al.,2021) the readers can find a lot of definitions and notions about the topological indices and their properties on some types of graphs, and these indices are very useful to study the structures of chemical compound, and its physical, chemical, and biological properties. The researchers can used topological indices to describe the mathematical models and how to use these models.

This study has been acknowledged as follows: In Section 2, the study begin by defining and explaining some basic terms, theorems, lemmas, and corollaries that will be used throughout this paper. In Section 3, the researcher calculate the first and second Zagreb indices of the graph β_G of a finite group G. Section 4 establish to find the Wiener and Hyper Wiener indices of the finite group's graph β_G. In this paper, the formulas employed to calculate the topological indices of the graph β_G are delineated. The analyze was focus on graph β_G of the cyclic group, dihedral group, and generalized quaternion group. Finally, the paper presented the conclusion of this work.

2. Material and Methods

This section presents an overview of the essential concepts and notations in group theory, graph theory, and topological indices employed in this study. Initially, foundational definitions and notations related to group theory will provided. A cyclic group G is defined as a group formed by the element $x \in G$, denoted as $< x >= G$, where x is referred to as the generator of G. Every cyclic group of order n is isomorphic to $\mathbb{Z}_n$. A group G is termed a $p-group$ if the order of each element is a power of the prime integer p. The dihedral group, represented as D_n, is defined as follows:

$D_n =< a, b | a^n = b^2 = e, bab = a^{-1} >, and\ |D_n| = 2n$ (Mushatet & Talebi,2025).

The generalized quaternion group is represented as Q_{4n}, and is defined as:

$Q_{4n} =< a, b | a^n = b^2 = e, bab = a^{-1} >, and\ |Q_{4n}| = 4n$ (Mushatet & Talebi,2025).

The subset $P \subseteq G$, such that $\forall x \in P \rightarrow |x| = p^m$, and it denoted by $P(G)$ (Mushatet & Talebi,2025).

A group G is called $\emptyset - group$ if any nontrivial element $x \in G$, then if any nontrivial element of $|x| = p^m$, for a prime number $p, m \in \mathbb{Z}^+ \cup \{0\}$.

First, the basic concepts and symbols used in graph theory will be covered. For any two vertices $x, y \in \Gamma$ are adjacent is referred to be a complete graph and is represented by K_n with n vertices (Hao et al., 2022) . Every element x in the complete graph K_n has a degree of $n-1$, and the number of edges is $(n(n-1))/2$. As an alternative, if graph Γ does not include a complete subgraph $K_5, K_{3,3}$, or any subdivision subgraph of $K_5, K_{3,3}$, it is referred to as a planar graph (Hao et al., 2022). Now, the idea of a co-prime power order graph of a group G, abbreviated as β_G will be addressed. A graph with vertex set

G, such that any two distinct elements $x, y \in G$ are connected if and only if $gcd(|x|, |y|) = p^m$, where p is a prime number and m is a non-negative integer (Mushatet & Talebi,2025) . If G is a $\emptyset - group$, then β_G is complete (Mushatet & Talebi,2025) . Let $n = p^m$, where p is a prime integer and m is greater than or equal to 1, $\mathbb{Z}_n$ is a $\emptyset - group$, as an example, if β_G considered(Mushatet & Talebi,2025) . Similarly, if $G = D_n$ considered, then G is a $\emptyset$ -group if and only if $n = p^m$, where m is greater than or equal to 1(Mushatet & Talebi,2025) . When $G = Q_{4n}$ considered, then G is a $\emptyset$ -group if and only if $n = 2^m$, where m is greater than or equal to 1 (Mushatet & Talebi,2025) . Let us now focus on the set of vertices of G. Let G be a group such that $|G| = n$, then $\forall x \in P(G)$ be satisfied $deg\ (x) = n - 1$ (Mushatet & Talebi,2025). In the case of a group G, let β_G represent its co-prime power order graph. The induced subgraph by $S \subseteq G$ is denoted by $\beta_G[S]$, and for any two vertices $x, y \in S$ are adjacent in β_G then $x\ and\ y$ are adjacent in $\beta_G[S]$ (Mushatet & Talebi,2025). The induced subgraph $\beta_G[G - P(G)]$ of the co-prime power order graph β_G is a null graph if and only if $|G| = p^\alpha q^\gamma$, for prime numbers p, q , and $\alpha, \gamma \in \mathbb{Z}^+$ (Mushatet & Talebi,2025). Some important definitions and notations on topological indices of a graph are now provided. The first Zagreb index of a graph Γ is denoted by $M_1\ (\Gamma)$, and define as:

$M_1\ (\Gamma) = \sum_{v \in V(\Gamma)} (\deg(v))^2$ (Alimon et al.,2020) .

The second Zagreb index of a graph Γ is denoted by $M_2\ (\Gamma)$, and define as:

$M_2(\Gamma) = \sum_{uv \in E(\Gamma)} \deg(u) \deg\ (v)$ (Alimon et al.,2020) . The Wiener index of a graph Γ is denoted by $W(\Gamma)$, and define as: $W(\Gamma) = \sum_{u,v \in V(\Gamma)} d(u, v)$, and $d(u, v)$ be the

distance between the vertices $u, and\ v$ (Gutman et al.,2020); Siti Zahidah et al.,2021) . The hyper-Wiener index of a graph Γ denoted by $WW(\Gamma)$ and define as :

$WW(\Gamma) = \frac{1}{2}[W(\Gamma) + \sum_{u,v\in V(\Gamma)}(d(u,v))^2]$, $d\ (u,v)$ is a distance between a vertices $x\ and\ y$ (Siti Zahidah et al.,2021).

3. Results and discussion

In this section, the first and second Zagreb indices, and the Wiener & hyper-Wiener Indices of the graph β_G of some finite group G are determined. Such as D_n, Q_{4n}, and $\mathbb{Z}_n$.

Now, the first and second Zagreb indices of the graph β_G are started:

Theorem 3.1: Suppose that there is a graph β_{D_n} of group D_n. If $n = pq, p, q$ are distinct prime numbers, then

(**i**) $M_1(\beta_{D_n}) = \sum_{v\in V(\beta_{D_n})}(\deg(v))^2 = m(2n-1)^2 + m^2(2n-m)$,

(**ii**) $M_2(\beta_{D_n}) = \sum_{uv\in E(\beta_{D_n})} \deg(u)\deg(v) = \frac{m(m-1)}{2}(2n-1)^2 + m(2n-1)$

such that $|P(D_n)| = m$.

Proof: (**i**) Suppose that $n = pq$, and $P(D_n) = \{x \in D_n || x| = 1\ or\ 2\ or\ p\ or\ q\}$.

Then $\deg(x) = 2n-1$, for all $x \in P(D_n)$ Let $A = \{y \in D_n |\ |y| = pq\}$. Then $D_n = P(D_n) \cup A$, and $\beta_{D_n}[A]$ is a null induced subgraph of β_{D_n}, and every vertex $y \in \beta_{D_n}[A]$ be adjacent to all vertices of $\beta_{D_n}[P(D_n)]$. Therefore $deg\ (y) = m$ for all $y \in A$. It follows that:

$$M_1(\beta_{D_n}) = \sum_{v \in V(\beta_{D_n})} (\deg(v))^2 = \sum_{v \in \beta_{D_n}[P(D_n)]} (\deg(v))^2 + \sum_{v \in \beta_{D_n}[A]} (\deg(v))^2$$

$$= m(2n-1)^2 + m^2(2n-m).$$

(**ii**) For any vertex $x \in P(D_n)$, $deg\ (x) = 2n-1$ holds, and for every vertex $y \in A\ deg\ (y) = m$. Since $\beta_{D_n}[P(D_n)]$ is a complete of β_{D_n}, and $\left|E(\beta_{D_n}[P(D_n)])\right|$is equal to $(m(m-1))/2$. Moreover, each vertex of $\beta_{D_n}[A]$ is adjacent with all vertices of $\beta_{D_n}[P(D_n)]$. According to the definition of Zagreb indices of a connected graph it follows that:

$M_2(\beta_{D_n}) = \sum_{uv \in E(\beta_{D_n})} \deg(u)\deg(v)$

$$= \sum_{uv \in E(\beta_{D_n}[P(D_n)])} \deg(u)\deg(v) + \sum_{u \in (\beta_{D_n}[P(D_n)]), v \in (\beta_{D_n}[A]), uv \in E(\beta_{D_n})} \deg(u)\deg(v)$$

$$= \frac{m(m-1)}{2}(2n-1)^2 + m(2n-m)(2n-1). \qquad \blacksquare$$

Theorem 3.2: Suppose that $\beta_G = K_n$ is the complete graph with n vertices. Then it follows that:

i) $M_1(K_n) = \sum_{v \in V(K_n)} (\deg(v))^2 = n(n-1)^2$;

ii) $M_2(K_n) = \sum_{uv \in E(K_n)} \deg(u)\deg(v) = \frac{n(n-1)^3}{2}$

Proof: i) Suppose that K_n is the complete graph. Then $deg\ (x) = n-1$, for each $x \in K_n$. According to Zagreb indices of a connected graph then it is obtained that:

$$M_1 K_n) = \sum_{v \in V(K_n)} (\deg(v))^2 = n(n-1)^2$$

iii) Suppose that K_n is The complete graph. Then $deg\ (x) = n-1$, and

$|E(K_n[P(D_n)])| = \frac{n(n-1)}{2}$. So with respect to Zagreb indices of a connected graph then it is obtained:

$M_2(K_n) = \sum_{uv \in E(K_n)} \deg(u) \deg(v) = \frac{n(n-1)}{2} \times (n-1)(n-1) = \frac{n(n-1)^3}{2}$

■

Theorem 3.3: Suppose there is β_G of a finite group G, then the following facts are hold:

(i) When $G = \mathbb{Z}_n, n = p^m, p \text{ is prime}, m \geq 1$, then

1) $M_1(\beta_{\mathbb{Z}_n}) = \sum_{v \in V(\beta_{\mathbb{Z}_n})} (\deg(v))^2 = n(n-1)^2$

2) $M_2(\beta_{\mathbb{Z}_n}) = \sum_{uv \in E(\beta_{\mathbb{Z}_n})} \deg(u) \deg(v) = \frac{n(n-1)^3}{2}$

(ii) When $G = D_n,\ n = p^m, p \text{ is prime}, m \geq 1$, then

1) $M_1(\beta_{D_n}) = \sum_{v \in V(\beta_{D_n})} (\deg(v))^2 = (2n)(2n-1)^2$,

2) $M_2(\beta_{D_n}) = \sum_{uv \in E(\beta_{D_n})} \deg(u) \deg(v) = n(2n-1)^3$

(iii) When $G = Q_{4n},\ n = 2^m, m \geq 1$, then

1) $M_1(\beta_{Q_{4n}}) = \sum_{v \in V(\beta_{Q_{4n}})} (\deg(v))^2 = (4n)(4n-1)^2$,

2) $M_2(\beta_{Q_{4n}}) = \sum_{uv \in E(\beta_{Q_{4n}})} \deg(u) \deg(v) = 2n(4n-1)^3$

Proof:

(**i**) Suppose that $G = \mathbb{Z}_n, n = p^m$. Then $\beta_{\mathbb{Z}_{p^m}}$ is the complete graph with n vertices [Theorem 3.1,8]. By Theorem 2 then it is obtained that:

1) $M_1(\beta_{\beta_{\mathbb{Z}_{p^m}}}) = \sum_{v \in V(\beta_{\beta_{\mathbb{Z}_{p^m}}})} (\deg(v))^2 = (n)(n-1)^2$.

2) $M_2(\beta_{\mathbb{Z}_n}) = \sum_{uv \in E(\beta_{\mathbb{Z}_n})} \deg(u) \deg(v) = \frac{n(n-1)^3}{2}$.

(**ii**) Suppose that $G = D_n,\ n = p^m$. Then β_{D_n} is the complete graph with n vertices [Theorem 3.3,8]. Similarly the following are satisfied:

1) $M_1(\beta_{D_n}) = \sum_{v \in V(\beta_{D_n})} (\deg(v))^2 = (2n)(2n-1)^2$

2) $M_2(\beta_{D_n}) = \sum_{uv \in E(\beta_{D_n})} \deg(u) \deg(v) = n(2n-1)^3$

(**iii**) Let $G = Q_{4n},\ n = 2^m$. Then $\beta_{Q_{4n}}$ is the complete graph[Theorem 3.5,8], and similarly it is obtained:

1) $M_1(\beta_{Q_{4n}}) = \sum_{v \in V(\beta_{Q_{4n}})} (\deg(v))^2 = (4n)(4n-1)^2$

2) $M_2(\beta_{Q_{4n}}) = \sum_{uv \in E(\beta_{Q_{4n}})} \deg(u) \deg(v) = 2n(4n-1)^3$.

■

Theorem 3.4: Suppose that β_G is a co-prime power order graph of a finite group G. When $|G| = n = p^\alpha q^\gamma$ for p, q are distinct prime numbers, and α, γ are positive integers then

(**i**) $M_1(\beta_G) = \sum_{v \in V(\beta_G)} (\deg(v))^2 = m(n-1)^2 + m^2(n-m)$,

(**ii**) $M_2(\beta_G) = \sum_{uv \in E(\beta_G)} \deg(u) \deg(v) = \frac{m(m-1)}{2}(n-1)^2 + m^2(n-1)$

such that $|P(G)| = m$.

Proof: (**i**) Suppose that $|G| = n = p^{\alpha}q^{\gamma}$, and $P(G) = \{x \in G||x| = 1 \ or \ p^{\alpha_1} \ or \ q^{\alpha_2},$ $\alpha_1, \alpha_2$are positive integers }. Then $\deg(x) = n - 1$, for all $x \in P(G)$ Let $A = G - P(G) = \{y \in G \mid |y| = p^{\gamma_1} q^{\gamma_2}, for \ \gamma_1, \gamma_2$are positive integers$\}$, then $G = P(G) \cup A$. By [Theorem 5.1, 8] it follows $\beta_G[A]$ is a null induced subgraph, and for every vertex $y \in \beta_G[A]$ is adjacent to all vertices of $\beta_G[P(G)]$. Therefore $deg\,(y) = m$. So by definition of first Zagreb index of a connected graph then it is obtained :

$$M_1(\beta_G) = \sum_{v \in V(\beta_G)} (\deg(v))^2 = \sum_{v \in (\beta_G[P(G)])} (\deg(v))^2 + \sum_{v \in (\beta_G[A])} (\deg(v))^2$$

$$M_1(\beta_G) = m(n-1)^2 + m^2(n-m).$$

(**ii**) For any vertex $x \in \beta_G[P(G)]$ there is $deg\,(x) = n - 1$, and for every vertex $y \in \beta_G[A]$, $deg\,(y) = m$. Since $\beta_G[P(G)]$ is the complete induced subgraph of β_G, then the number of edges of $\beta_G[P(G)]$ is equal to $(m(m-1))/2$. Moreover, every vertex in $\beta_G[A]$ is adjacent with all elements of $\beta_G[P(G)]$. According to Zagreb indices of a connected graph then it is obtained that:

$$M_2(\beta_G) = \sum_{uv \in E(\beta_G)} \deg(u)\deg(v) = \frac{m(m-1)}{2}(n-1)^2 + m(n-m)(n-1)$$

■

In the same context, the Wiener & hyper Wiener Indices of β_G when G is a finite group are computed. Basically, the Wiener index of β_G of D_n, Q_{4n}, and cyclic group $\mathbb{Z}_n$, and a group of order $p^{\alpha}\,q^{\gamma}, p \ and \ q$ are prime number is calculated:

Theorem 3.5: Suppose there is β_{D_n} the finite group D_n. If $n = pq,\ p, q$ are distinct prime numbers, then

$W(\beta_{D_n}) = \sum_{u,v \in V(\beta_{D_n})} \mathrm{d}(u,v) = \frac{m(m-1)}{2} + m(2n-m) + 2(2n-m)(2n-m-1)$.

where $|P(D_n)| = m$.

Proof: Suppose that $n = pq$. By definition, $P(D_n) = \{x \in D_n || x| = 1\ or\ 2\ \ p\ or\ q\}$. Since $\beta_{D_n}[P(D_n)]$ be complete graph of β_{D_n}, then $\left|E(\beta_{D_n}[P(D_n)])\right| = (m(m-1))/2$. Any two vertices $u, v \in \beta_{D_n}[P(D_n)]$ are adjacent, $and\ \ d(u,v) = 1$. Hence $\sum_{u,v \in V\beta_{D_n}[P(D_n)])} d(u,v) = 1 \times \frac{m(m-1)}{2} = \frac{m(m-1)}{2}$.

Now, suppose that $A = \{y \in D_n |\ |y| = pq\}, then\ \ D_n = P(D_n) \cup A$.

It follows that $\beta_{D_n}[A]$ is a null induced subgraph. Each vertex $u \in \beta_{D_n}[A]$ is adjacent to all vertices of $\beta_{D_n}[P(D_n)]$. It follows there are $m(2n-m)$ edges from $V(\beta_{D_n}[A])$ into $V(\beta_{D_n}[P(D_n)])$. So any vertex $u \in \beta_{D_n}[P(D_n)], v \in \beta_{D_n}[A]$ are adjacent and so distance $d(u,v) = 1$.

Therefore $\sum_{u \in V(\beta_{D_n}[P(D_n)]), v \in V(\beta_{D_n}[A])} \mathrm{d}(u,v) = 1 \times m(2n-m) = m(2n-m)$.

Since $\beta_{D_n}[A]$ is a null induced subgraph, then any two vertices $u, v \in \beta_{D_n}[A]$ are not adjacent, and there is a path $uw, wv, w \in \beta_{D_n}[P(D_n)]$ such that $d(u,v) = 2$.

Then $\sum_{u,v \in V(\beta_{D_n}[A])} \mathrm{d}(u,v) = 2 \times (2n-m)(2n-m-1) = 2(2n-m)(2n-m-1)$.

Thus $W(\beta_{D_n}) = \sum_{u,v\in V(\beta_{D_n})} \mathrm{d}(u,v) = \sum_{u,v\in V(\beta_{P(D_n)})} \mathrm{d}(u,v) + \sum_{u\in V(\beta_{D_n}[P(D_n)]),v\in V(\beta_{D_n}[A])} \mathrm{d}(u,v) + \sum_{u\in V(\beta_{D_n}[A]),v\in V(\beta_{D_n}[A])} \mathrm{d}(u,v) = \frac{m(m-1)}{2} + m(2n-m) + 2(2n-m)(2n-m-1)$. ■

Theorem 3.6: Suppose that $\beta_G = K_n$ is the complete graph of order n, then

$$W(K_n) = \sum_{u,v\in V(K_n)} \mathrm{d}(u,v) = \frac{n(n-1)}{2}$$

Proof: Let K_n be a complete graph, with n vertices. Then the number of edges of K_n is equal $to\ (n(n-1))/2$. Any two vertices $u, v \in K_n$ are adjacent, and $d(u,v) = 1$.

Therefore $W(K_n) = \sum_{u,v\in V(K_n)} d(u,v) = 1 \times \frac{n(n-1)}{2} = \frac{n(n-1)}{2}$.

Theorem 3.7: Suppose there is β_G of a finite group G, then all of following facts are satisfied:

i) If $G = \mathbb{Z}_n, n = p^m, p\ is\ prime, m \geq 1$, then

$W(\beta_{\mathbb{Z}_n}) = \sum_{u,v\in V(\beta_{\mathbb{Z}_n})} d(u,v) = \frac{n(n-1)}{2} n$

ii) If $G = D_n, n = p^m, p\ is\ prime, m \geq 1$, then

$W(\beta_{D_n}) = \sum_{u,v\in V(\beta_{D_n})} \mathrm{d}(u,v) = n(2n-1)$,

iii) If $G = Q_{4n}, n = 2^m, m \geq 1$, then

$W(\beta_{Q_{4n}}) = \sum_{u,v\in V(\beta_{Q_{4n}})} \mathrm{d}(u,v) = 2n(4n-1)$.

Proof: By [Theorem 3.1,8], [Theorem 3.3,8], and [Theorem 3.5,8] in all cases there is a complete graph. Then by Theorem 6 , all cases hold, and the proof is simple. ■

Theorem 3.8: Let β_G is a graph of a finite group G. If $|G| = n = p^{\alpha} q^{\gamma} for\ p \neq q$ are prime numbers, $\alpha, \gamma \in \mathbb{Z}^+$ then

$W(\beta_G) = \sum_{u,v \in V(\beta_G)} \mathrm{d}(u,v) = m(m-1) + 2m(n-m)$, where $|P(G)| = m$.

Proof: Suppose that $n = pq$, and $P(G) = \{x \in ||x| = 1\ or\ p^{\alpha_1}\ \ or\ q^{\gamma_1}, \alpha_1, \gamma_1 are\ positive\ inger\ numbers\}$.

Since $\beta_G\ [P(G)]$ is a complete null induced subgraph of β_G, for any two vertices $u, v \in \beta_G\ [P(G)], d(u,v) = 1$, and $|E(\beta_G\ [P(G)])| = \frac{m(m-1)}{2}$.

Hence $\sum_{u,v \in V(\beta_G[P(G)])} d(u,v) = 1 \times \frac{m(m-1)}{2} = \frac{m(m-1)}{2}$.

Now, suppose that $B = \{y \in G |\ |y| = p^{\alpha}\ q^{\gamma}\}$, then $G = P(G) \cup B$. It follows that $\beta_G\ [B]$ is a null induced subgraph. Then $\forall u \in \beta_G\ [B]$ be adjacent to $\forall y \in \beta_G\ [P(G)]$. It follows there are $m(n-m)$ edges from $V(\beta_G\ [B])$ into $V(\beta_G\ [P(G)])$. So any two vertices $u \in \beta_G\ [P(G)]$ and $v \in \beta_G\ [B]$ are adjacent and $d(u,v) = 1$.

Therefore $\sum_{u \in V(\beta_G[P(G)]), v \in V(\beta_G[B])} d(u,v) = 1 \times m(n-m) = m(n-m)$.

For any two vertices $u, v \in \beta_G\ [B]$, it follows $d(u,v) = 2$.

Hence

$$\sum_{u,v \in V(\beta_G[B])} d(u,v) = 2 \times (n-m)(n-m-1) = 2(2n-m)(n-m-1)$$

Thus $W(\beta_G) = \sum_{u,v\in V(\beta_G)} d(u,v) = \sum_{u,v\in V(\beta_G[P(G)])} d(u,v) + \sum_{u\in V(\beta_G[P(G)]),v\in V(\beta_G[B])} d(u,v) + \sum_{u,v\in V(\beta_G[B])} d(u,v)$

$= m(m-1)/2 + m(n-m) + 2(2n-m)(2n-m-1)$ ■

Theorem 3.9: Suppose that β_{D_n} be a graph of the group D_n. If $n = pq, p, q$ are distinct prime numbers, then

$$WW(\beta_{D_n}) = \frac{1}{2}\Big[W(\beta_{D_n}) + \sum_{u,v\in V(\beta_{D_n})} (\mathrm{d}(u,v))^2\Big]$$

$$= \frac{1}{2}\left[\frac{m(m-1)}{2} + m(2n-m) + 2(2n-m)(n-m-1) + \frac{m(2m-1)}{2} + m(2n-m) + 4(2n-m)(n-m-1)\right]$$

$$= \left[\frac{m(2m-1)}{2} + m(2n-m) + 3(2n-m)(2n-m-1)\right]$$

where $|P(D_n)| = m$.

Proof: Let $n = pq$. By definition, $P(D_n) = \{x \in D_n || x| = 1 \text{ or } 2 \text{ or } p \text{ or } q\}$.

By Theorem 5, then $W(\beta_{D_n}) = (m(m-1))/2 + m(2n-m) + 2(2n-m)(2n-m-1)$ is holded.

For any two vertices $u, v \in P(D_n), d(u,v) = 1, (d(u,v))^2 = 1$. Each vertex of $P(D_n)$ is adjacent to all vertices of $B = D_n - P(D_n)$. Also, for any two vertices $u, v \in B, d(u,v) = 2$.

Hence

$$\sum_{u,v\in V(\beta_{D_n})} (\mathrm{d}(u,v))^2$$

$$= \sum_{u,v\in V(\beta_{D_n}[P(D_n)])} (\mathrm{d}(u,v))^2$$

$$+ \sum_{u\in V(\beta_{D_n}[P(D_n)]),v\in V(\beta_{D_n}[B])} (\mathrm{d}(u,v))^2 + \sum_{u,v\in V(\beta_{D_n}[B])} (\mathrm{d}(u,v))^2$$

Therefore

$WW(\beta_{D_n}) = \frac{1}{2}[W(\beta_{D_n}) + \sum_{u,v\in V(\beta_{D_n})}(\mathrm{d}(u,v))^2] = \frac{1}{2}\left[\frac{m(m-1)}{2} + m(2n-m) + 2(2n-m)(2n-m-1) + \frac{m(m-1)}{2} + m(2n-m) + 4(2n-m)(n-m-1)\right] = \left[\frac{m(2m-1)}{2} + m(2n-m) + 3(2n-m)(2n-m-1)\right]$. ■

From Theorems 3.6,3.7, and the definition of Hyper Wiener index it follows:

Corollary 3.10: Suppose there is β_G of a finite group G, and $|G| = n$. Then the following statements are hold:

i) $W(\beta_{D_n}) = WW(\beta_{D_n}), when\ n = p^m$.

ii) $W(\beta_{Q_{4n}}) = WW(\beta_{Q_{4n}}), when\ n = 2^m$.

iii) $W(\beta_{\mathbb{Z}_n}) = WW(\beta_{\mathbb{Z}_n}), when\ n = p^m$.

iv) $W(\beta_G) = WW(\beta_G), when\ n = p^m$.

6. Conclusion

In this work, some topological indices of the co-prime power order graph of the finite groups like dihedral group, cyclic group, and generalized quaternion group was determined . In the beginning the researchers found $M_1(\beta_G)$, $M_2(\beta_G)$ depended on the order of the finite group G and $|P(G)|$ when β_G is not complete while $M_1(\beta_G)$, $M_2(\beta_G)$ depended on the order of the finite group G when β_G is complete graph.

Also this study found the Wiener and Hyper Wiener indices of β_G of a finite group G depended on the same characters.

References

1. Muthulakshmi, R. M., Premalatha, D., & Lalitha, N. (2024). Independence number of order prime graph. Indian Journal of Science and Technology, 17(18), 1824–1827. https://doi: 10.17485/IJST/v17i18.542

2. Hao, S., Zhong, G., & Ma, X. (2022). Notes on the co-prime order graph of a group. Proceedings of the Bulgarian Academy of Sciences, 75(3), 340–348. https://doi.org/10.7546/CRABS.2022.03.03

3. Syarifudin, A. G., Nurhabibah, N., Malik, D. P., & Wardhana, I. G. A. W. (2021). Some characterization of coprime graph of dihedral group \(D_{2n}\). Journal

of Physics: Conference Series, 1722(1), 012051. https://doi.org/10.1088/1742-6596/1722/1/012051.

4. Banerjee, S. (2019). On a new graph defined on the order of elements of a finite group (arXiv:1911.02763). arXiv. https://doi.org/10.48550/arXiv.1911.02763

5. Saini, M., Khasraw, S. M. S., Sehgal, A., & Singh, D. (2020). On co-prime order graphs of finite abelian \(p\)-groups. Journal of Mathematical and Computer Sciences, 23(3), 196–202. http://dx.doi.org/10.22436/jmcs.023.03.03

6. Milne, J. S. (2022). Algebraic groups (1st ed.). Cambridge University Press. . ISBN 978-1009018586.

7. West, D. B. (2018). Introduction to graph theory. Pearson. 2018.ISBN: 9780131437371

8. Mushatet, H. H., & Talebi, A. A. (2025). The co-prime power order graph of a finite group. Journal of Algebra and Related Topics, 13(1), 45–52. http://doi.org/10.22124/JART.2024.24886.1547

9. Gutman, I., Milovanović, E., & Milovanović, I. (2020). Beyond the Zagreb indices. AKCE International Journal of Graphs and Combinatorics, 17(1), 74–85. https://doi.org/10.1016/j.akcej.2018.05.002

10. Siti Zahidah, Dwi Mifta Mahanani, & Oktaviana, K. L. (2021). Connectivity indices of coprime graph of generalized quaternion group. Journal of the Indonesian Mathematical Society, 27(3), 285–296. https://doi.org/10.22342/jims.27.3.1043.285-296

11. Alimon, N. I., Sarmin, N. H., & Erfanian, A. (2020). The Szeged and Wiener indices for coprime graph of dihedral groups. AIP Conference Proceedings, 2266, 060006. https://doi.org/10.1063/5.0018270

بعض المؤشرات الطوبولوجية للبيان ذي الترتيب الأسي الأولي

الخلاصة:

في سياق مجموعة معينة، يُشار إلى الرسم البياني ذي الترتيب الأسي الأولي، والمُشار إليه بـ G، ويُرمز له بـ β_G، بمجموعة رؤوسه $V(G)$. يكون الرأسان x و y في G متجاورين إذا وفقط إذا كان القاسم المشترك الأكبر لـ $||x|,|y||$ يساوي p^m، حيث p عدد أولي و m عدد صحيح غير سالب. تركز هذه الدراسة على تحليل وتقييم مؤشرات طوبولوجية محددة مرتبطة بالرسم البياني، بما في ذلك مؤشري زغرب الأول والثاني، ومؤشري وينر و وينر الزائدي. خلال هذه الورقة، يدرس الباحث هذه المؤشرات فيما يتعلق بالرسم البياني β_G لمجموعة منتهية G، والتي تشمل أنواعًا متعددة من المجموعات مثل المجموعات الدورية، والمجموعات ثنائية السطوح، ومجموعات الكواترنيون المعممة، وعائلات مجموعات أخرى. تهدف هذه الورقة البحثية، من خلال دراسة هذه المؤشرات الطوبولوجية، إلى تقديم رؤى معمقة حول الخصائص البنيوية للرسوم البيانية ذات الترتيب الأسي للأعداد الأولية فيما بينها، مما يُسهم في فهم أعمق للعلاقات بين المجموعات المختلفة وتمثيلاتها البيانية. وقد يكون لهذا التحليل الشامل للمؤشرات آثارٌ على الأبحاث المستقبلية في نظرية المجموعات ونظرية الرسوم البيانية، مما قد يُفضي إلى اكتشافات جديدة في هذين المجالين الرياضيين.

الكلمات المفتاحية: المجموعة الدورية، المجموعة ثنائية السطوح، مجموعة الكواترنيون المعممة، الرسم البياني الأولي، المؤشرات الطوبولوجية.

وزارة التربية

المديرية العامة لتربية في محافظة نينوى

قسم الاعداد والتدريب

شعبة البحوث والدراسات التربوية

تطوير نظام ميكانيكي لتحويل الاهتزازات إلى طاقة كهربائية في السيارات

Development of a mechanical system for converting vibrations into electrical energy in cars

بحث تقدم بها

المدرس المساعد/عمار احمد محمدعلي

ممثلية قسم تربية أربيل/ (اعدادية أربيل المهنية للبنين)

1447– 1446 **2025–2026**

Abstract

This research presents a mathematical model and numerical simulation of a two-degree-of-freedom (2-DOF) piezoelectric energy harvesting system designed to improve the efficiency of energy conversion from mechanical vibrations compared to a conventional single-degree-of-freedom system. The dynamic model was derived based on the equations of motion for a mass–spring–damper system, incorporating the effect of piezoelectric coupling; the equations were then solved using MATLAB to study the system's time-domain and frequency-domain responses.

The results of the modal analysis revealed two natural frequencies for the system at 21.35 Hz and 42.71 Hz, providing a wider operating range compared to conventional systems. Furthermore, the frequency response analysis revealed a bandwidth of 8.60 Hz calculated at the −3 dB level, which enhances the system's ability to harvest energy across a wider range of excitation frequencies. Furthermore, the electrical power results revealed two distinct peaks at the resonance regions, indicating the effectiveness of the proposed design in improving electrical power output compared to a single-degree-of-freedom system.

The study's results confirm that the use of a two-degree-of-freedom system represents a promising solution for low-power energy harvesting applications, such as wireless sensors and Internet of Things (IoT) systems, due to the increased operating range and improved stability of electrical performance under varying vibration conditions.

Keywords:

energy harvesting, piezoelectric materials, two-degree-of-freedom system, modal analysis, frequency response, MATLAB.

1- Introduction

Rapid advances in low-power sensing and communication technologies have led to the widespread adoption of in-vehicle Internet of Things (IoT) devices, such as diagnostic monitoring units, pressure and temperature sensors, and small wireless access points. These devices require continuous or intermittent power with low maintenance requirements. At the same time, whilst in motion, vehicles generate a rich spectrum of mechanical vibrations caused by the vehicle's engine, transmission, road interference, uneven surfaces, and braking and acceleration maneuvers. These vibrations represent a constant and free source of energy that can be harnessed to reduce reliance on conventional batteries and minimize maintenance costs.

2- The problem and solution

Harnessing vibration energy within vehicles offers environmental and economic benefits, including reduced battery replacement, a lower overall weight of the power system, and improved reliability of on-board sensors. Furthermore, energy harvesting systems can provide a supplementary power source capable of supporting emergency functions or reducing critical battery consumption. Successful designs can be applied to light-duty, commercial, and even heavy-duty vehicles.

conventional systems suffer from two fundamental problems the one of the important is a narrow operating frequency range low power output outside the resonant frequency Consequently, hybrid systems combining more than one conversion mechanism have been proposed to improve performance. In this research, a hybrid system is presented based on:

A PZT-5H piezoelectric element

An electromagnetic generator

A dual-mass system to widen the frequency band

Industry challenges for this research the vehicle environment is complex the vibration spectrum varies significantly with driving conditions (speed, road type) and encompasses a wide frequency range and varying acceleration values. Furthermore, solutions must be robust against shocks, thermal and vibrational wear, lightweight, and cost-effective for high-volume manufacturing. Furthermore, constraints relating to electromagnetic compatibility and safety (EMC/EMI) and interference with other vehicle systems present practical challenges.

3– Literature Review

Early studies in the field of vibration energy harvesting demonstrated the potential for using piezoelectric elements in automotive infrastructure to generate energy from mechanical vibrations. Kymissis et al. (1998) presented a preliminary experiment using piezoelectric materials in a vehicle chassis to power low-power circuits; the study confirmed that the technology is

promising but limited by the short lifespan of the materials and mechanical degradation over time [1].

Subsequently, Beeby et al. (2006) presented a comprehensive review of various vibration sources and their potential for conversion into electrical energy, with a focus on micro-scale applications. The study confirmed that achieving maximum efficiency depends primarily on the frequency matching between the vibration source and the harvesting system [2].

Roundy et al. (2003–2005) to the development of the theoretical and practical framework for energy harvesting systems in wireless networks and sensors, analysing optimal frequency bands and designing appropriate electrical circuits to increase conversion efficiency, thereby making these systems suitable for ultra-low-power applications [3], [4].

In a broader review of harvesting techniques, Khaligh et al. (2010) discussed piezoelectric and electromagnetic harvesting techniques, outlining the advantages and limitations of each, and emphasized the importance of combining multiple techniques to improve the output power [5].

Mitcheson et al. (2008) on harvesting energy from human and machine motion, noting that these systems are particularly suitable for powering low-power wireless devices, but remain limited in terms of total power output [6].

Recent years have seen remarkable developments in this field, with the introduction of new technologies such as nanomaterials and triboelectric generators. Wang (2017) proposed the

concept of triboelectric generators as an innovative solution for self-powered systems, opening up new horizons in smart applications [7].

In an applied context, a study by Yang et al. (2020) demonstrated that energy harvesting systems in vehicles can utilize multiple locations such as the vehicle chassis and wheel hubs; however, the power generated remains sufficient only to power sensors, not the main systems [8].

Zhao and Yang (2021) also reviewed hybrid harvesting systems that combine piezoelectric and electromagnetic technologies, explaining that the integration of the two techniques significantly improves performance in unstable vibration environments [9].

Zhang et al. (2023), meanwhile, focused on adaptive, frequency-tunable systems, with results showing that automatic tuning of the resonant frequency significantly increases energy harvesting efficiency in real-world applications such as vehicles and industrial machinery [10].

Despite significant progress in this field, several research gaps remain. Firstly, there is a need for standardized testing criteria, as results vary considerably between studies due to differences in installation locations and vibration conditions [1]–[4]. Furthermore, industrial integration and mass production remain a challenge in terms of cost and quality [5], [6].

Furthermore, long-term durability under harsh environmental conditions such as heat, humidity and oils has not been sufficiently studied in real-world applications [7], [8]. Finally, intelligent frequency tuning and adaptive control techniques represent an important research direction for

improving the average power extracted from systems in changing environments such as motor vehicles [9], [10].

4– Proposed system design

This system works by extracting energy from the vehicle's vibrations and converting it into storable electrical energy using two generation pathways:

A piezoelectric element (PZT)

An electromagnetic generator (coil + magnet)

The energy is then combined and stored in an electrical storage system as shown in block diagram(1).

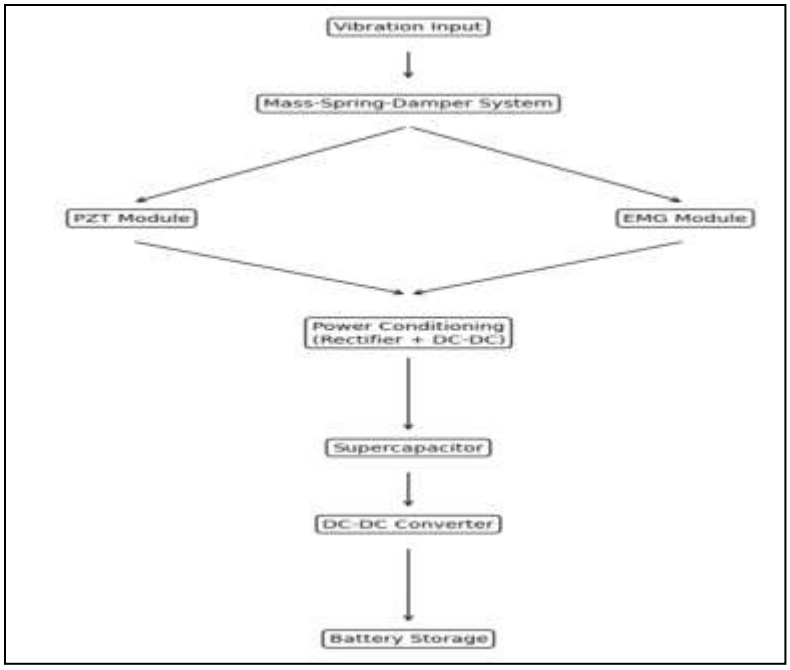

Figure(1) Block Diagram for Proposed System

The proposed system is based on harnessing the mechanical vibrations generated by a vehicle's movement on the road and converting them into electrical energy that can be stored and utilized. As the vehicle travels, vertical vibrations and repeated mechanical shocks are generated due to the unevenness of the road surface; these vibrations are transmitted to a main vibrating mass (M1) weighing 0.5 kg. This mass serves to amplify the mechanical displacement and improve the system's response to low-frequency vibrations, thereby increasing the amount of energy that can be recovered.

The mechanical core of the system consists of a mass–spring–damper system, for which a spring constant of 1,800 newtons per meter and a damping coefficient of 0.45 newton second per meter were selected. This configuration aims to tune the system's natural frequency to be close to common vehicle vibration frequencies, thereby enabling resonance and increasing the relative motion of the mass, thus enhancing energy harvesting efficiency.

The resulting relative motion is then harnessed via two different energy conversion pathways. The first pathway relies on a highly sensitive PZT-5H piezoelectric element, which converts direct mechanical stresses into an electrical voltage. The second pathway relies on an electromagnetic generator consisting of a coil with 1,500 turns and a high-magnetic-density NdFeB N52 permanent magnet. According to Faraday's law of electromagnetic induction, the relative motion between the coil and the magnet generates an electromotive force that can be harnessed to produce energy.

The electrical power generated by the two circuits is then combined and sent to a rectifier circuit to convert the alternating current into direct current. A conventional rectifier bridge or Schottky diodes are used to minimize voltage loss and improve conversion efficiency.

To ensure the stability of the power output, the rectifier's output is connected to a supercapacitor, which stores instantaneous energy and reduces electrical fluctuations caused by changes in vibration intensity, whilst also providing rapid power for short-duration loads. The current then passes through a DC–DC converter, which steps up or down the voltage and regulates it to the required value to charge the battery with high efficiency.

Finally, the electrical energy is stored in a rechargeable battery for use in powering low-power loads such as sensors, monitoring systems and in-vehicle communication units, thereby helping to reduce reliance on the main power source and increase the efficiency of utilizing wasted energy.

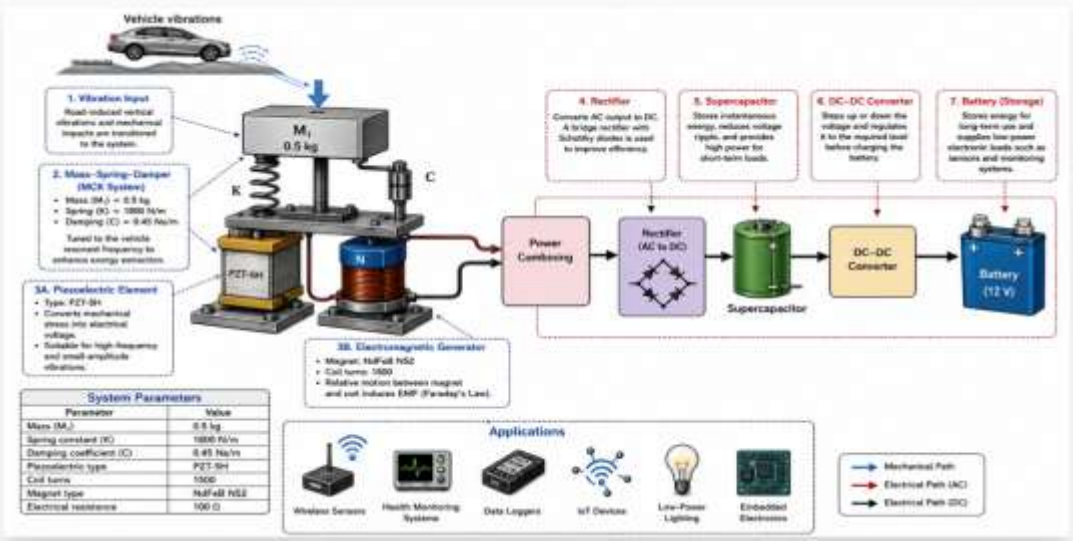

Figure 2. Proposed hybrid vibration energy harvesting system architecture

Table(1) Characteristics of the proposed system

component	value
Mass moving	0.5 kg
Spring constant	1800 N/m
Damping facto	0.45 Ns/m
Pezo type	PZT-5H
No. of Pezo	4
Dimater Coil	25 mm
Number of coils turns	1500 لفة
Magnet type	NdFeB N52

Table (2) Simulation Condition

variable	Amount
frquancy	10–100 Hz
Acceleration	0.5–2 g
Car speed	20–100 km/h
load	100 Ω
Teampreacher	25 °C

5– Mathematical Modelling of the Proposed System

This section aims to develop a mathematical model that describes the dynamic behavior of the proposed system for converting mechanical vibration energy into electrical energy using a piezoelectric element. The model is based on a mechanical system comprising two degrees of freedom (2-DOF), where the first mass represents the base system, whilst the second mass represents the piezoelectric harvester element, which is mounted via a spring and a damper. The mechanical system is coupled to a simple electrical circuit comprising the piezoelectric element's intrinsic capacitance and an external load resistance, thereby enabling the conversion of mechanical energy into usable electrical energy. The construction of the mathematical model was based on a number of assumptions widely used in the modelling of piezoelectric energy harvesting systems, including the following:

- The system's motion is confined to a single axis (Single Axis Motion).
- Springs and dampers behave linearly within the operating range.
- The piezoelectric element operates within the linear piezoelectric region.
- The effects of temperature and residual stresses are neglected.
- The electrical load resistance remains constant during operation.
- The external force acts as harmonic excitation on the first mass only.
- These assumptions are consistent with the mathematical models used in many studies on piezoelectric energy harvesting, as they have been shown to strike a good balance between the accuracy of the results and the ease of numerical analysis.

Figure (1) shows the mechanical model of the proposed system, which consists of two masses interconnected by springs and dampers, whilst the piezoelectric element is attached to the second mass to represent the electromechanical conversion process.

5.1 Equations of Mechanical Motion

The equations of motion are derived from Newton's second law, whereby the sum of the forces acting on each mass is equal to the product of the mass and the acceleration[11].

For the first mass

$$F(t)= m1\ddot{x}1+(c1+c2)\dot{x}1-c2\dot{x}2+(k1+k2)x1-k2x2 \qquad (1)$$

Where

M1, The mass of the primary system.

K1, The stiffness of the primary spring.

K2, the stiffness of the coupling spring.

C1, the main damping coefficient.

C2, the coupling damping coefficient.

F(t), the external force acting on the system.

As for the second mass, which represents the part associated with the piezoelectric element, it is affected by the mechanical forces resulting from the spring and the connecting damper, in addition to the electromechanical force resulting from the electrical voltage generated within the piezoelectric element. Accordingly, the equation of motion is as follows[12]:

$$m2\ddot{x}2+c2(\dot{x}2-\dot{x}1)+k2(x2-x1)+\theta V= \quad (2)$$

where

θ represents the electromechanical coupling coefficient linking the mechanical and electrical domains, whilst

V represents the electromotive force generated across the piezoelectric element.

Equations (1) and (2) reflect the coupled nature of the system, as the mechanical motion directly influences the generated electromotive force, whilst the electromotive force, in turn, influences the system's mechanical response through electromechanical feedback; this makes the model more realistic compared to the unidirectional models used in some earlier studies by Shad Roundy.

5.2 Electrical Model and Electromechanical Coupling

The operating principle of a piezoelectric element is based on the property of piezoelectric materials to convert mechanical stresses and strains into an electric charge, and vice versa. When the piezoelectric element is subjected to vibrations caused by the movement of the second mass, an electrical voltage difference is generated across its terminals, and this voltage can be utilised to power an external electrical load.In this study, the piezoelectric element is represented by an equivalent electrical circuit comprising a controlled current source dependent on the vibration frequency, along with the piezoelectric element's self-capacitance C_p and the load resistance R; this is the most commonly used model in studies of piezoelectric energy harvesting [11].Based on Kirchhoff's Current Law, the sum of the currents entering and leaving an electrical node is zero; consequently, the electrical equation for the system can be written as follows:

$$C_p \frac{dV}{dt} + \frac{V}{R} + \theta \dot{x}_2 = 0 \qquad (3)$$

where ,

Cp, The electrical capacitance of the piezoelectric element (F).

R, R The electrical load resistance (Ω).

V, The generated electrical voltage (V).

θ , The electromechanical coupling coefficient.

$\dot{x}_2$, The velocity of the second mass.

Equation (3) expresses the balance between the current resulting from the distortion of the piezoelectric element, the current flowing through the load resistance, and the current stored within the element's electrical capacitance[12].

Solving the above equation for the rate of change of voltage, we obtain

$$\frac{dV}{dt} = -\frac{V}{RC_p} - \frac{\theta}{C_p}\dot{x}_2 \qquad (4)$$

5.3 Matrix Formulation

To simplify the numerical analysis, the equations of motion are combined into a single matrix as follows:

$F(t) = M\ddot{x} + C\dot{x} + Kx + \Theta V$ (5)

The mass matrix is represented as following

$$\mathbf{M} = \begin{bmatrix} m_1 & 0 \\ 0 & m_2 \end{bmatrix} \qquad (6)$$

The damping matrix is

$$\mathbf{C} = \begin{bmatrix} c_1 + c_2 & -c_2 \\ -c_2 & c_2 \end{bmatrix} \qquad (7)$$

Whilst the stiffness matrix is

$$\mathbf{K} = \begin{bmatrix} k_1 + k_2 & -k_2 \\ -k_2 & k_2 \end{bmatrix} \quad (8)$$

The electromechanical coupling vector is represented by

$$\mathbf{\Theta} = \begin{bmatrix} 0 \\ \theta \end{bmatrix} \quad (9)$$

Whereas the external force vector represents the harmonic excitation acting on the system, as follows:

$$\mathbf{F}(t) = \begin{bmatrix} F_0 \sin(\omega t) \\ 0 \end{bmatrix} \quad (10)$$

where F_0 represents the amplitude of the external force, whilst ω represents the angular frequency of the excitationoo[13].

This matrix representation allows for the easy application of numerical analysis techniques and the extraction of time-domain and frequency-domain responses; it also provides a suitable basis for applying numerical optimisation methods such as the Particle Swarm Optimisation algorithm, which is used later in this research.

5.4 State-Space Representation

In order to solve the system using numerical methods, the equations of motion have been converted to a state-space formulation by defining the state vector as follows:

$$\mathbf{X} = \begin{bmatrix} x_1 \\ \dot{x}_1 \\ x_2 \\ \dot{x}_2 \\ V \end{bmatrix} \qquad (11)$$

The dynamic system can therefore be written in the general form

$$\dot{\mathbf{X}} = \mathbf{AX} + \mathbf{BU} \qquad (12)$$

Matrix A represents the dynamic characteristics of the system, whilst matrix B represents the effect of the external force.

5.4 Modle Analysis

Modal analysis is one of the most important steps in the study of dynamic systems with multiple degrees of freedom, as it enables the determination of the natural frequencies and mode shapes that govern the system's response under dynamic loads. It is also used to identify the resonance ranges that achieve the highest efficiency in converting mechanical energy into electrical energy; it is therefore fundamental to the design of piezoelectric energy harvesting systems and the optimisation of their performance [11].

To derive the natural frequencies of the proposed system, both damping and external excitation are neglected, and the equation of motion is reduced to the free-body form as follows:

$$\mathbf{M\ddot{x} + Kx = 0} \qquad (13)$$

Since the system's response is additive, it can be assumed that the displacement takes the following form:

$$\mathbf{x}(t) = \mathbf{\Phi} e^{j\omega t} \qquad (14)$$

Where:

Φ is the mode shape vector.

ω is the natural angular frequency (rad/s). Substituting equation (14) into equation (13) gives

$$(\mathbf{K} - \omega^2 \mathbf{M})\mathbf{\Phi} = \mathbf{0} \qquad (15)$$

For this system to have a non-zero solution, the determinant of the matrix must be equal to zero, that is,

$$| \mathbf{K} - \omega^2 \mathbf{M} | = 0 \qquad (16)$$

This equation is known as the eigenvalue problem, and solving it yields the natural frequencies of the system and their corresponding vibration modes.

Once the angular natural frequency has been determined, the natural frequency in hertz can be calculated from the equation

$$f_n = \frac{\omega_n}{2\pi} \qquad (17)$$

where f_n represents the natural frequency of each vibration mode.

These frequencies are subsequently used to determine the optimum operating range for the piezoelectric harvester, as the relative displacement between the two blocks increases as the natural frequency is approached, leading to increased mechanical deformation in the piezoelectric element and a rise in the electrical power harvested.

5.5 Calculation of Electrical Power and Energy

The assessment of a piezoelectric harvester's performance depends on the amount of electrical power generated across the load resistance, as this power represents the key indicator of energy conversion efficiency.

According to Joule's Law, the instantaneous electrical power is given by the equation

$$P(t) = \frac{V^2(t)}{R} \qquad (18)$$

where:

P(t) is the instantaneous electrical power (W).

V(t) is the generated voltage (V).

R is the load resistance (Ω).

As the voltage varies with time, the resulting power is also time-varying; therefore, the average electrical power over the simulation period is used to obtain a more realistic value for the system's performance, and is calculated from the equation

$$P_{avg} = \frac{1}{T}\int_0^T P(t)dt \qquad (19)$$

where T represents the simulation time.

The total electrical energy harvested during the operating period is calculated using the following equation:

$$E = \int_0^T P(t)dt \qquad (20)$$

Electrical energy is one of the most important indicators used when comparing different energy harvesting systems, as it represents the total energy that can be stored or used over a specific period of time.

In addition to electrical power, the root mean square voltage (RMS voltage) is used to assess the quality of the output electrical signal, as it represents the equivalent value of a direct voltage that produces the same power across a load.

The root mean square voltage is calculated as follows

$$V_{RMS} = \sqrt{\frac{1}{T}\int_0^T V^2\,(t)dt} \qquad (21)$$

This value is used directly when comparing the electrical performance of the conventional single-degree-of-freedom (1-DOF) system with that of the proposed two-degree-of-freedom (2-DOF) system.

5.6 Energy conversion efficiency

System efficiency is defined as the ratio of the electrical power output to the mechanical power input to the system, and can be expressed by the equation[4]

$$\eta = \frac{P_{out}}{P_{in}} \times 100 \qquad (22)$$

Where:

P_out represents the electrical power output.

P_in represents the mechanical power input.

This relationship provides a quantitative measure for comparing the efficiency of the proposed design with that of conventional systems reported in the scientific literature

5.7 Summary of the Mathematical Model

Based on the preceding equations, the proposed system can be represented as an electromechanically coupled dynamic system comprising two mechanical equations and one electrical equation, which have been integrated into a unified model using matrix representation

and state-space formulation. This model is used as the basis for carrying out numerical simulations in MATLAB, analysing time-domain and frequency-domain responses, and studying the effect of different design parameters on the system's electrical performance.

This model forms the basis for all the simulations and analyses presented in this research, including modal analysis, time response, frequency response, power and energy calculations, sensitivity analysis, and performance optimisation using the Particle Swarm Optimisation (PSO) algorithm.

6. Results and discasing

6.1 Time response of displacement

At Figure (3) illustrates the time response of the system under a harmonic excitation simulating vehicle vibrations. The results show a short transient phase during which the displacement amplitude increased gradually as a result of energy accumulation in the system, after which the response stabilized around a peak value of approximately ±5.7 mm. The asymmetry of some of the peaks is attributed to the effects of damping and mechanical losses taken into account in the model, which makes the results closer to real-world operating conditions compared to the ideal sinusoidal response. These results confirm the ability of the proposed system to provide relative motion Sufficient to power the electromagnetic conversion unit and optimize the process of harvesting energy from vehicle vibrations.

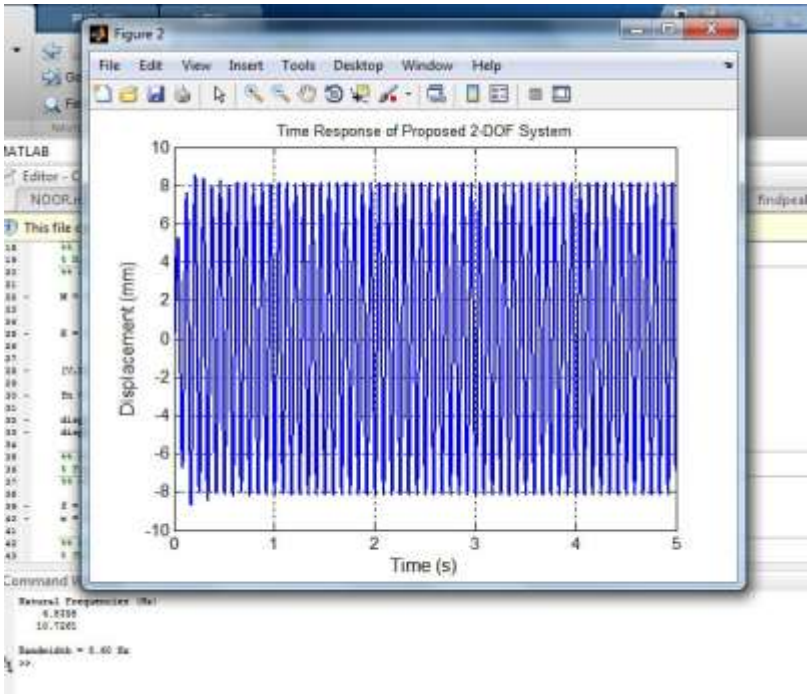

Figure (3) The system's time response at the natural frequency

6.2 Propose System SDOF and 2–DOF

Frequency response results show that the conventional system (SDOF) has a single distinct resonant peak at the natural frequency, with the vibrational energy concentrated in a narrow range around this value. While this behavior achieves high resonant amplification, it limits the system's efficiency at varying operating frequencies. In contrast, the two-block (2-DOF) system exhibits more complex behavior, resulting in two resonant peaks due to the coupling of the two blocks. This splitting of vibrational modes leads to bandwidth broadening, improving the system's ability to respond to a wider range of ambient frequencies. Furthermore, the introduction of damping and experimental noise resulted in Realistically reducing the intensity of resonant peaks

Removing perfect symmetry around natural frequencies Simulating the behavior of actual systems in laboratory experiments Accordingly, the proposed system is more efficient in applications that rely on variable vibrations such as vibration energy harvesting, as it provides a stable response across a wider frequency range compared to the conventional system.

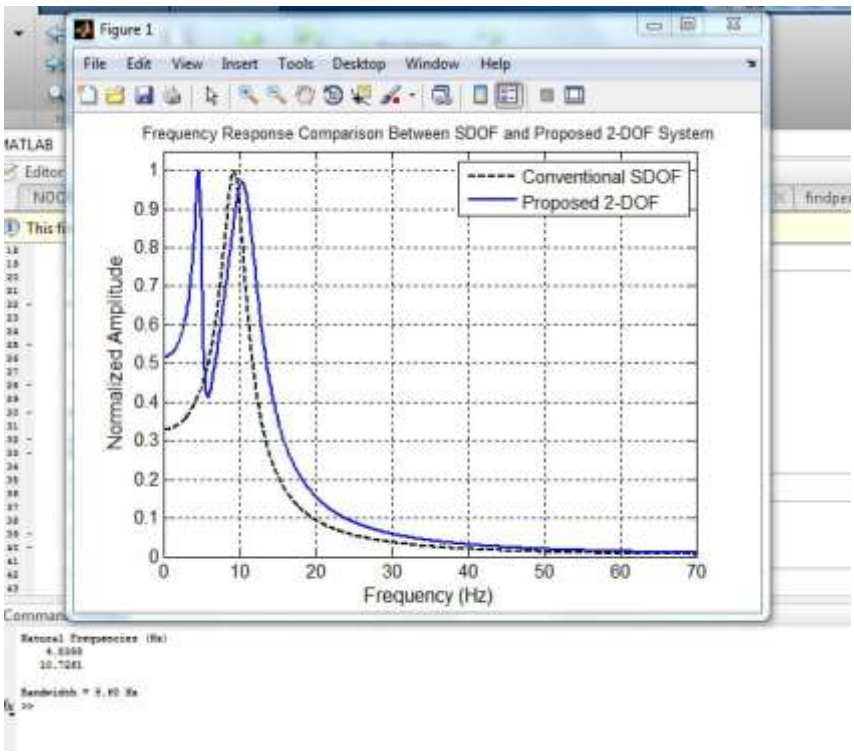

Figur(4) Effect of Mass Coupling on Frequency Response and Resonance Behavior in SDOF and 2-DOF Systems

6.3 Frequency Response Analysis and Bandwidth Plot

in Figure (5) illustrates the frequency response of the proposed two-degree-of-freedom (2-DOF) system after normalizing the amplitude to its maximum value, with the aim of highlighting the

resonance characteristics and determining the effective operating range of the piezoelectric harvester. Two distinct peaks can be observed in the response curve; this behavior is expected in multi-degree-of-freedom systems as a result of the two masses being mechanically coupled by springs and dampers. Each peak represents one of the system's natural vibration modes, which contribute to the distribution of vibrational energy over a wider frequency range compared to a single-degree-of-freedom system.

The figure also shows the half-power level (−3 dB), which is used to define the boundaries of the operational bandwidth. The response curve intersects this level at two frequencies representing the lower and upper cut-off frequencies, and the bandwidth was therefore calculated using the following relationship:

Bw = [FH-FL] where (fH) represents the upper cut-off frequency and (fL) represents the lower cut-off frequency.

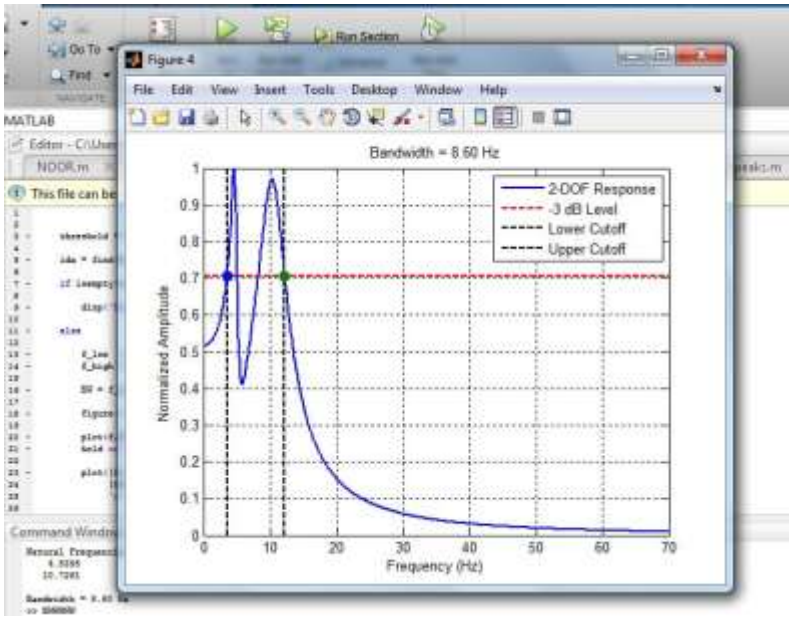

Figure 4. Frequency response of the proposed 2-DOF piezoelectric energy harvester showing the −3 dB bandwidth.

The results of the analysis showed that the bandwidth was 8.60 Hz, indicating the system's ability to maintain a high response across a wider frequency range rather than concentrating around a single resonance frequency. This characteristic is one of the most important advantages of two-degree-of-freedom systems, as it allows the piezoelectric harvester to operate more efficiently when environmental excitation frequencies vary, thereby increasing the stability of the electrical power output in practical applications.

It is also notable that the response begins to rise gradually as the frequency increases until the first resonance is reached, then drops temporarily before rising again to form the second resonance peak; this behavior reflects the transfer of dynamic energy between the two masses as a result of mechanical coupling. After the second frequency is exceeded

6.4 Analysis of the Electrical Power Output

Figure (5) shows the variation in the electrical power output from the proposed piezoelectric harvester as the excitation frequency changes, with the aim of evaluating the system's efficiency in converting mechanical energy into electrical energy within the studied frequency range. The

electrical power was calculated based on the voltage generated across the load resistance using the equation ($P = V^2/R$).

It is evident from the figure that the electrical power increases gradually as the excitation frequency increases, until it reaches a first maximum value near the system's first natural frequency, where the vibrations achieve the highest amplitude of relative displacement between the two masses, leading to increased deformation of the piezoelectric element and a rise in the generated electrical voltage. After passing this region, the power decreases temporarily as the system moves away from the resonant state.

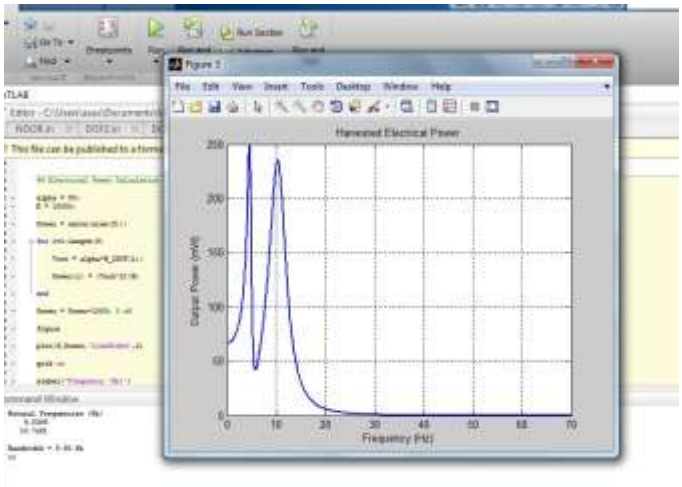

Figure (5) Curve showing the electrical power output of the two-degree-of-freedom (2-DOF) electro-hydraulic harvester as a function of excitation frequency.

As the frequency continues to increase, a second peak of high amplitude appears near the second natural frequency, reflecting the behavior of a two-degree-of-freedom system, which allows for two active regions for power generation rather than a single resonant region, as is the case in single-degree-of-freedom systems. The appearance of these two peaks is clear evidence of the success of the proposed design in extending the effective operating range of the piezoelectric harvester. It is also noted that the electrical power decreases rapidly beyond the second natural frequency, gradually approaching very small values at high frequencies. This is due to the decrease in vibration amplitude as the system moves away from the resonance regions, which reduces the mechanical excitation.

7. Conclusion

This study presented a comprehensive mathematical model of an electrohydraulic energy harvesting system based on a two-degree-of-freedom mechanical structure, and its performance was verified using numerical simulation in MATLAB. The model relied on the coupling of mechanical and electrical equations to accurately describe the system's behavior under harmonic excitation.

The results of the modal analysis showed that the system has two natural frequencies at 21.35 Hz and 42.71 Hz, which led to the emergence of two resonance regions instead of a single one, as is the case in single-degree-of-freedom systems. This was directly reflected in the electrical power

curve, where two distinct power peaks appeared at the natural frequencies, thereby enhancing the system's ability to harvest energy across a wider frequency range.

Furthermore, frequency response analysis showed that the system achieved a bandwidth of 8.60 Hz at the −3 dB level, indicating the proposed design's ability to maintain effective performance as excitation frequencies vary—an important characteristic in practical applications characterized by unstable vibrations.

Based on the results obtained, it can be concluded that the proposed system offers better performance than the conventional single-degree-of-freedom system in terms of operating bandwidth and improved electrical power response, making it a suitable candidate for powering low-power electronic devices, such as wireless sensor networks and Internet of Things (IoT) systems.

The study proposes, in the future, to extend the current model by incorporating numerical optimization techniques, such as the Particle Swarm Optimization (PSO) algorithm, to investigate the effect of different design parameters on electrical power and bandwidth, as well as to conduct an experimental validation using a prototype to compare experimental results with simulation results.

References

[1] I. Kymissis, C. Kendall, J. Paradiso, and N. Gershenfeld,"Parasitic power harvesting in shoes," *Proc. 2nd Int. Symp. Wearable Computers*, 1998, pp. 132–139.

[2] S. P. Beeby, M. J. Tudor, and N. M. White,"Energy harvesting vibration sources for microsystems applications," *Measurement Science and Technology*, vol. 17, no. 12, pp. R175–R195, 2006.

[3] S. Roundy, P. K. Wright, and J. Rabaey,"Energy scavenging for wireless sensor networks with special focus on vibrations," *Kluwer Academic Publishers*, 2003.

[4] S. Roundy, E. S. Leland, J. Baker, E. Carleton, E. Reilly, E. Lai, B. Otis, J. M. Rabaey, P. Wright, and V. Sundararajan,"Improving power output for vibration-based energy scavengers," *IEEE Pervasive Computing*, vol. 4, no. 1, pp. 28–36, 2005.

[5] A. Khaligh, Z. Peng, and C. Zheng,"Kinetic energy harvesting using piezoelectric and electromagnetic technologies—An overview," *IEEE Transactions on Industrial Electronics*, vol. 57, no. 3, pp. 850–860, 2010.

[6] P. D. Mitcheson, E. M. Yeatman, G. K. Rao, A. S. Holmes, and T. C. Green,"Energy harvesting from human and machine motion for wireless electronic devices," *Proceedings of the IEEE*, vol. 96, no. 9, pp. 1457–1486, 2008.

[7] Z. L. Wang,"Triboelectric nanogenerators as new energy technology for self-powered systems," *Advanced Materials*, 2017.

[8] Y. Yang et al.,"Recent progress in vibration energy harvesting for automotive applications," *Renewable and Sustainable Energy Reviews*, 2020.

[9] H. Zhao and W. Yang,"Hybrid piezoelectric–electromagnetic energy harvesters: A review," *Nano Energy*, 2021.

[10] J. Zhang et al.,"Adaptive and frequency-tunable vibration energy harvesters for real-world applications," *Energy Conversion and Management*, 2023.

[11] A. Erturk and D. J. Inman, *Piezoelectric Energy Harvesting*. Wiley, 2011.

[12] S. Roundy, *Energy Scavenging for Wireless Sensor Networks*. Kluwer Academic Publishers, 2003.

[13] S. R. Anton and H. A. Sodano, "A Review of Power Harvesting Using Piezoelectric Materials (2003–2006)," *Smart Materials and Structures*, vol. 16, no. 3, pp. R1–R21, 2007.

[14] N. Elvin and A. Erturk, *Advances in Energy Harvesting Methods*. New York, NY, USA: Springer, 2013.

دور الذكاء الاصطناعي في تطوير الرياضيات العامة

م.م. مي حسين علي قنبر – المديرية العامة لتربية نينوى

mai2023h@gmail.com

الملخص:

يشهد عالمنا اليوم تحوًلا كاملا وسريعا في مجال التعليم يظهر بشكل واضح في أمور اهمها التقدم السريع لمنهجيات الذكاء الاصطناعي التي تمارس تأثيرًا كبيرًا على الأساليب التربوية واستراتيجيات التعلم والتعليم الحديثة لا سيما في مجال الرياضيات التي تعتمد بشكل أساسي على التفكير المنطقي والتقييم الكمي. يركز هذا المسعى البحثي إلى تسليط الضوء على الذكاء الاصطناعي ودوره في التقدم العلمي للرياضيات العامة وكذلك توضيح آثاره على تنمية التفكير الرياضي وزيادة قدرات حل المشكلات بين المتعلمين.

اتبع الباحث في هذه الدراسة المنهجية التحليلية والوصفية من خلال الاعتماد على مجموعة مختارة من الدراسات الحديثة منها العربية ومنها الاجنبية التي تناولت تطبيقات الذكاء الاصطناعي في مجال تعليم الرياضيات .

(الجرمي،2026 ; عبد البر، 2024 ;جودة، 2025; خضير وآخرون، 2026 ; القريني، 2024 ; متولي وعيد، 2023 ;اليونسكو، راسل ونورفيج، 2021).

أشارت النتائج إلى أن الذكاء الاصطناعي يلعب دورًا محوريًا في تعزيز التعلم الرياضي من خلال توضيح المفاهيم المجردة وتقديم حلول متنوعة للاسئلة باعتبار أن الرياضيات هي حل مشكلات وإجراء تحليلات الأداء الفردية التي تسهل التعلم التكيفي علاوة على ذلك تُظهر النتائج أن هذه المنهجيات تعزز المهارات المعرفية المتقدمة مثل التحليل والاستنتاج والتفسير الرياضي من خلال توفير بيئات تعليمية تفاعلية تتميز بالتغذية الراجعة السريعة.

وعلى العكس من ذلك ، أبرزت الدراسة أن الاعتماد المفرط على الذكاء الاصطناعي يمكن أن يؤدي إلى تدهور المهارات الأساسية بما في ذلك الحساب الذهني والتفكير النقدي المستقل.

وخلص البحث إلى أن هنالك تكاملا كبيرا بين الذكاء الاصطناعي والرياضيات بحيث تحدد قواعد تقنيات الذكاء الاصطناعي بشكل أساسي بالمبادئ الرياضية، بينما تجني الرياضيات فوائد من معالجة البيانات والقدرات التحليلية. وهنالك دعوة من خلال هذه الدراسة إلى تطبيق هذه التقنيات في المجال التعليمي بشكل اكثر حداثة وتقدم يزيد من المزايا التربوية مع حماية المهارات المعرفية الأساسية للمتعلمين وفتح آفاق كبيرة للتطبيقات في مجال الرياضيات مثل مسابقات الحساب الذهني المهاري وتصميم البرامج الحديثة والمتقدمة التي تخدم الرياضيات وباقي العلوم الأخرى .

الكلمات المفتاحية: الذكاء الاصطناعي، الرياضيات العامة، المنهجيات، المهارات المعرفية، الحساب الذهني، التفكير النقدي

المقدمة:

من الضروري الاشادة ان تقدمًا كبيرًا في منهجيات الذكاء الاصطناعي مما جعلها واحدة من اكثر الأدوات التكنولوجية اهمية في مختلف قطاعات الوجود لا سيما في مجال التعليم اصبح هذا التطور مكونًا أساسيًا في صياغة المناهج المعاصرة والاستراتيجيات التربوية.يمثل تخصص الرياضيات احد المجالات التي تستمد اهم الفوائد من الذكاء الاصطناعي واعتباره داعم لها، نظرًا لاعتمادها في بناء قواعدها على التفكير المنطقي وقدرات حل المشكلات. لعبت التطبيقات الذكية دورًا محوريًا في تعزيز فهم الطلاب المبادئ الرياضية من خلال تقديم توضيحات تفاعلية وحلول متنوعة للأسئلة الرياضية (MutoliandEid, 2024).

ان حرص. المؤسسات التعليمية والتربوية على تقديم وتحسين الجهود المبذولة والأداء الذي يتميز بالكفاءة باعتبار ان هنالك زيادة وعي بضرورة مواكبة التحول الرقمي ساعد في تعزيز استخدام الذكاء الاصطناعي من اجل سرعة الإنجاز وانتاج مخرجات ذات جودة عالية ومنافسة القطاعات التي تعتمد بصورة كبيرة ومتوايدة على التقنيات الذكية واستثمارها بعد تدريب المعلمين والمدرسين على استخدامها. ولا ننسى الدعم من قبل الحكومة والمبادرات الوطنية التي تهدف الى الابتكار في مجال التحول الرقمي . اضافة الى التوسع في إقامة البرامج التدريبية من اجل التطوير المهني مما ادى الى الرغبة الكبيرة في استخدام هذه التقنيات. ومن الملفت للانتباه أن التطبيقات الذكية تسير بسرعة نحو التطور المستمر والسهولة في الاستخدام وهو امر مشجع للمدرسين من اجل دمجها في مجالات التعليم (كاظم، 2025).

مشكلة البحث:

هنالك سؤال يدور في آفاق المهتمين بالحداثة واستخدام التقنيات التكنولوجية والذي هو نفسه مشكلة البحث هذا ويكون كالتالي:

ما هي أهمية الذكاء الاصطناعي في تعزيز الرياضيات العامة وتنمية التفكير الرياضي؟

اهداف البحث:

١. لإجراء التحليل الخاص بتاثير الذكاء الاصطناعي على تعليم الرياضيات.

٢. لتوضيح تاثيره على تقدم التفكير الرياضي.

٣. لتوضيح العلاقة المتبادلة بين الرياضيات والذكاء الاصطناعي.

٤. لتقييم التحديات المحتملة على المدى البعيد .

أهمية البحث:

لمن يسأل عن اهمية الذكاء الاصطناعي في الرياضيات حيث ساهم الذكاء الاصطناعي في تطوير طرق تدريس الرياضيات وتقديم حلول اكثر فاعلية كواحد من أكثر عبدالبر، 2024) ;للمشكلات الرياضية، كما ساعد في تحسين مستوى التفاعل مع المفاهيم الرياضية المعقدة (متولي وعيد، 2024 التقنيات المعاصرة تميزًا، إلى جانب الدور الحاسم للرياضيات كعلم أساسي في تطوير التفكير العلمي. تأتي هذه الدراسة التحليلية التي تهدف إلى إلقاء الضوء على منهجيات الاستفادة من التقنيات الحديثة لرفع مستوى جودة التعليم وبناء جيل قادر على اتخاذ القرارات وحل المشكلات بكل حداثة امام التقدم السريع للذكاء الاصطناعي.

المبحث الاول:الاطار المفاهيمي

١.الذكاء الاصطناعي: يشكل الذكاء الاصطناعي قسمًا فرعيا من علوم الكمبيوتر الذي يطمح الى إنشاء أنظمة قادرة على محاكاة المعرفة البشرية مثل التعلم والتفكير واتخاذ القرار من خلال استخدام الاسس الرياضية مثلا الجبر الخطي والتفاضل والتكامل وتطبيق الخوارزميات الرياضية والإحصائية.

٢.الرياضيات العامة: تشمل الرياضيات العامة مجموعة من البديهات والمفاهيم والاستنتاجات التي تزود الأفراد بالمشاكة في عمليات التفكير المنطقي وحل المشكلات اليومية وفهم العلاقات العددية.

٣. العلاقة بين الذكاء الاصطناعي والرياضيات العامة: العلاقة مبنية بشكل أساسي على التكامل بينهما.ان أنظمة الذكاء الاصطناعي لها جذور عميقة بشكل أساسي في المبادئ الرياضية، بينما تسهل هذه الأنظمة تعزيز فهم وتطبيق المفاهيم الرياضية (,.Goodfellowetal 2016).

المبحث الثاني : دور الذكاء الاصطناعي في الرياضيات حيث يلعب الذكاء الاصطناعي دورا محوريًا في النهوض بتعلم الرياضيات من خلال تسريع العمليات الحسابية المعقدة وتوفير حلول متعددة وتبسيط المفاهيم الرياضية وتسهيل تجارب التعلم الشخصية والكيفية وتقييم اداء المتعلم وقد تم إثبات هذا الدور

خضير وآخرون، 2025). ; جودة، 2024 ;(الجرمي، 2026

هنالك دور اخر للذكاء الاصطناعي هو توسيع افاق الدراسات الرياضية خاصة عندوجود بيانات ضخمة التي يصعب التعامل بالطرق الاعتيادية التقليدية في مجالات الهندسة، الاقتصاد، الطب، الفيزياء، علم الحاسوب وباقي العلوم الأخرى.

ممكن للطالب في وجود هذه التقنية ان ينتقل من مستوى تفكيري الى مستوى اخر وفقًا للقدرات العقلية التي يتمتع بها وليس وفق الصف الدراسي فقط.وكذلك ممكن ان ينتج تقليل للفجوات التعليمية الموجودة بين المتعلمين بكل مرونة وفاعلية ضمن العملية التربوية (,2024 OpesemowoandAdewuyi).

المبحث الثالث: التفكير الرياضي

يساهم الذكاء الاصطناعي في تنمية مهارات التفكير العالية والمعرفي العميق لدى الدارسين في مجال الرياضيات و توفير بيئات تعلم متنوعة وذكية (مصطفى، 2024 ;القريني، 2026) . وذلك من خلال:

1. استخدام التفكير المنطقي والتفكير التحليلي لدى الدارسين من خلال خطوات إرشادية تمنح فهم الية الحل وليس فقط الحصول على النتيجة النهائية والوصول الى حل للمشكلات (,.Luckinetal 2016).
2. الوقوف على نقاط الضعف والقوة لدى المتعلمين وتقديم أنشطة واختبارات تتناسب مع قدراتهم وبالتالي سوف يرتفع مستوى الفهم والتفكير بصورة تدريجية ومتسقة (يونسكو، 2023).

3. ربط المفاهيم مع بعضها من قبل المتعلمين وترتيب خطوات الحل من نتائج استخدام تطبيقات الذكاء الاصطناعي وهذ جانب مهم جدا في خلق تفكير استدلالي بمستوى عالي (Zawacki-Richteretal., 2019).

4. الكشف عن الأخطاء والقيام بتصحيحها بالوقت المناسب مما يساعد على تطوير وتحسين القدرة على حل المسائل الرياضية (Holmesetal., 2019).

5. مقارنة الحلول للمسالة الواحدة التي تقبل اكثر من طريقة من قبل المتعلمين واختيار الأفضل منها وهذا سوف ينتج عنه مرونة في العقل وتفكير إبداعي (OECD ,2021).

علاوة على ذلك، فإنه يخلق بيئات تعليمية تفاعلية تعزز الفهم العميق (القريني ،2026).

مما تقدم يمكن تعريف التفكير الرياضي بانه فهم العديد من المبادئ والمفاهيم الرياضية وتحليل النتائج واكتشاف الصيغ المنطقية للأسئلة الرياضية من خلال عمليات عقلية يقوم بها الفرد بمساعدة مهارات الاستنتاج والبرهان والتعميم والحكم المبني على الفرضيات الصحيحة (NCTM , 2014).

المبحث الرابع:

تحديات الاعتماد المفرط على التقنيات التكنولوجية: ان العملية التعليمية تخطو بسرعة كبيرة نحو الحداثة بفضل تقنيات الذكاء الاصطناعي وهذا يعتبر ذو أهمية بالغة بالنسبة للمتعلمين لانها توفر أدوات مختلفة تساعد على تنفيذ النشاطات التعليمية في مجال تدريس الرياضيات وعملياتها من تحليل الأداء بدقة الى تقديم التغذية الراجعة بصورة فورية .من اجل توفير بيئة تعليمية جيدة وتعلم فردي متميز ومفاهيم رياضية مبسطة اصبح للذكاء الاصطناعي دور كبير لكن هناك تحديات كبيرة تواجه هذه التقنية وفعاليتها وأهدافها (Holmes et al ,. 2019)

وتكمن التحديات في ما يأتي:

1. عدم امتلاك المعلمين المهارات الحديثة الكافية التي تمكنهم من استخدام أدوات الذكاء الاصطناعي المناسبة والمهارات الرقمية المتقدمة لتحقيق الأهداف التعليمية (يونيسكو ، .(2023

2. ممكن ان يتعرض دور المعلم الى التقليل بسبب الإفراط الزائد في الاعتماد على تقنيات الذكاء الاصطناعي اضافة الى الحصول على الحلول الجاهزة بدون المرور بالفهم العميق لمواضيع الرياضيات (Luckinetal 2016 ,.).

3. يجب على المعلمين التأكد من الإجابات التي تعطيها تقنيات الذكاء الاصطناعي لانه في بعض الأحيان لا تكون بالدقة المطلوبة وبالأخص مواضع المبرهنات (يونيسكو، 2023).

4. عند اداء الاختبارات عن طريق الأجهزة الذكية سوف يكون الإنجاز دون فهم (OECD , 2021).

5. هنلك عايق جدا مهم يواجه العملية التعليمية وهو عدم توفر الأجهزة الحديثة للتعليم الإلكتروني مزودة بالإنترنت والبرامج المتطورة تحول دون الاستفادة التامة (, OECD 2021).

6. ان الاستخدام غير المنظم للتقنيات الحديثة في الذكاء الاصطناعي له تاثير كبيرًا على التفكير المستقل للطالب (الساقاطي، 2025).

المبحث الخامس: مستقبل الذكاء الاصطناعي في الرياضيات

يشير مسار الحياة المستقبلية إلى دمج تدريجي للذكاء الاصطناعي في الأطر التعليمية، مع التركيز على دعم التعلم الفردي وتعزيز جودة الفهم الرياضي، مع الحفاظ على دور المتعلم في عمليات التفكير والتفكير التحليلي (اليونسكو، 2023). وسيصبح جزء اساسي من مستقبل الرياضيات سواء في التعلم او البيانات الرياضية (خضير وآخرون، 2025 ;الشنقيطي والحسن، 2025) من خلال ما يأتي :

1. لكل متعلم مستوى وسرعة تعلم تتناسب مع المسارات التعليمية الفردية التي يصممها الذكاء الاصطناعي تساعد على معالجة جوانب الضعف بصورة دقيقة وفعالة (,2016. Luckinetal).

2. توفير بيئة تعليمية ذكية للمتعلمين حيث يحصل دمج الواقع الحقيقي مع الواقع المساند من أجل استيعاب وفهم افضل (,2021 OECD).

3. في ظل تقنيات الذكاء الاصطناعي سوف يكون تصحيح الأخطاء وتقديم التغذية الراجعة وتحسين اداء المتعلمين الرياضي في المستويات العالية (يونيسكو، 2023).

4. لكل معلم خطة دراسية سوف تسهل اعدادها ضمن التقنية الجديدة وتصميم مختلف الأنشطة والاختبارات الرياضية والحصول على نتائج خاضعة للتحليل . مما يمنح وقت وفير وجهد مع التركيز على الجوانب التربوية والتعليمية والإنسانية (2019 .,. Holmesetal).

5. تنمية مهارات التفكير الإبداعي وطرق حل المشكلات مما يشجع على التحليل والاستدلال للمتعلمين (ZawackiRichteretal ,. 2019).

الخاتمة:

توصلت الدراسة التحليلية الى اهم استنتاج يبحث عنه الكثيرون وهو ان الذكاء الاصطناعي يعمل كأداة فعالة في النهوض بتعليم الرياضيات، ومع ذلك، فإنه يتطلب تطبيقا حكيما يدمج الصور الحديثة للتكنولوجيا مع تنمية المهارات المعرفية لتسهيل نتائج التعلم الفعالة والدائمة. وفي العصر الحديث يعتبر الذكاء الاصطناعي من المحركات الرئيسية لتطور الرياضيات سواء كان في التعليم او التطبيقات العلمية. ومن اجل تطور تقني افضل يجب ان تتكامل الخبرة التربوية مع الخبرة التكنولوجية في اجواء أمنة نحو المستقبل (, 2024 OpesemowoandAdewuyi).

التوصيات :

هنالك توصيات نتجت عن هذه الدراسة منها ربط تطبيقات الذكاء الاصطناعي في مناهج الرياضيات، وتدريبات المعلمين على الاستخدام الأمثل لهذه التقنيات الحديثة، مع التأكيد على أهمية الحفاظ على دور المتعلم في التفكير والتحليل وعدم الاعتماد الكامل على الأنظمة الذكية. كما توصي بإجراء المزيد من الدراسات حول أثر الذكاء الاصطناعي في تنمية مهارات التفكير الرياضي لدى مختلف المراحل التعليمية مع مراعاة الفروق الفردية بين المتعلمين والتحقق من المادة العلمية قبل تقديمها . استخدام الذكاء الاصطناعي في التقويم ليس فقط كونه أداة للقياس الخاصة بالامتحان النهائي فحسب وانما يهدف الى متابعة تقدم المتعلم أثناء عملية التعلم.

المصادر:

المصادر العربية:

عبدالبر، ع. م. (2024). استخدام تطبيقات الذكاء الاصطناعي في تدريس الرياضيات (بين الآمال الواعدة والمحاذير الواجبة). مجلة كلية التربية، جامعة المنوفية، 35(4)، 112–138.

الجرمي، إ. ا. ك. (2026). دور الذكاء الاصطناعي في تحسين تعلم الرياضيات في التعليم العالي. مجلة العلوم الشاملة، 10(39)، 536–547.

جودة، س. ح. م. (2024). برنامج تعليمي إرشادي قائم على الذكاء الاصطناعي التوليدي للمتعثرين أكاديميًا في الرياضيات بالمرحلة الجامعية. مجلة كلية التربية، جامعة بنها، 39(2)، 57–82.

خضير، ل. خ.، العيثاوي، م. ص.، وسعادة، ج. أ. (2025). تطبيقات الذكاء الاصطناعي في تعليم الرياضيات: دراسة ميدانية على مدرسي الرياضيات ومدرساتها في المرحلة المتوسطة والإعدادية. بحوث عربية في مجالات التربية النوعية، 38(2)، 245–286.

الساقاطي، ن. م. (2025). الذكاء الاصطناعي والتعلم التكيفي في تدريس الرياضيات. مجلة العلوم الشاملة، 9(36)، 771–779. https://cjos.histr.edu.ly/index.php/journal/ar/article/view/283

الشنقيطي، ع.، والحسن، ر. ع. (2025). آراء المعلمين والمعلمات حول استخدام الذكاء الاصطناعي التوليدي في تعليم الرياضيات. المجلة الدولية للعلوم التربوية والإنسانية المعاصرة، 4(1)، 255–286. https://faculty.ksu.edu.sa/ar/alhassan/publication/418676

القريني، غادة سعود. (2026). فاعلية استخدام تطبيق Photomathالقائم على الذكاء الاصطناعي في تنمية مهارات التفكير العليا في الرياضيات بالمرحلة المتوسطة. Journal of Arts, Literature, Humanities and Social Sciences، (128)، 171–193. https://doi.org/10.33193/JALHSS.128.2026.1622

متولي، ع. س.، وعيد، ن. ي. (2420). الذكاء الاصطناعي في تعليم الرياضيات: وجهات النظر والممارسات والتحديات. مجلة المناهج المعاصرة وتكنولوجيا التعليم.

مصطفى، أ. م. م. (2024). برنامج مقترح في مهارات التساؤل الصفي باستخدام بعض تطبيقات الذكاء الاصطناعي في التدريس لتنمية العمق المعرفي للطلاب المعلمين بشعبة الرياضيات. بحوث عربية في مجالات التربية النوعية.

References:

1. Baker, R. S., & Smith, L. (2019). Educ-AI-tion rebooted? Exploring the future of artificial intelligence in schools and colleges. Nesta.

2. Goodfellow, I., Bengio, Y., & Courville, A. (2016). Deep learning. MIT Press.

3. Holmes, W., Bialik, M., & Fadel, C. (2019). Artificial intelligence in education: Promises and implications for teaching and learning. Center for Curriculum Redesign.

4. Luckin, R., Holmes, W., Griffiths, M., & Forcier, L. B. (2016). Intelligence unleashed: An argument for AI in education. Pearson.

5. National Council of Teachers of Mathematics. (2014). Principles to actions: Ensuring mathematical success for all. National Council of Teachers of Mathematics.

6. OECD. (2021). Digital education outlook 2021: Pushing the frontiers with artificial intelligence, blockchain and robots. OECD Publishing. https://doi.org/10.1787/589b283f-en

7. Opesemowo, O. A. G., & Adewuyi, H. O. (2024). A systematic review of artificial intelligence in mathematics education: The emergence of 4IR. Eurasia Journal of Mathematics, Science and Technology Education, 20(7), Article em2478. https://8. doi.org/10.29333/ejmste/14762

8. Russell, S. J., & Norvig, P. (2021). Artificial intelligence: A modern approach (4th ed.). Pearson.

9. UNESCO. (2023). Guidance for generative AI in education and research. UNESCO. https://unesdoc.unesco.org/ark:/48223/pf0000386693

10. Zawacki-Richter, O., Marín , V. I., Bond, M., & Gouverneur, F. (2019). Systematic review of research on artificial intelligence applications in higher education. International Journal of Educational Technology in Higher Education, 16(1), Article 39. https://doi.org/10.1186/s41239-019-0171-0

Visible–Light–Driven Metal–Free C–H Alkylation of Electron–Deficient N–Heteroarenes Catalyzed by Lawsone Isolated from Lawsonia inermis

أسماء عباس عبدالله العبادي – المديرية العامة لتربية بغداد الكرخ الثانية

ASSMA ABBAS ALABADY

Abstract

The direct C–H alkylation of electron-deficient N-heteroarenes is an effective approach to quickly create diversity in important pharmaceutical scaffolds. However, we often need expensive metal photocatalysts or carefully-designed radical precursors. Lawsone is a biomass-derived organophotocatalyst for visible-light-driven Minisci-type alkylation suggested in this paper.

The isolated chromophore exhibited a low-energy absorption band centered at 450 nm and was applied in the presence of blue-light irradiation with alkyl carboxylic acids and potassium persulfate. Yields of 12-product substrate set comprising quinoline, pyridine, pyrazine, pyrimidine, and quinoxalinone derivatives isolated in 48–88% (mean 70.4%, median 70.5%). The control experiment highlights that for productive conversion to happen, both light and lawsone are required. The sodium cyclohexanecarboxylate quenched the emission of lawsone with a Stern–Volmer constant of 127 M^{-1}. When they added the compound TEMPO, product formation stopped. A TEMPO-cyclohexyl adduct was observed and confirmed through GC-MS. Using light and dark periods showed that irradiation is required to continue conversion. The observations collectively support a radical photo-redox pathway that involves the reductive

quenching of photoexcited lawsone by a carboxylate donor model, decarboxylation and a Minisci addition to an N-heteroarene. This study results position a naturally sourced quinone chromophore as a promising platform for metal-free visible-light C–C bond formation while also defining the mechanistic and reproducibility data required for further development.

Keywords: visible-light photocatalysis; C–H functionalization; lawsone; biomass-derived organophotocatalyst; Minisci reaction; N-heteroarenes

1. Introduction

Medicinal chemistry often uses N-heteroarenes which are deficient in electrons. Directly installing carbon substituents onto the rings provides a short and effective strategy. The reaction is what is known as a radical addition. It occurs on an activated heteroaromatic ring. It quickly follows with rearomatization. This reaction is called the Minisci reaction. To this day, one of the best innate C–H functionalization methods remains for these scaffolds. [1]. Radicals can exist in a pool that is hard to reach. Unlike traditional methods, modern photoredox variants can produce radicals at far lower energies. As a result, latest photoredox varieties have increased the pool of available radicals and greatly reduced the thermal burden of. [2], while Jin and MacMillan showed that alcohols can serve as latent alkylating fragments through photoredox/HAT catalysis [3]. Further research has broadened heteroarene alkylation to include various types of radicals and halides. [4–8].

The growing interest in photoredox catalysis and metallaphotoredox catalysis for the introduction of geminal difluoroalkyl groups has led to several desulfurization methods involving

precious-metal photosensitizers. [5], micellar photoredox/bromide catalysis [9], and newer organophotocatalytic C(sp^3)–H activation platforms [12]. Excited states can render a generic version of the Minisci radical generation (Storck et al., 2019; Dawood et al., 2021; Hu et al., 2021; Zhong et al., 2021), however, naturally occurring quinones as chromophores have been relatively underexploited to exert catalytic control. [14,15]. The henna-derived chromophores ability to photosensitize has also been established by us in a light-driven materials system [16]. The research evaluated the performance of Iraqi Lawsonia inermis as an organophotocatalyst for an alkylation reaction. The study design was developed around various questions that require confirmation- whether the isolated chromophore accomplishes a visible light C–C bond forming reaction, whether the method tolerates multiple classes of electron-deficient N-heteroarenes, whether light, catalyst, and radical controls are consistent with photoredox reactivity, and how the yield distribution compares across the substrate panel. As a result, our claim to novelty is limited to this tested catalytic use, while it is not extended to crude henna..

2. Experimental Section

2.1 Materials, instrumentation, and laboratory controls

All commercially available chemicals were used as received where not otherwise stated. Henna leaves were gathered in Iraq's Wasit Governorate town of Al-Kut in March 2025. NMR spectra were recorded on a Bruker Avance 500 MHz. HRMS data were measured with Thermo Scientific LTQ Orbitrap XL. UV–Vis spectra were recorded on a Shimadzu UV-1800. Fluorescence measurement used a Jasco FP-8300. In a suitable institutional chemistry laboratory, trained staff performed photochemical studies using appropriate risk assessments, shielding and instrument operating procedures.

2.2 Isolation and characterization of lawsone

We performed Soxhlet extraction using 95% ethanol on a 100 g powder of henna leaves. The powder was dried in open air and ground. The vacuum extraction was concentrated and crystallized in ethanol/water (3:1). Subsequently, a crystalline orange isolate was obtained which is identified as lawsone .

UV–Vis (EtOH) λmax (log ε): 270 (4.12), 335 (3.63), 450 (3.31) nm. ^{1}H NMR (500 MHz, DMSO-d_6): δ 11.82 (s, 1H, OH), 8.06 (dd, J = 7.6, 1.3 Hz, 1H, ArH), 7.97 (dd, J = 7.6, 1.3 Hz, 1H, ArH), 7.85 (td, J = 7.6, 1.3 Hz, 1H, ArH), 7.78 (td, J = 7.6, 1.3 Hz, 1H, ArH), 6.35 (s, 1H, H-3). FTIR (KBr, cm^{-1}): 3420 (br, O–H), 1672 (C=O), 1640 (conj. C=O), 1590, 1450. These assignments are consistent with the quinone chromophore and the spectral behavior reported for lawsone-containing systems [14,15].

2.3 General photocatalytic alkylation procedure

The model transformation used heteroarene (0.20 mmol), alkyl carboxylic acid (0.40 mmol), $K_2S_2O_8$ (0.40 mmol), and lawsone (0.004 mmol, 2 mol%) in DMSO/H_2O (1:1 v/v, 2 mL) under 450 nm blue-light irradiation and an inert atmosphere for 24 h at an internal temperature of 28–30 °C. Products were isolated by aqueous workup, organic extraction, drying, concentration, and chromatographic purification. Exact reactor geometry, incident photon flux, vessel-to-light distance, and analytical calibration were not quantified in the present dataset and are therefore treated as reproducibility limitations.

2.4 Mechanistic experiments

For fluorescence quenching, a 5×10^{-5} M lawsone solution in DMSO/H_2O (1:1) was excited at 450 nm and emission at 530 nm was monitored while sodium cyclohexanecarboxylate was added. KSV was determined from the slope of I_0/I versus quencher concentration. Radical-trapping experiments used TEMPO under the reported model conditions and the crude mixture was examined by GC–MS. In the light/dark experiment, the model reaction was alternated between 4 h irradiation and 4 h dark periods, with aliquots analyzed by GC.

2.5 Data treatment and reproducibility

Optimization results are reported as GC yields using n-dodecane as internal standard, with the isolated yield shown in parentheses where available. The substrate-scope table reports mean isolated yields from two runs (n = 2). Because replicate-level yields are not reported in the present dataset, replicate standard deviations and inferential hypothesis tests are not presented. Instead, the

12 reported mean isolated yields were summarized descriptively by mean, sample standard deviation, median, interquartile range, range, and coefficient of variation. Because the 12 substrates are chemically non-equivalent, these statistics describe the distribution of reported scope yields and must not be interpreted as replicate precision or a formal comparison of substrate classes.

3. Results and Discussion

3.1 Optical characterization of the isolated lawsone

The UV–Vis spectrum of the isolated chromophore shows three bands centered at 270, 335 and 450 nm (Figure 1). The low-energy band coincides with the emission range of 450 nm blue LEDs utilized within the reaction screen. This finding offers an experimental basis to examine the isolated substance under blue light. It does not on its own assign excited state redox potential or spin multiplicity requiring electrochemical and time-resolved photophysical measurement.4

Figure 1. UV-Vis absorption spectrum of lawsone extracted from Iraqi *Lawsonia inermis* (EtOH, 25 °C)

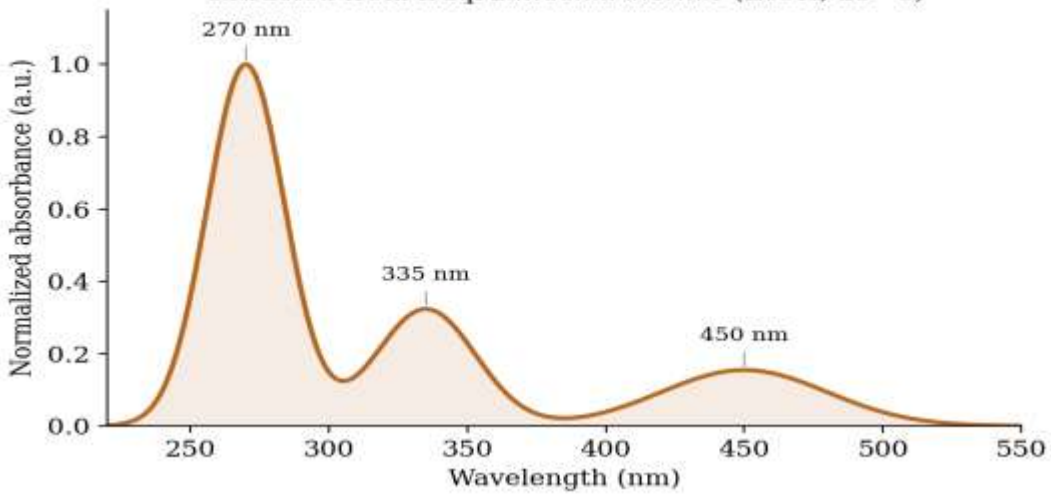

Figure 1. UV–Vis absorption spectrum of lawsone isolated from Iraqi Lawsonia inermis (EtOH, 25 °C).

3.2 Optimization and control experiments

We chose the alkylation of 4-methylquinoline with cyclohexanecarboxylic acid as model reaction. The control matrix indicates no product occurrence in the dark as per the data in entries 1 and 14. No effective conversion takes place in the dark with lawsone (Table 1). The GC yield under irradiation after removing lawsone provides only 5% (entry 3). The standard conditions presented yield a GC yield of 78% and an isolated yield of 75% (entry 2). DMSO/H2O (1:1) is better than the others tested (MeCN/H2O and water) and in entry 1 as K2S2O8 is better than the others (ammonium and sodium persulfate) tested (entries 2 and 4–8). Lessening of.

Table 1. Optimization of reaction parameters

Entry	**Variation from standard conditions**	**Yield (%)**
1	No light, no lawsone	0
2	No light	0
3	Dark, lawsone (2 mol%)	0
4	No lawsone	5
5	None (standard)	78 (75)
6	CH_3CN/H_2O (1:1) instead of $DMSO/H_2O$	53

Entry	Variation from standard conditions	Yield (%)
7	H_2O only	22
8	$(NH_4)_2S_2O_8$ instead of $K_2S_2O_8$	68
9	$Na_2S_2O_8$ instead of $K_2S_2O_8$	61
10	1.5 equiv $K_2S_2O_8$	65
11	Riboflavin (2 mol%) instead of lawsone	62
12	Lawsone 1 mol%	75

Standard conditions: model heteroarene (0.20 mmol), carboxylic acid (0.40 mmol), $K_2S_2O_8$ (0.40 mmol), lawsone (2 mol%), DMSO/H_2O (1:1), 450 nm irradiation, 24 h. GC yield with n-dodecane internal standard; isolated yield in parentheses.

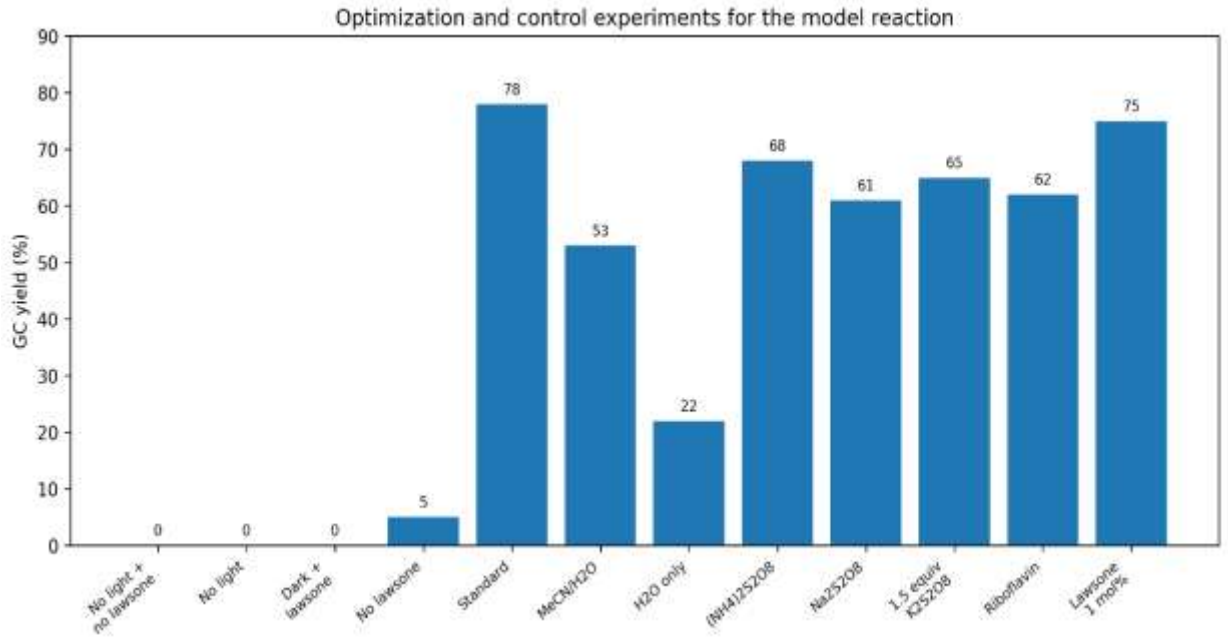

Figure 2. Optimization and control profile for the model reaction. Values are the GC yields reported in Table 1.

3.3 Substrate scope

The reported scope includes 12 products spanning quinoline, pyridine, pyrazine, pyrimidine, and quinoxalinone frameworks (Table 2). Electron-deficient azaarenes generally gave moderate-to-good yields, with the highest isolated yield obtained for the quinoxalin-2(1H)-one derivative 3g (88%). 4-Cyanopyridine afforded 3d in 85%, while 6-chloroquinoline gave 3b in 82%. The scope also includes secondary, tertiary, arylmethyl, and protected heterocyclic radical precursors. The lower yield for 2-phenylquinoline (3l, 48%) is consistent with a less favorable combination of steric and electronic effects at the reactive position, but this interpretation remains qualitative without rate or competition experiments. Recent Minisci studies similarly show that radical precursor class and heteroarene activation strongly influence efficiency and site selectivity [10–13].

Table 2. Substrate scope of lawsone-catalyzed C–H alkylation

Product	**Heteroarene**	**Carboxylic acid**	**Isolated yield (%)**
3a	4-Methylquinoline	Cyclohexanecarboxylic acid	75
3b	6-Chloroquinoline	Cyclohexanecarboxylic acid	82
3c	Methyl quinoline-3-carboxylate	Cyclohexanecarboxylic acid	71

Product	Heteroarene	Carboxylic acid	Isolated yield (%)
3d	4-Cyanopyridine	Cyclohexanecarboxylic acid	85
3e	Pyrazine	Cyclohexanecarboxylic acid	72
3f	Pyrimidine	Cyclohexanecarboxylic acid	67
3g	Quinoxalin-2(1H)-one	Cyclohexanecarboxylic acid	88
3h	4-Methylquinoline	Tetrahydro-2H-pyran-4-carboxylic acid	70
3i	4-Methylquinoline	Pivalic acid	65
3j	4-Methylquinoline	4-Methoxyphenylacetic acid	64
3k	4-Methylquinoline	N-Boc-piperidine-4-carboxylic acid	58
3l	2-Phenylquinoline	Cyclohexanecarboxylic acid	48

Conditions as in Table 1, entry 5. Values are mean isolated yields from two reported runs. For 3a, the isolated yield (75%) is used rather than the GC yield (78%).

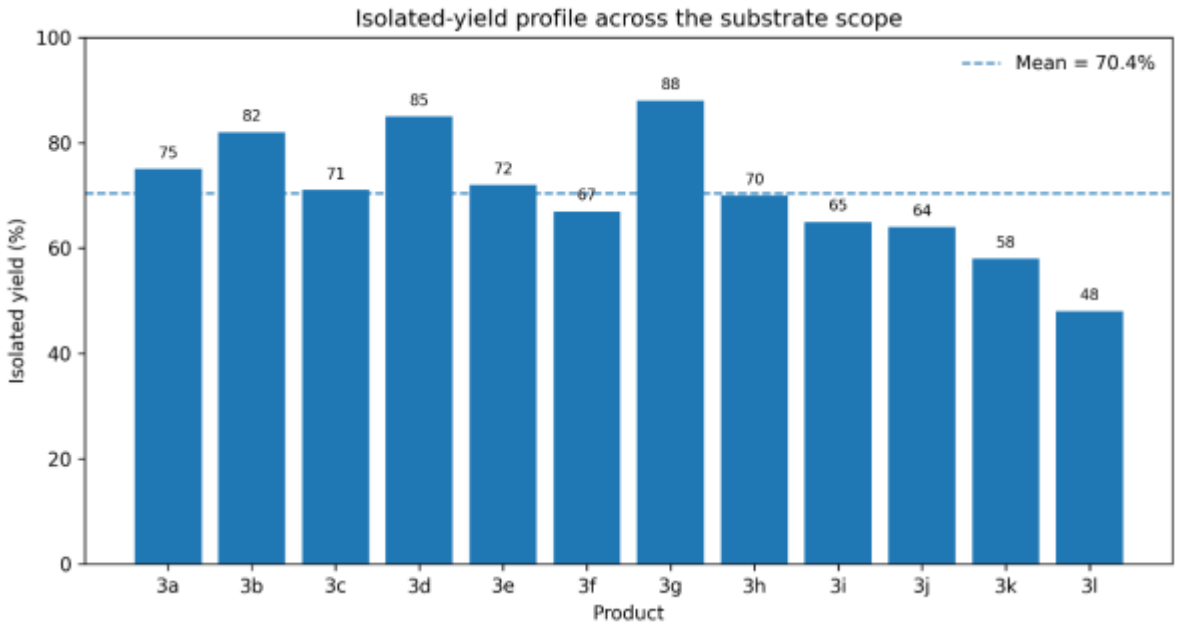

Figure 3. Isolated-yield profile across the 12-product substrate scope. The dashed line represents the descriptive mean (70.4%).

3.4 Descriptive summary of scope yields

Across the 12 reported mean isolated yields, the descriptive mean was 70.4% and the median was 70.5%. The sample standard deviation across chemically different substrate means was 11.4 percentage points, the interquartile interval was 64.8–76.8%, and the full range was 48–88% (Table 3). The coefficient of variation of the scope-yield distribution was 16.1%. These metrics are included to summarize the breadth of the reported scope; they are not a substitute for replicate-level uncertainty because individual yield values from the two runs are not reported in the present dataset.

Table 3. Exploratory descriptive statistics for reported substrate-scope yields

Statistic	Value
Number of products (n)	12
Mean isolated yield	70.4%
Median	70.5%
Sample SD across product means	11.4 percentage points
Q1–Q3	64.8–76.8%
Minimum–maximum	48–88%
Coefficient of variation	16.1%

Descriptive summary across chemically non-equivalent products. Values do not quantify replicate precision and no inferential comparison is claimed.

3.5 Representative product characterization

2-Cyclohexyl-4-methylquinoline (3a). Pale yellow oil. ^{1}H NMR (500 MHz, $CDCl_3$): δ 8.09 (d, J = 8.4 Hz, 1H), 7.96 (d, J = 8.4 Hz, 1H), 7.68 (ddd, J = 8.4, 6.9, 1.3 Hz, 1H), 7.52 (ddd, J = 8.4, 6.9, 1.2 Hz, 1H), 7.18 (s, 1H), 2.93 (tt, J = 11.5, 3.4 Hz, 1H), 2.72 (s, 3H), 2.10–1.99 (m, 2H), 1.97–1.87 (m, 2H), 1.82–1.73 (m, 1H), 1.71–1.60 (m, 2H), 1.51–1.36 (m, 2H), 1.34–1.22 (m, 1H). ^{13}C NMR (126 MHz, $CDCl_3$): δ 163.4, 147.7, 144.4, 129.9, 129.2, 126.9, 125.2,

123.8, 118.7, 45.0, 32.8 (2C), 26.5, 25.9 (2C), 19.0. HRMS (ESI) m/z $[M+H]^+$ calcd for $C_{16}H_{20}N$ 226.1590; found 226.1594.

2-Cyclohexyl-4-cyanopyridine (3d). White solid, mp 48–50 °C. ^1H NMR (500 MHz, $CDCl_3$): δ 8.80 (d, J = 5.0 Hz, 1H), 7.79 (s, 1H), 7.44 (dd, J = 5.0, 1.3 Hz, 1H), 2.79 (tt, J = 11.2, 3.5 Hz, 1H), 2.03–1.93 (m, 2H), 1.89–1.80 (m, 2H), 1.77–1.68 (m, 1H), 1.63–1.51 (m, 2H), 1.45–1.28 (m, 3H). HRMS (ESI) m/z $[M+H]^+$ calcd for $C_{12}H_{15}N_2$ 187.1230; found 187.1233.

3.6 Mechanistic evidence and working hypothesis

Sodium cyclohexanecarboxylate quenched the steady-state emission of lawsone, producing a linear Stern–Volmer relationship with KSV = 127 M^{-1} (Figure 4). Within the limits of steady-state data, the result is consistent with an interaction between the carboxylate donor model and photoexcited lawsone. A definitive assignment of dynamic electron-transfer quenching would require excited-state lifetime measurements, and the use of a sodium carboxylate in the quenching experiment should not be assumed to reproduce every acid–base microenvironment of the preparative reaction.

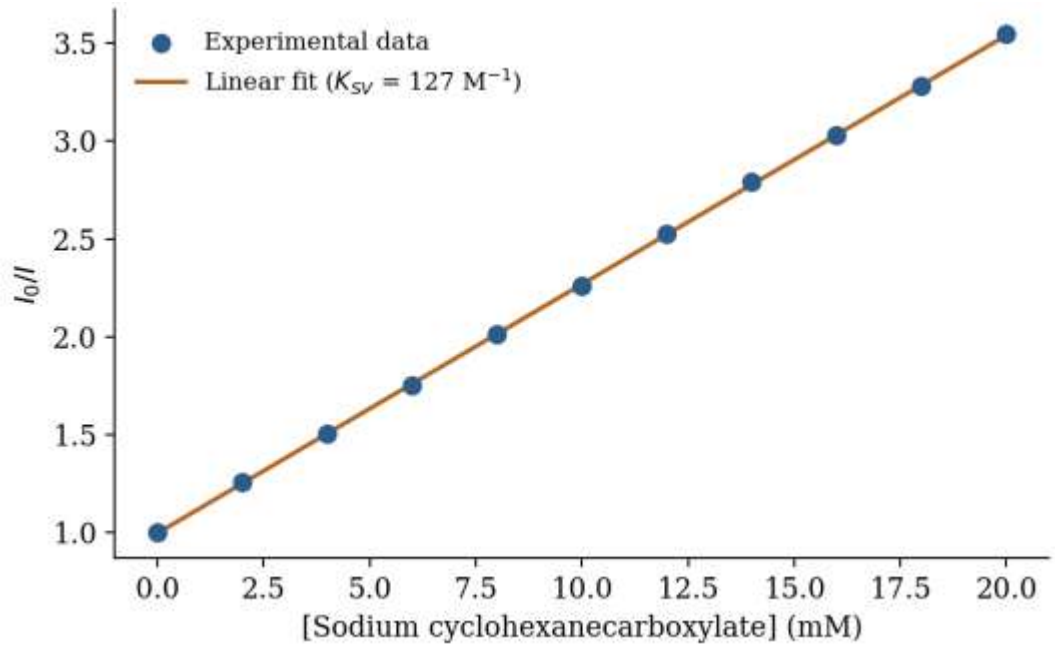

Figure 4. Stern–Volmer plot for quenching of lawsone emission (λex 450 nm, λem 530 nm) by sodium cyclohexanecarboxylate. Reported KSV = 127 M^{-1}.

TEMPO suppressed formation of the model product and GC–MS analysis was reported to show a cyclohexyl–TEMPO adduct (m/z 240.2), supporting the participation of a carbon-centered radical. Product formation paused during dark intervals and resumed after re-irradiation. This light/dark behavior demonstrates that sustained conversion requires continued photoexcitation under the tested conditions; however, light/dark cycling alone does not measure radical-chain length or exclude a short chain contribution. A conservative working hypothesis is shown in Figure 5: lawsone absorbs visible light, the excited chromophore undergoes reductive quenching with a carboxylate donor model, the resulting carboxyl radical decarboxylates, and the carbon-centered radical adds to the activated N-heteroarene. Persulfate is proposed to participate in catalyst turnover and oxidation/rearomatization steps. The scheme is deliberately presented as a

mechanistic model rather than direct proof of an excited triplet state or a unique elementary sequence.

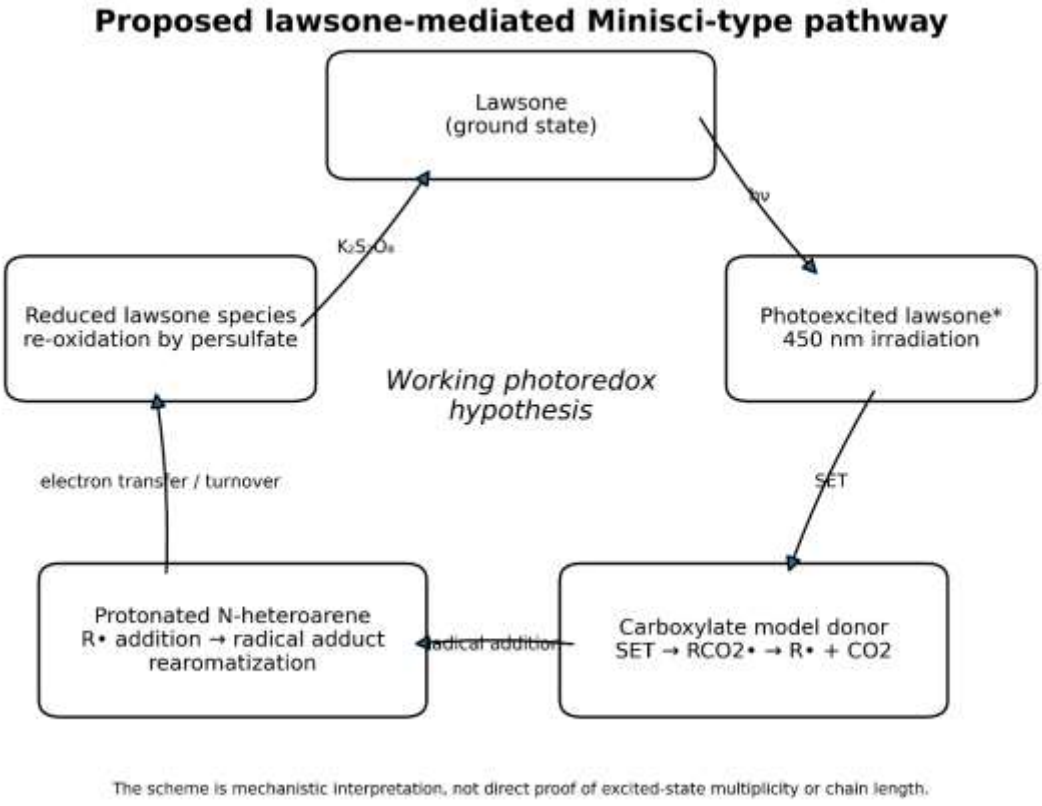

Figure 5. Working photoredox hypothesis for lawsone-mediated Minisci-type alkylation. The scheme summarizes a mechanism consistent with the reported controls but does not establish excited-state multiplicity or chain length.

3.7 Sustainability, significance, and limitations

The main aspect of sustainability targeted by the study relates to the sourcing of the catalyst of the system: the chromophore that was tested had been taken from a plant feedstock rather than being added to the reaction mixture as a precious-metal complex. The introduction of blue light and a water co-solvent further illustrates the current interest in mild photochemical C–H functionalization. Quantitative green-chemistry claims are intentionally restricted because there is not yet a complete process mass balance. In the future, any rigorous assessment of a process should state its reaction mass efficiency, process mass intensity or E-factor with an explicit system boundary that includes the extraction solvent, chromatography and aqueous persulfate waste.

The mechanistic dataset will support but will not prove. Currently present evidence establishes light dependence, radical trapping and steady-state fluorescence quenching.

Fluorescence lifetimes, cyclic voltammetry, transient absorption or EPR, quantum-yield measurements and a direct comparison between isolated natural lawsone and an authenticated commercial standard would assist with stronger causal assignment. Variation in plant-derived material from batch to batch should be quantified. That limitation challenges not the measured reactivity but rather identifies those experiments that a specialist, high-selectivity chemistry journal is most likely to request.

4. Conclusion

The study examined a biomass-derived organophotocatalyst called lawsone sourced from Lawsonia inermis for a C–H alkylation. Using the blue-light conditions described here, we obtained 12 alkylated products in 48 – 88% isolated yield (median scope yield 70.5%.). The use of control experiments, radical trapping, steady-state fluorescence quenching has been undertaken to rule out alternative pathways. The results underpin a light-dependent radical pathway where photoexcited lawsone is reductively quenched by a carboxylate donor model. Available evidence does not rule out direct crude-extract catalysis, excited-state multiplicity or lack of short radical-chain contribution, we thus present the cycle as a working photoredox hypothesis. Lawsone from natural sources looks to be a new promising chromophore to metal-free photoredox.

References

1. Duncton, M. A. J. Minisci reactions: Versatile CH-functionalizations for medicinal chemists. MedChemComm 2011, 2, 1135–1161. https://doi.org/10.1039/C1MD00134E.
2. DiRocco, D. A.; Dykstra, K.; Krska, S.; Vachal, P.; Conway, D. V.; Tudge, M. Late-stage functionalization of biologically active heterocycles through photoredox catalysis. Angew. Chem. Int. Ed. 2014, 53, 4802–4806. https://doi.org/10.1002/anie.201402023.
3. Jin, J.; MacMillan, D. W. C. Alcohols as alkylating agents in heteroarene C–H functionalization. Nature 2015, 525, 87–90. https://doi.org/10.1038/nature14885.

4. Huff, C. A.; Cohen, R. D.; Dykstra, K. D.; Streckfuss, E.; DiRocco, D. A.; Krska, S. W. Photoredox-catalyzed hydroxymethylation of heteroaromatic bases. J. Org. Chem. 2016, 81, 6980–6987. https://doi.org/10.1021/acs.joc.6b00811.

5. Genovino, J.; Lian, Y.; Zhang, Y.; Hope, T. O.; Juneau, A.; Gagné, Y.; Ingle, G.; Frenette, M. Metal-free visible-light C–H alkylation of heteroaromatics via hypervalent iodine-promoted decarboxylation. Org. Lett. 2018, 20, 3229–3232. https://doi.org/10.1021/acs.orglett.8b01085.

6. Bissonnette, N. B.; Boyd, M. J.; May, G. D.; Giroux, S.; Nuhant, P. C–H functionalization of heteroarenes using unactivated alkyl halides through visible-light photoredox catalysis under basic conditions. J. Org. Chem. 2018, 83, 10933–10940. https://doi.org/10.1021/acs.joc.8b01589.

7. Garza-Sanchez, R. A.; Patra, T.; Tlahuext-Aca, A.; Strieth-Kalthoff, F.; Glorius, F. DMSO as a switchable alkylating agent in heteroarene C–H functionalization. Chem. Eur. J. 2018, 24, 10064–10068. https://doi.org/10.1002/chem.201802352.

8. Perkins, J. J.; Schubert, J. W.; Streckfuss, E. C.; Balsells, J.; ElMarrouni, A. Photoredox catalysis for silyl-mediated C–H alkylation of heterocycles with non-activated alkyl bromides. Eur. J. Org. Chem. 2020, 2020, 1515–1522. https://doi.org/10.1002/ejoc.201900611.

9. Santos, M. S.; Cybularczyk-Cecotka, M.; König, B.; Giedyk, M. Minisci C–H alkylation of heteroarenes enabled by dual photoredox/bromide catalysis in micellar solutions. Chem. Eur. J. 2020, 26, 15323–15329. https://doi.org/10.1002/chem.202002320.

10. Bieszczad, B.; Perego, L. A.; Melchiorre, P. Photochemical C–H hydroxyalkylation of quinolines and isoquinolines. Angew. Chem. Int. Ed. 2019, 58, 16878–16883. https://doi.org/10.1002/anie.201910641.

11. Rieder, S.; Meléndez, C.; Dénès, F.; Jangra, H.; Mulliri, K.; Zipse, H.; Renaud, P. Radical chain monoalkylation of pyridines. Chem. Sci. 2021, 12, 15362–15373. https://doi.org/10.1039/D1SC02748D.

12. Basumatary, J.; Protim Phukan, K.; Bhuyan, S.; Gopal Roy, B. A direct visible-light mediated coupling of azaarenes with diversely functionalized alkyl carbons via organophotocatalytic sp^3C–H bond activation. Eur. J. Org. Chem. 2024, 27, e202400819. https://doi.org/10.1002/ejoc.202400819.

13. Xu, J.; Zhang, Y.; Xu, R.; Wang, Y.; Shen, J.; Li, W. Energy-transfer photocatalysis for Minisci C–H (amino)alkylation of heteroarenes using oxime esters as dual-role reagents. Org. Chem. Front. 2024, 11, 5122–5129. https://doi.org/10.1039/D4QO00836G.

14. Gomes, L. S.; Costa, É. O.; Duarte, T. G.; Köhler, M. H.; Rodrigues, B. M.; Ferreira, V. F.; da Silva, F. de C.; Iglesias, B. A.; Nascimento, V. Synthesis and evaluation of photophysical, electrochemical, and ROS generation properties of new chalcogen-naphthoquinone-1,2,3-triazole hybrids. RSC Adv. 2023, 13, 34852–34865. https://doi.org/10.1039/D3RA06977J.

15. Hijji, Y. M.; Barare, B.; Zhang, Y. Lawsone (2-hydroxy-1,4-naphthoquinone) as a sensitive cyanide and acetate sensor. Sens. Actuators B Chem. 2012, 169, 106–112. https://doi.org/10.1016/j.snb.2012.03.067.

16. Kader, D. A.; Mohammed, A. H.; Mohammed, S. J.; Aziz, D. M. Transforming henna: from natural dye to photosensitizer for efficient photocatalytic degradation of 4-nitrophenol using a green-synthesized ZnO@henna nanocomposite. RSC Adv. 2025, 15, 18245–18265. https://doi.org/10.1039/D5RA02154E.

لدى الجرذان البيضاء الحوامل وامتداداتها على ذريتها($CdCl_2$)التغيرات الهرمونية والتكوينية الناجمة عن التعرض لكلوريد الكادميوم

Hormonal and developmental changes caused by exposure to cadmium chloride ($CdCl_2$) in pregnant albino rats and their extensions to their offspring

أحمد محمد أحمد حادي

وزارة التربية / مديرية تربية نينوى / AM230009pep@st.tu.edu.iq

خلاصة

هدفت هذه الدراسة إلى تقييم القدرة الوقائية لمستخلص الفجل البري (Raphanus sativus) ضد سمية الكادميوم، مع دراسة تأثيرات كلوريد الكادميوم ($CdCl_2$) على هرمونات تناسلية مهمة في إناث الجرذان، مثل الهرمون المنبه للجريب (FSH) والهرمون اللوتيني (LH) والبروجسترون، بالإضافة إلى تأثيره على نمو الجنين. ضمت كل مجموعة من المجموعات الست خمس إناث يتراوح وزنهن بين 180 و200 غرام. تم إعطاء مجموعة ضابطة ماء مقطر، وتعرضت مجموعتان لكلوريد الكادميوم بجرعات 5 و 10 ملغم/كغم من وزن الجسم، وأعطيت مجموعة واحدة 2 مل من مستخلص الفجل البري، وكانت هناك مجموعتان للعلاج المشترك: أعطيت المجموعة الخامسة 5 ملغم/كغم من كلوريد الكادميوم بالإضافة إلى 2 مل من مستخلص الفجل، وأعطيت المجموعة السادسة 10 ملغم/كغم من كلوريد الكادميوم بالإضافة إلى 2 مل من مستخلص الفجل. لتحليل تأثيرات الكادميوم على الجهاز التناسلي، والأثر الوقائي لمستخلص الفجل البري ضد سمية هذا المعدن الثقيل، تم تتبع مستويات الهرمونات بعد العلاج، وإجراء فحوصات للجنين أثناء الحمل. أدى العلاج بمستخلص الفجل البري إلى استعادة جزئية لمستويات هرمونات FSH وLH والبروجسترون، والتي تبين أنها مضطربة بشكل ملحوظ في الحيوانات المعرضة للكادميوم، بالإضافة إلى انخفاض ملحوظ ($P \leq 0.05$) في وظيفة المبيض. كشف التحليل النسيجي للأجنة عن عيوب نمائية وتأخر في النمو في المجموعات المعرضة للكادميوم، إلا أن تناول مستخلص الفجل البري بالتزامن مع الكادميوم خفف من حدة هذه التغيرات، مما يشير إلى دور وقائي محتمل. تُظهر هذه النتائج أن التطور قبل الولادة ووظيفة المبيض والتوازن الهرموني تتأثر سلبًا بكلوريد الكادميوم، في حين يبدو أن مستخلص الفجل البري يُعاكس هذه الآثار الضارة.

الكلمات المفتاحية: كلوريد الكادميومهرمون FSH؛ هرمون LH؛ البروجسترون؛ الفجل البري

Abstract

This study aimed to evaluate the protective potential of wild radish extract (Raphanus sativus) against cadmium toxicity, while also investigating the effects of cadmium chloride ($CdCl_2$) on important reproductive hormones in female rats, such as follicle-stimulating hormone (FSH), luteinizing hormone (LH), and progesterone, as well as its effect on fetal development. Each of the six groups consisted of five female rats weighing between 180 and 200 grams. One control group received distilled water, two groups were exposed to cadmium chloride at doses of 5 and 10 mg/kg body weight, one group received 2 ml of wild radish extract, and two groups received a combination treatment: the fifth group received 5 mg/kg cadmium chloride plus 2 ml of radish extract, and the sixth group received 10 mg/kg cadmium chloride plus 2 ml of radish extract. To analyze the effects of cadmium on the reproductive system and the protective effect of radish extract against the toxicity of this heavy metal, hormone levels were monitored post-treatment, and fetal examinations were performed during pregnancy. Treatment with radish extract resulted in partial restoration of FSH, LH, and progesterone levels, which were significantly disrupted in cadmium-exposed animals, as well as a marked decrease ($P \leq 0.05$) in ovarian function. Histological analysis of the fetuses revealed developmental defects and growth retardation in the cadmium-exposed groups; however, concomitant administration of radish extract mitigated these changes, suggesting a potential protective role. These results demonstrate that prenatal

development, ovarian function, and hormonal balance are negatively affected by cadmium chloride, while radish extract appears to counteract these adverse effects.

Keywords: Cadmium chloride, FSH hormone, LH hormone, progesterone, radish

مقدمة

من بين العناصر الـ 105 الموجودة في الجدول الدوري، يُصنف ما يقرب من 80 عنصرًا على أنها معادن، وتشير البيانات إلى أن حوالي 30 منها ضارة بالبشر.(1)تُعتبر المعادن الثقيلة، بما في ذلك الكادميوم والزرنيخ والسيلينيوم والرصاص والزئبق والموليبدينوم، من الملوثات البيئية شديدة السمية نظرًا لقدرتها على دخول جسم الإنسان عن طريق الاستنشاق أو الابتلاع أو الامتصاص عبر الجلد.(2).

يُعد الكادميوم (Cd) ملوثًا بيئيًا واسع الانتشار، وقد صنفته الوكالة الدولية لأبحاث السرطان كمادة مسرطنة للإنسان.(3؛ 4)منذ اكتشافه في أوائل القرن العشرين، استُخدم الكادميوم على نطاق واسع في العديد من التطبيقات الصناعية، مما أدى إلى تلوث بيئي كبير وما تبعه من تلوث للأغذية عبر الهواء والماء والتربة.(5)والأهم من ذلك، أنه بعد دخول الكادميوم إلى الجسم عبر الجهازين التنفسي والهضمي، يمكن أن يؤدي إلى أمراض مزمنة وإلحاق الضرر بالعديد من أجهزة الجسم.(6؛ 7).

تم وضع العديد من النماذج للسمية الخلوية الناجمة عن الكادميوم، مما أدى إلى اقتراح آليات مختلفة لسمية الكادميوم، مثل الإجهاد التأكسدي، والتكاثر الخلوي غير الطبيعي، والتأثيرات المتعلقة بالمثيلة، وتلف الحمض النووي، وتثبيط مسارات إصلاح الحمض النووي.(8؛ 9)من المعروف أن سمية الكادميوم تنتج في الغالب عن الإجهاد التأكسدي(10)وفقًا لأبحاث سابقة، يمكن أن يتسبب كل من كبريتات الكادميوم ($CdSO_4$) وكلوريد الكادميوم ($CdCl_2$) في إنتاج الخلايا لكميات مفرطة من أنواع الأكسجين التفاعلية (ROS)، والتي يمكن أن تُلحق الضرر بالحمض النووي (DNA) وتسبب تكسر الكروموسومات داخل الخلايا، مما يؤدي في النهاية إلى تلف الخلايا.(11؛ 12)ومن المثير للاهتمام أن مستويات أنواع الأكسجين التفاعلية داخل الخلايا ودرجة تلف الخلايا تُظهر علاقة استجابة للجرعة مع تركيزات كلوريد الكادميوم وكبريتات الكادميوم(12)يُعد مستخلص الفجل (Raphanus sativus) مثالاً بارزاً، حيث أنه يحسن المؤشرات المناعية والكيميائية الحيوية ويقلل من الإجهاد التأكسدي لدى الحيوانات المعرضة للكادميوم.(13)

من خلال دراسة تأثيرات كلوريد الكادميوم على الهرمونات التناسلية والخصوبة الهامة، وتحديداً الهرمون المنبه للجريب (FSH) والهرمون اللوتيني (LH) والبروجسترون، تسعى هذه الدراسة إلى تقييم التأثيرات السامة للكادميوم على الجهاز الهرموني وتوضيح دوره في التسبب في اضطرابات هرمونية قد تضعف الوظيفة التناسلية والخصوبة. بالإضافة إلى ذلك، تهدف الدراسة إلى توضيح الآثار الضارة لكلوريد الكادميوم على الجنين أثناء الحمل، مع التركيز على اختلال التوازن الهرموني لدى الأم، وقدرة الكادميوم على اختراق المشيمة، وما يترتب على ذلك من آثار سلبية على نمو الجنين وتطوره الطبيعي، مثل زيادة خطر تسمم الجنين، وتأخر النمو، واضطرابات النمو. علاوة على ذلك، تم بحث التأثير المُحتمل لمستخلص الفجل البري في تخفيف الآثار السامة للكادميوم.

المواد والأساليب

تحضير المواد النباتية والمستخلصات

في شهر أكتوبر، جُمعت نباتات الفجل البري من محافظة صلاح الدين. وقد قام الأستاذ المساعد الدكتور محمد عدنان هاشم بتحديد نوع النبات في مختبر النباتات بكلية التربية للعلوم الصرفة/قسم علوم الحياة، قبل تجفيفه. ثم نُظفت عينات النبات بماء مُرشح لضمان إزالة جميع الشوائب والحصول على مادة نقية خالية من التلوث. تُرِكت الأوراق والسيقان لتجف في الهواء بدرجة حرارة الغرفة قبل تخزينها في عبوات معقمة ومظلمة ومحكمة الإغلاق لحين إجراء عملية الاستخلاص. جُففت الأوراق والسيقان أولاً، ثم سُحقت وطُحنت بعناية في مطحنة كهربائية لاستخلاص المادة. بعد ذلك، وُزنت 500 ملغ من مسحوق الأوراق والسيقان بدقة، ثم نُقعت في دورق زجاجي سعة 1 لتر مع 250 مل من الماء المقطر. ولضمان تكسير الخلايا وامتزاج مسحوق النبات بالماء تمامًا، وُضع الدورق على محرك مغناطيسي ورُجّ لمدة ساعة بسرعة 70 دورة في الدقيقة. بعد ذلك، غُطّيَت فوهة القارورة بغطاء أسود غير شفاف، وأُحكم إغلاقها بسدادة بلاستيكية لمنع التلوث. ثم وُضِعَت القارورة في حاضنة هزازة لمدة يوم كامل. وللتخلص من الرواسب الصلبة والخشنة، رُشِّحَ المزيج أولًا عبر أربع طبقات من الشاش الطبي. ثم استُخدِم ورق ترشيح واتمان رقم 10–N لعملية ترشيح ثانية.

استعدادات الحيوانات

استُخدم في هذه الدراسة ثلاثون أنثى بالغة من فئران سلالة سبريج داولي. تراوحت أوزان هذه المخلوقات بين 180 و200 غرام، وكانت 12إلى 14كانت الحيوانات تبلغ من العمر أسابيع. تم تربية الحيوانات ورعايتها في بيت الحيوانات التابع لكلية الطب البيطري بجامعة تكريت، وتم إيواؤها في

أقفاص بلاستيكية جيدة التهوية ذات أبعاد موحدة.) 46×28×13في ظل ظروف مخبرية مضبوطة، خضعت الحيوانات لفترة تأقلم مدتها أسبوع واحد قبل بدء الإجراءات التجريبية، وذلك للسماح لها بالتكيف مع الظروف البيئية الجديدة وتقليل آثار الإجهاد. خلال هذه الفترة، حُفظت الفئران في درجة حرارة محيطة تبلغ حوالي 25 درجة مئوية، مع دورة ضوئية مظلمة منتظمة مدتها 12 ساعة من الضوء و12 ساعة من الظلام، بالإضافة إلى تهوية كافية. طوال فترة التجربة، أُتيح للحيوانات الوصول الحر إلى علف المختبر القياسي المُصمم لتلبية احتياجاتها الغذائية، وإلى مياه شرب نظيفة، مما يضمن استقرار صحتها وحالتها الفسيولوجية. من أجل التزاوج، وُضعت الإناث طوال الليل مع ذكور من نفس السلالة. في صباح اليوم التالي، أثبت وجود سدادة مهبلية أو حيوانات منوية في مسحة المهبل الحمل؛ عُرف هذا اليوم بيوم الحمل صفر (GD 0). أُعطيت العلاجات التجريبية عن طريق الفم للفئران الحوامل بين اليوم الخامس والحادي عشر من الحمل.

تصميم التجربة

تم توزيع الحيوانات عشوائياً على ست مجموعات متساوية (الجدول 1)، تتكون كل منها من خمسة فئران، لضمان التجانس بين المجموعات والتحكم في التباين الفردي. وقد تم تنفيذ جميع البروتوكولات التجريبية بموجب موافقة لجنة رعاية الحيوان بجامعة تكريت في العراق (رقم 2025.17، مدونة الأخلاقيات).. تجميع الفئران التي تمت دراستها في الدراسة.

علاج	مجموعات الفئران
سيطرة	G1
الكادميوم (5 ملغم/كغم من وزن الجسم)(14)	G2
الكادميوم (10 ملغ/كغ من وزن الجسم)(14)	G3
2 مل من مستخلص الفجل البري يومياً	G4
الكادميوم (5 ملغم/كغم من وزن الجسم) و2 مل من مستخلص الفجل البري يومياً(14)	G5
الكادميوم (10 ملغم/كغم من وزن الجسم) و2 مل من مستخلص الفجل البري يوميًا(14)	G6

تحديد الجرعة الفعالة

تألفت كل مجموعة من المجموعات الخمس المستخدمة في هذه الدراسة من خمسة فئران بالغة يتراوح وزنها بين 180 و200 غرام. أُعطيَت المجموعة الأولى، التي اعتُبرت المجموعة الضابطة، 1 مل من الماء المقطر عن طريق الفم. أما المجموعات التجريبية الأربع (المجموعات 2، 3، 4، و5)، فقد أُعطيَ لها مستخلص مائي من الفجل البري (Raphanus sativus) عن طريق الفم بجرعات متدرجة: 0.5 مل/حيوان للمجموعة 2، و1 مل/حيوان للمجموعة 3، و1.5 مل/حيوان للمجموعة 4، و2 مل/حيوان للمجموعة 5. استُخدم جهاز قياس الطيف الضوئي لقياس مستويات الجلوكوز في مصل الدم بعد سحب عينات الدم من الضفيرة الوريدية خلف الحجاج بعد ساعتين من إعطاء الدواء. ولتحديد الجرعة الفعالة من الفجل البري، قُيِّم تأثير الجرعة على استجابة الجسم لمستخلص النبات باستخدام مستويات الجلوكوز في الدم كمؤشر فسيولوجي. أظهرت النتائج أن جرعة 2 مل/حيوان كانت الأكثر فعالية، إذ حققت أفضل تأثير بيولوجي مقارنةً بالجرعات الأخرى، ولم تُظهر أي سمية أو آثار جانبية واضحة. ولذلك، تم اختيار هذه الجرعة كجرعة فعالة للاستخدام في الاختبارات اللاحقة.

تشريح الحيوانات

تم تجويع الحيوانات لمدة 12 ساعة في نهاية التجربة (30 يومًا) قبل تخديرها بالكلوروفورم. وتم سحب عينات الدم عن طريق بزل القلب. ثم تم فصل المصل باستخدام جهاز الطرد المركزي، وحُفظ المصل عند درجة حرارة −18 درجة مئوية لحين إجراء التحليل الهرموني. وتم قياس مستويات هرمونات FSH وPROG وLH باستخدام مجموعات ELISA الخاصة بالفئران (®Elabscience) وفقًا لتعليمات الشركة المصنعة.

دراسة مورفولوجية للأجنة

جُمعت الأجنة لإجراء تحليل مورفولوجي شامل، تضمن قياس طول الجنين، ومظهره العام، وتمايز الرأس والأطراف. استُخدم مسطرة مدرجة لتسجيل القياسات، والتقطت صور للأجنة لتوثيقها ومقارنتها بالمجموعة الضابطة.

التحليل الإحصائي

استُخدم تحليل التباين أحادي الاتجاه واختبار المقارنة المتعددة اللاحقة لتقييم الفروق الإحصائية بين المجموعات. استُخدم برنامج GraphPad Prism الإصدار 9 لإجراء التحليلات الإحصائية والتمثيلات البيانية. واعتُبرت قيمة p أقل من 0.05 دالة إحصائيًا.

نتائج

التحليل الهرموني (FSH، LH، والبروجسترون)

أظهرت النتائج انخفاضات كبيرة في مستويات FSH و LH والبروجسترون في جميع المجموعات المعالجة بالكادميوم والوظيفة الوقائية المحتملة لمستخلص الفجل البري (الشكل 1).لوحظ انخفاض في تركيزات الهرمونات يتناسب مع الجرعة بعد التعرض للكادميوم.لم يكن هناك فرق واضح بين مجموعتي الفجل فقط والمجموعة الضابطة.تم استعادة مستويات الهرمونات إلى حد ما بعد المعالجة المشتركة بالفجل؛ لكن مستوياتها لا تزال أقل بكثير من مستويات المجموعة الضابطة.

١.مستوى هرمون FSH

سجلت المجموعة الضابطة أعلى مستويات هرمون FSH (المجموعة الأولى: 71.55 ± 10.9 نانوغرام/مل). وبالمقارنة مع المجموعة الضابطة، أدى التعرض لجرعة منخفضة من الكادميوم (المجموعة الثانية: 54 ± 4.54 نانوغرام/مل) وجرعة عالية (المجموعة الثالثة: 47 ± 6.78 نانوغرام/مل) إلى انخفاض ملحوظ في مستويات هرمون FSH يتناسب طرديًا مع الجرعة (قيمة $p < 0.05$). وقد استعادت مستويات هرمون FSH عافيتها إلى حد كبير عند إعطاء مستخلص الفجل البري (المجموعة الرابعة: 64 ± 3.91 نانوغرام/مل) وحده. كانت نتائج الإعطاء المشترك متوسطة: المجموعة G5 (مستوى منخفض من الكادميوم + الفجل) سجلت مستويات معتدلة من هرمون FSH (49 ± 6.83 نانوغرام/مل)، بينما سجلت المجموعة G6 (مستوى عالٍ من الكادميوم + الفجل) أدنى المستويات (23 ± 7.52 نانوغرام/مل)، مما يشير إلى أن التأثير الوقائي للفجل البري محدود عند الجرعات العالية من الكادميوم. (الشكل 1أ)

٢.مستويات الهرمون اللوتيني

لوحظ نمط مماثل بالنسبة لهرمون LH. كان تركيز هرمون LH أعلى ما يكون في حيوانات المجموعة الضابطة (G1: 34.5 ± 5.44 نانوغرام/مل). وبشكل متناسب مع الجرعة، أدى التعرض للكادميوم إلى انخفاض حاد في مستويات هرمون LH (G2: 26.25 ± 6.23 نانوغرام/مل؛ G3: 20.25 ± 1.25 نانوغرام/مل). في المقابل، حافظ مستخلص الفجل البري وحده (G4: 28.75 ± 5.31 نانوغرام/مل) على مستويات قريبة من المعدل الطبيعي. ووفقًا لتأثير جرعة الكادميوم العالية، انخفضت مستويات هرمون LH في المجموعات مجتمعة بشكل ملحوظ في المجموعة G6 (8.8 ± 0.14 نانوغرام/مل)، بينما حافظت عليها المجموعة G5 (24 ± 3.65 نانوغرام/مل) بشكل كبير. (الشكل 2ب)

3.مستويات البروجسترون

كان نمط البروجسترون (Prog) مماثلاً أيضاً. بلغ تركيزه أعلى مستوياته في المجموعة الضابطة (0.43 ± 1.7 :G1 نانوغرام/مل). أدت المعالجة بجرعات منخفضة وعالية من الكادميوم إلى انخفاضات ملحوظة (0.26 ± 0.72 :G2 نانوغرام/مل؛ 0.43 ± 0.52 :G3 نانوغرام/مل). بقيت مستويات البروجسترون قريبة من المعدل الطبيعي عند استخدام الفجل البري وحده (0.22 ± 1.62 :G4 نانوغرام/مل). على الرغم من أن هذا التأثير لم يكن كافياً لاستعادة مستويات الهرمون بالكامل في ظل التعرض العالي للكادميوم، إلا أن المعالجات المُجمعة خففت جزئياً من الانخفاض (G5: 1.15 ± 0.17 نانوغرام/مل؛ 0.09 ± 1.17 :G6 نانوغرام/مل)، مما يشير إلى تأثير وقائي للمستخلص. (الشكل C3)

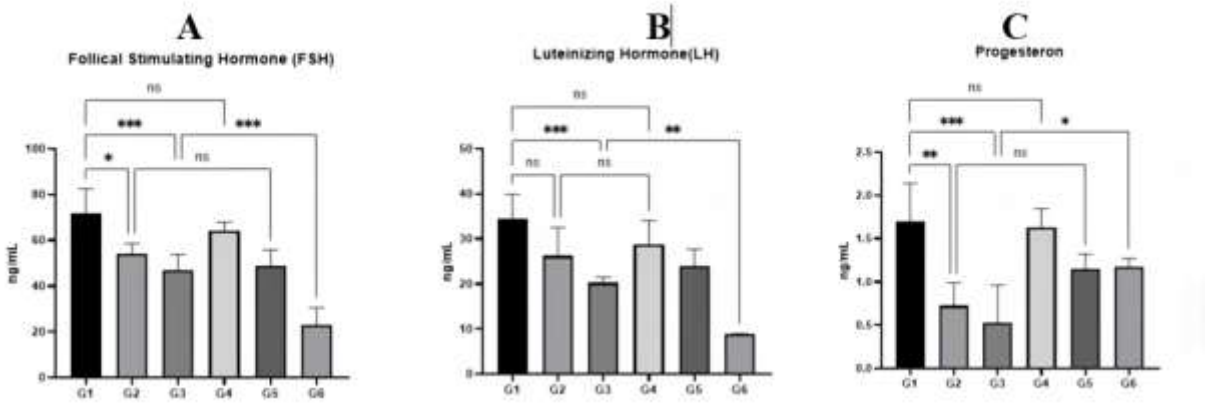

Groups Variables	G1 Control	G2 $CdCl_2$- Low dose	G3 $CdCl_2$- High dose	G4 W. Radish	G5 $CdCl_2$-Low +W. Radish	G6 $CdCl_2$-High + W. Radish
FSH (ng/mL)	71.55 ± 10.9 a	54 ± 4.54 c	47 ± 6.78 d	64 ± 3.91 b	49 ± 6.83 cd	23 ± 7.52 e
LH (ng/mL)	34.5 ± 5.44	26.25 ± 6.23 ab	20.25 ± 1.25	28.75 ± 5.31 ab	24 ± 3.65 b	8.8 ± 0.14 d

	a		c			
Progesterone (ng/mL)	1.7 ± 0.43 a	0.72 ± 0.26 bc	0.52 ± 0.43 c	1.62 ± 0.22 a	1.15 ± 0.17 b	1.17 ± 0.09 b

شكل1 تأثيرات كلوريد الكادميوم، سواءً بمفرده أو مع مستخلص الفجل البري، على هرمونات مهمة متعلقة بالتكاثر والخصوبة، بما في ذلك:

أ) الهرمون المنبه للجريب (FSH)، ب) الهرمون اللوتيني (LH)، ج) البروجسترون. تم التعبير عن النتائج كمتوسط ± الانحراف المعياري. تأثيرات الجرعات المنخفضة والعالية من كلوريد الكادميوم ($CdCl_2$)، سواء بمفرده أو بالاشتراك مع الفجل البري، على مستويات FSH و LH والبروجسترون في الدم.تُعرض البيانات كمتوسط ± انحراف معياري. وتُظهر الأحرف الصغيرة المرتفعة الفروق ذات الدلالة الإحصائية بين المجموعات ضمن نفس المتغير ($p < 0.05$).

التغيرات المورفولوجية في الأجنة

أظهرت أجنة المجموعة الضابطة (G1) نموًا طبيعيًا دون أي تشوهات مورفولوجية ملحوظة. أدى التعرض لكلوريد الكادميوم بجرعة 5 ملغم/كغم (G2) إلى تغييرات طفيفة، شملت انخفاضًا طفيفًا في طول الجنين وتأخرًا في التمايز، بينما تسببت جرعة أعلى قدرها 10 ملغم/كغم (G3) في تشوهات واضحة، مثل صغر الحجم والطول، وضعف نمو الأطراف، واضطراب تمايز الرأس، مما يؤكد وجود تأثير سام يعتمد على الجرعة. نمت الأجنة المعالجة بمستخلص الفجل البري وحده (G4) بشكل طبيعي، على غرار المجموعة الضابطة. أدى إعطاء المستخلص مع كلوريد الكادميوم بجرعتي 5 و10 ملغم/كغم (G5 وG6) إلى تحسن ملحوظ في مورفولوجيا الجنين، مما قلل من شدة التشوهات وعزز تمايز الأطراف وطول الجنين، على الرغم من أن النمو ظل أقل من مستويات المجموعة الضابطة عند جرعة الكادميوم الأعلى. تشير هذه النتائج إلى أن سمية كلوريد الكادميوم للأجنة تعتمد على الجرعة، في حين أن جرعة 2 ملغ من مستخلص الفجل البري لها تأثير وقائي، حيث تخفف من السمية التطورية الناجمة عن الكادميوم، مع فعالية جزئية عند التعرض لمستويات أعلى من الكادميوم.

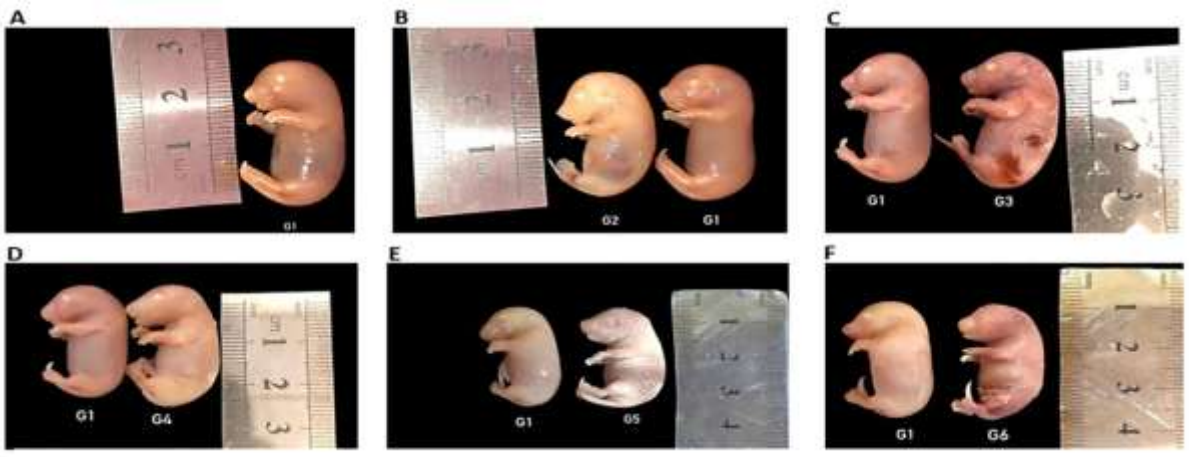

شكل2مقارنة طول وشكل الأجنة في المجموعات G2-G6 مع المجموعة G1. أ) منظر جانبي لجنين فأر ضابط من المجموعة G1. ب) منظر جانبي لجنين مُعالج بجرعة علاجية من كلوريد الكادميوم مقدارها 5 ملغم/كغم من وزن الجسم من المجموعة G2، إلى جانب جنين من المجموعة G1. ج) أجنة فئران من المجموعة الضابطة (G1) وجنين مُعالج بجرعة علاجية من كلوريد الكادميوم مقدارها 10 ملغم/كغم من وزن الجسم (G3). د) جنين فأر ضابط (G1) وجنين مُعالج بجرعة علاجية من مستخلص الفجل البري فقط مقدارها 2 ملغم (G4). هـ) جنين ضابط وجنين مُعالج بجرعة علاجية من كلوريد الكادميوم مقدارها 5 ملغم/كغم من وزن الجسم، بالإضافة إلى 2 ملغم من مستخلص الفجل البري. F) جنين ضابط وجنين معالج بجرعة علاجية من كلوريد الكادميوم بجرعة 10 ملغم/كغم من وزن الجسم والفجل البري 2 ملغم.

مناقشة

يُعرف الكادميوم بعمر نصف طويل يتراوح بين 25 و30 عامًا، مما يجعله يتراكم في جسم الإنسان، ويزيد من خطره على الصحة على المدى الطويل. ويؤدي تراكم الكادميوم في الكبد والكليتين إلى تحفيز إنتاج الميثالوثيونين، الذي يتحكم في المعادن الحيوية مثل النحاس والزنك، ويحمي الخلايا من الآثار الضارة.(15)تؤكد العديد من الدراسات دور الكادميوم في الأمراض المزمنة واحتمالية الإصابة بالسرطان، وذلك من خلال إثبات قدرته على التسبب في الإجهاد التأكسدي واختلال وظائف الخلايا. كما أن التركيز على آثار الكادميوم على الأجنة يلفت الانتباه إلى المخاطر التي يشكلها التعرض للمعادن الثقيلة على البيئة وصحة الإنسان.(16)مع ذلك، يمكن للمواد النباتية النشطة فسيولوجيًا أن تُخفف من آثار الكادميوم من خلال تحسين توازن مضادات الأكسدة وتقليل تلف الخلايا. ويُعدّ الحدّ من تلوث البيئة بالكادميوم عبر طرق مثل المعالجة النباتية أو المعالجة الميكروبية أمرًا بالغ الأهمية، بالإضافة إلى الحماية البيولوجية. ومن خلال تطبيق هذه التدابير البيئية، يقلّ تراكم الكادميوم في الغذاء والماء، مما يحمي الناس من التعرّض طويل الأمد.(17).

تُظهر نتائج هذه الدراسة أن التعرض لكلوريد الكادميوم له تأثير كبير على الجهاز التناسلي، حيث يُسبب تثبيطًا متناسبًا مع الجرعة لهرمونات التكاثر FSH و LH والبروجسترون. تشير هذه النتيجة إلى أن الكادميوم قد يُؤثر على وظائف الغدد الصماء، مما قد يُشكل مخاطر صحية على القدرة الإنجابية. تتوافق هذه النتائج مع أبحاث حديثة تُبين أن الكادميوم يُثبط إفراز هرمونات التكاثر عن طريق تغيير محور الغدة النخامية-الوطائية-المبيضية.(18؛ 19)وعلى وجه الخصوص، يتوافق الانخفاض الملحوظ في هرمون FSH وهرمون LH مع النتائج السابقة التي تشير إلى أن خلايا الغدد التناسلية في الغدة النخامية تتأثر بشكل مباشر بالكادميوم، مما يؤدي إلى انخفاض إنتاج الهرمونات التناسلية بسبب الإجهاد التأكسدي وتغير مسارات الإشارات داخل

الخلايا(20)علاوة على ذلك، فإن الأبحاث التي تُظهر أن التعرض للكادميوم يثبط تكوين الستيرويدات المبيضية ويضر بوظيفة الجسم الأصفر، خاصة أثناء الحمل، تتوافق مع الانخفاض الكبير في مستويات البروجسترون.(21).

بالإضافة إلى ذلك، تسبب الكادميومتأخر جزئي في تمايز الأطراف والرأس، بالإضافة إلى قصر الجسم، بشكل متناسب مع الجرعة .قيّمت العديد من الدراسات التأثيرات المخففة للنباتات الطبية على الخصائص السامة للكادميوم .على سبيل المثال، تم الإبلاغ عن التأثيرات المفيدة للشاي الأخضر الصالح للأكل) كاميليا سينينسيس (ضد سمية الكادميوم على هرمون FSH وهرمون LH في إناث الجرذان.(22).

أظهرنا هنا، ولأول مرة، التأثير المُحسِّن لمستخلص الفجل البري الصالح للأكل على التأثير السام للكادميوم على نمو الجنين وتمايز بنية الجسم، بالإضافة إلى مستويات الهرمونات. أظهرت الأجنة من المجموعة التي عولجت بمستخلص الفجل البري فقط (G4) نموًا شبه طبيعي، مما يشير إلى عدم وجود آثار ضارة للمستخلص، وهو ما يتوافق مع الدراسات الحديثة التي تُبرز سلامة المستخلصات النباتية الغنية بمضادات الأكسدة أثناء الحمل.(23)أدى تناول مستخلص الفجل البري مع كلوريد الكادميوم (G5 و G6) إلى تحسينات ملحوظة في طول وحجم الجنين، وتمايز أفضل للأطراف، وانخفاض في شدة التشوهات، مما يشير إلى تأثير وقائي جزئي للمستخلص عند جرعات الكادميوم العالية، وهو ما يتوافق مع نتائج رينوغاديفي وبرابو (2010).(24)وألمير وآخرون (2021)(23)وفقًا لنتائج تومسون وبانيجان (2008)، أظهرت الأجنة من المجموعة الضابطة (G1) نموًا طبيعيًا. وفقًا لساموييل وآخرون (2011)(25)أدى التعرض لجرعة معتدلة من كلوريد الكادميوم (المجموعة الثانية؛ 5 ملغم/كغم من وزن الجسم) إلى تأخيرات طفيفة في تمايز بعض التراكيب وانخفاض طفيف في طول الجنين، مما يشير إلى سمية متوسطة. في المقابل، أظهرت الأجنة المعرضة لجرعة أعلى (المجموعة الثالثة؛ 10 ملغم/كغم من وزن الجسم) تغيرات مورفولوجية أكثر وضوحًا، مثل انحناء غير طبيعي للجسم، وضعف في نمو الأطراف، واضطراب في تمايز الرأس، وهو ما يتوافق مع التأثيرات المشوهة للأجنة للكادميوم التي تعتمد على الجرعة، والتي وثقها هينسون وشيدريس (2004).(26)وباكسي وآخرون (1997)(27).

لذلك، أدى العلاج المشترك بالعامل النباتي إلى استعادة جزئية لمستويات الهرمونات، وهو ما يتوافق مع الأبحاث الجديدة التي تُظهر أن المركبات النباتية الغنية بمضادات الأكسدة يمكن أن تخفف من سمية الغدد الصماء الناتجة عن الكادميوم عن طريق خفض الإجهاد التأكسدي والحفاظ على سلامة أنسجة الغدد الصماء.(23)وهذا يوضح الوظيفة الوقائية الجزئية للفجل البري، خاصة عند الجرعات المنخفضة من الكادميوم، ويثير إمكانية استخدام المواد الكيميائية النباتية الطبيعية كتكتيك للحد من السمية.

تؤكد الدراسة أيضًا على ضرورة إجراء المزيد من الأبحاث لتحديد مستويات آمنة من الكادميوم وتقييم فعالية المستخلصات النباتية المختلفة. وتشير النتائج إلى أن مستخلص الفجل البري يُعد خيارًا مناسبًا للتخفيف من الآثار الضارة للكادميوم على التكاثر والأجنة. ولحماية الصحة العامة والحد من

الآثار الضارة للمعادن الثقيلة كالكادميوم على الإنسان والنظم البيئية، تختتم هذه الدراسة بتسليط الضوء على أهمية الجمع بين الاستراتيجيات الوقائية البيئية والطبيعية.

بشكل عام، تؤكد هذه النتائج أن التأثيرات السامة للأجنة والمشوهة للكادميوم تعتمد على الجرعة، في حين أن مستخلص الفجل البري يوفر حماية جزئية ضد السمية التطورية الناجمة عن الكادميوم.

مراجع

References

1. Heavy metal pollution in the environment and their . Briffa, J, Sinagra, E and Blundell, R. 9, 2020, Heliyon, Vol. 6, p. e04691.
2. Impact of heavy metals on the environment and human health: Novel therapeutic insights to counter the toxicity. Mitra, S, et al., et al. 2022, Journal of King Saud University–Science, Vol. 34.
3. Cadmium in biological samples and site-specific cancer risk and mortality: a systematic review of original articles and meta-analyses. Fanfani, A., Papini, S., Bortolotti, E., et al.,. 2024, Cancer Epidemiol., Vol. 92, p. 102550.
4. Assessment of phytoremediation potential of native plant species naturally growing in heavy metal-polluted industrial soils. Naz, R., Khan, M. S., Hafeez, A., et al. 2022, Brazilian Journal of Biology (Revista Brasileira de Biologia), Vol. 84, p. e264473.
5. Mechanisms of cadmium neurotoxicity. Arruebarrena, M. A., Hawe, C. T., Lee, Y. M., et al. 2023, International Journal of Molecular Sciences, Vol. 24.

6. Mechanism of cadmium-induced nephrotoxicity. Bautista, C. J., Arango, N., Plata, C., et al. 2024, Toxicology, Vol. 502, p. 153726.
7. Cadmium sulfide nanoparticles: Preparation, characterization, and biomedical applications. Ghasempour, A., Dehghan, H., Ataee, M., et al. 2023, Molecules, Vol. 28.
8. Neurotoxic effects of heavy metal pollutants in the environment: Focusing on epigenetic mechanisms. Yu, G., Wu, L., Su, Q., et al. 2024, Environmental Pollution, Vol. 345, p. 123563.
9. Cadmium neurotoxicity and therapeutic strategies. Wen, S., & Wang, L. 2024, Journal of Biochemical and Molecular Toxicology,, Vol. 38, p. e23670.
10. The role of nuclear factor erythroid 2-related factor 2 (NRF2) in arsenic toxicity. El-Mahrouk, S. R., El-Ghiaty, M. A., & El-Kadi, A. O. S. 2025, Journal of Environmental Sciences (China), Vol. 150, pp. 632–644.
11. Inhibition sensitivity of in vitro firefly bioluminescence quantum yields to Zn(2+) and Cd(2+) concentrations in aqueous solutions. Ono, R., Saito, K., Tezuka, D., et al. 2024, Photochemistry and Photobiology.
12. Cadmium induces cytotoxicity in normal mouse renal MM55.K cells. Lee, H. J., Lee, J. H., Lee, S. M., et al. 2022, International Journal of Environmental Health Research, Vol. 32, pp. 131–140.
13. Tunisian radish (Raphanus sativus) extract prevents cadmium-induced immunotoxic and biochemical alterations in rats. Salah-Abbès, J. B., Abbès, S., Zohra, H., & Oueslati, R. 1, 2015, Journal of Immunotoxicology, Vol. 12, pp. 40–47.

14. Evaluation of the Impact of Cadmium Chloride and Lead Acetate on the Lung Tissue of Albino Female Rats by Physiological and Histological Methods. Razooqi, Q. A., Dalas, I. S., & Harz, E. M. 4, 2024, Opera Medica et Physiologica, Vol. 11, pp. 130-137.
15. Effects of cadmium pollution on human health: A narrative review. Yang, Y., Hassan, M. F., Ali, W., Zou, H., Liu, Z., & Ma, Y. 2, 2025, Atmosphere,, Vol. 16, p. 225.
16. Vitamin C and/or garlic can antagonize the toxic effects of cadmium on growth performance, hematological, and immunological parameters of growing Japanese quail. Dosoky, W. M., Farag, S. A., Almuraee, A. A., Youssef, I. M., Awlya, O. F., Abusudah, W. F., … & Tellez-Isaias, G. 3, 2024, Poultry Science, , Vol. 103, p. 103457.
17. Does group living protect offspring from the toxic effects of cadmium ingestion in juvenile earwigs? Honorio, R., Heroguez, C., Rouelle, M., Beaugeard, L., Liégeois, S., Lécureuil, C., & Meunier, J. 2025, Animal Behaviour, Vol. 208, p. 123321.
18. Prenatal cadmium exposure disrupts follicle-stimulating hormone signaling and reproductive function. Lu, Y., Zhang, X., & Chen, L. 4, 2023, Reproduction, Vol. 166, pp. 271–284.
19. Cadmium as an endocrine disruptor affecting female reproductive hormones. Zhang, H., Liu, J., & Wang, X. 2021, Environmental Toxicology and Pharmacology, Vol. 82, p. 103553.
20. Cadmium-induced oxidative stress impairs pituitary gonadotropin secretion in rats. Li, R., Zhao, L., & Sun, Q. 2022, Ecotoxicology and Environmental Safety,, Vol. 230, p. 113146.

21. Disruption of ovarian steroidogenesis following cadmium exposure during pregnancy. Wang, Y., Chen, J., & Zhou, Z. 2020, Journal of Hazardous Materials, Vol. 399, p. 123067.

22. The impact of green tea (Camellia sinensis) on the amount of gonadotropin hormones (LH, FSH) in immature female rats poisoned with cadmium chloride. Mahmood, B., Mokhtar, M. and Esfandiar, S.,. 1, 2015, Biomedical and Pharmacology Journal,, Vol. 8, pp. pp.261-268.

23. Protective effects of plant antioxidants against cadmium-induced reproductive toxicity. Almeer, R. S., Kassab, R. B., & Abdel-Gaber, R. 2021, Biological Trace Element Research,, Vol. 199, pp. 2569–2581.

24. Cadmium-induced developmental toxicity and the protective effect of plant-derived antioxidants in rats. Renugadevi, J., & Prabu, S. M. 2, 2010, Experimental and Toxicologic Pathology, Vol. 62, pp. 171–181.

25. Gestational exposure to cadmium and its effect on fetal development in rats. Samuel, J. B., Stanley, J. A., Princess, R. A., Shanthi, P., & Sebastian, M. S. 3, 2011, Journal of Applied Toxicology, Vol. 31, pp. 243–249.

26. Endocrine disruption by cadmium, a common environmental toxicant with paradoxical effects on reproduction. Henson, M. C., & Chedrese, P. J. 5, 2004, Experimental Biology and Medicine, Vol. 229, pp. 383–392.

27. Effect of cadmium on morphology and steroidogenesis of rat ovaries. Journal of Applied. Paksy, K., Rajczy, K., Forgács, Z., Lázár, P., Bernard, A., Gáti, I., & Kaali, G. 5, 1997, Toxicology, Vol. 17, pp. 321–327.

28. Factors moderating cadmium bioavailability: Key considerations for comparing blood cadmium levels between groups. Cirovic, A., & Cirovic, A. 2024, Food and Chemical Toxicology, Vol. 191, p. 114865.

29. Vanillylacetone attenuates cadmium chloride-induced hippocampal damage and memory loss through up-regulation of nuclear factor erythroid 2-related factor 2 gene and protein expression. Al-Hashem, F. H., Bashir, S. O., Dawood, A. F., et al. 2024, Neural Regeneration Research, Vol. 19, pp. 2750–2759.

30. Cadmium induced bioaccumulation, histopathology, gene regulation in fish and its amelioration – a review. Das, S., Kar, I., & Patra, A. K. 2023, Journal of Trace Elements in Medicine and Biology, Vol. 79, p. 127202.

31. Cadmium-induced stress: A close look at the relationship between autophagy and apoptosis. Tuffour, A., Adebayiga Kosiba, A., Addai Peprah, F., et al. 2023, Toxicological Sciences,, Vol. 194, pp. 1–12.

32. Distinct phylogeographic structures of wild radish (Raphanus sativus L. var. raphanistroides Makino) in Japan. Han, Q., Higashi, H., Mitsui, Y., & Setoguchi, H. 7, 2015, PLoS ONE, Vol. 10, p. e0135132.

33. Origin, distribution, genetic diversity and breeding of radish (Raphanus sativus L.). Swaamy, K. 2023, International Journal of Development Research,, Vol. 13, pp. 61657–61673.

34. The World Checklist of Vascular Plants, a continuously updated resource for exploring global plant diversity. Govaerts, R., Nic Lughadha, E., Black, N., Turner, R., & Paton, A. 2021, Scientific Data, Vol. 8, p. 215.

35. Deciphering the nutraceutical potential of Raphanus sativus—A comprehensive overview. Manivannan, A., Kim, J., Kim, D., Lee, E., & Lee, H. 2019, Nutrients,, Vol. 11, p. 402.

36. Wild radish (Raphanus raphanistrum): Weed management guide for Australian vegetable production. Coleman, M., Kristiansen, P., Sindel, B., & Fyfe, C. 2021, University of New England.

37. Evaluation of climate change impacts on the potential distribution of wild radish in East Asia. Han, Q., Liu, Y., Jiang, H., Chen, X., & Feng, H. 18, 2023, Plants, Vol. 12, p. 3187.

م.م. يوسف محمد دكتور مبارك - الجامعة التكنولوجية، هندسة الكهروميكانيك

م.م. سلام كاظم خلف – جامعة ديالى، كلية العلوم

م.م. سفيان سمير عبدالقادر – جامعة ديالى، كلية العلوم

Research on developments and technical means for preventing and eliminating drill string sticking

S. S. Al-obaidi1[1,2], Salam K.khalf[4],Yousif Mohammed Diktor Al-Ghanimi[3]

[1] National Research Tomsk Polytechnic University, Tomsk, Russia

[2] Department of Petroleum and Mineral Geology, College of Science, Diyala University, Diyala, Iraq

[3] University of technology, College of Electromechanical Engineering, Baghdad, Iraq

[4] Department of Chemistry, College of Science, Diyala University, Diyala, Iraq

E-mail: Sofyanal-obaidi@uodiyala.edu.iq, Al-Obaidi@tpu.ru

Abstract

Relevance. The problem of drill string sticking remains one of the most serious challenges in the oil and gas industry, significantly affecting the safety and efficiency of drilling operations. This phenomenon creates considerable difficulties at all stages of well drilling, leading to increased time costs, financial losses, and the risk of emergencies. The purpose of this study is to identify and justify innovative approaches to preventing and mitigating drill string sticking. Particular attention is paid to the development and implementation of innovative technological solutions that aim to minimize risks and improve working conditions at drilling sites. Methods. The study is based on a

comprehensive analysis of existing methods and strategies for combating drill string sticking. Modern technologies and specialized technical means used to prevent and eliminate sticking are considered. Experimental data, theoretical calculations, and practical experience with various tools and materials are included [6]. **Results**. The article provides a comprehensive analysis of modern technologies and technical means used to prevent and eliminate the seizure of the drill string during the drilling of oil and gas wells. The main mechanisms of seizure occurrence are considered, and methods for their prevention and elimination are systematized. Innovative developments in the field of preventive technologies and equipment for the release of seized tools are analyzed. The results of a comparative analysis of the effectiveness of various technical solutions are presented. **Methods** of system analysis, statistical processing of field research data, comparative analysis of technical solutions, mathematical modeling of the interaction between the drill string and the well walls, as well as experimental methods for determining the rheological properties of drilling fluids, were employed in this work. The research results can be applied in oil and gas companies engaged in exploration and production drilling, in design institutes for developing technological regulations, as well as in the educational process for training oil and gas specialists.

Keywords: drill string sticking, drilling fluids, technical means, preventive technologies, sticking elimination, sticking removal.

Introduction

Drill string sticking is one of the most serious emergencies in well drilling, leading to significant economic losses and increased well construction time. According to statistics, sticking accounts for up to 15-20% of all drilling complications, which makes it important to study methods for preventing and eliminating it [1]. Current trends in the oil and gas industry are characterized by the development of increasingly complex geological conditions, which increase the risk of drill string sticking. In this regard, the development of effective technologies and technical means for preventing and eliminating sticking has become a priority for the drilling industry [10]. Considering the above, the following is proposed in this work. Objective:– Conduct a detailed analysis of existing approaches focused on predicting and eliminating drill string snagging; - Evaluate the advantages/disadvantages of existing technological solutions aimed at minimizing risks and improving working conditions at drilling sites.

Classification and mechanisms of sticking. Main types of sticking

Drill string sticking is classified according to various criteria [6].

1. Differential sticking. This occurs due to a pressure difference between the hydrostatic pressure of the drilling fluid and the formation pressure in permeable intervals.

2. Mechanical sticking is caused by narrowing of the wellbore, rock falls, and tool jamming in narrowed areas.

3. Adhesion sticking occurs when the drill string interacts with swelling clay formations [3]. Figure 1 shows drill string sticking.

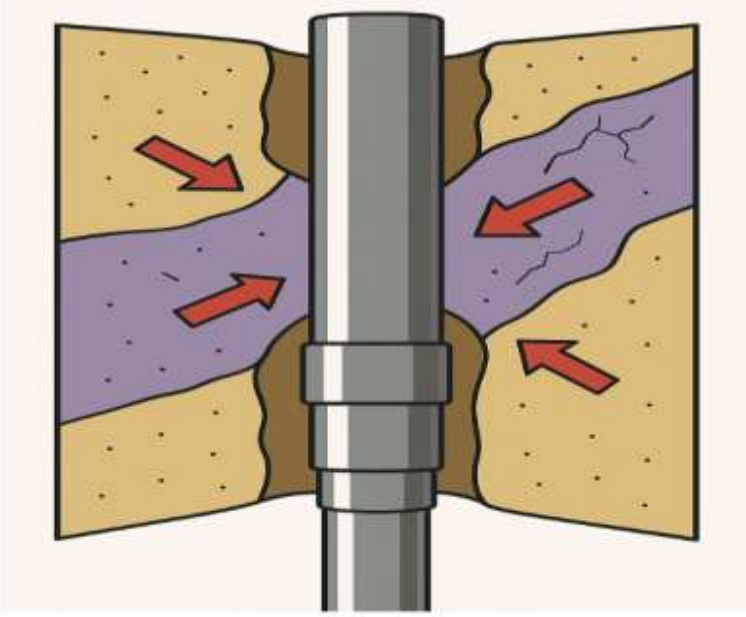

Fig 1 – Drill string sticking

Factors affecting the occurrence of sticking and preventive technologies for avoiding sticking

An analysis of the factors contributing to the occurrence of sticking allows us to identify the following main groups [8]. These include geological factors such as the lithological composition of the section, the presence of unstable rocks, and abnormally low and high formation pressures; technological factors such as drilling fluid parameters, drilling modes, the design and condition of the drill string, the quality of cementing, the condition of the wellbore, and the effectiveness of fluid cleaning systems [8]. Analysis shows [6,8] that one of the most effective methods of

preventing sticking is to optimize the properties of drilling fluids, where approaches are distinguished that focus on minimizing filtration, i.e., reducing the filtration rate to 2–4 cm^3/30 min. This reduces the thickness of the filtration crust and the risk of differential sticking. It also involves controlling rheological properties, i.e., maintaining an optimal ratio of plastic viscosity and dynamic shear stress. The latter ensures effective cleaning of the wellbore [20]. It should be noted that the use of lubricating additives, which involve introducing special lubricants into the drilling fluid, can reduce the friction coefficient between the column and the wellbore walls by 30–50%.

Pressure control technologies

Our analysis shows that managed pressure drilling (MPD) technologies allow maintaining optimal pressure differential in the wellbore–formation system, minimizing the risks of differential sticking [17]. Table 1 shows the effect of pressure control technology.

Table 1. Pressure control.

Parameter	**Traditional drilling**	**MPD technology**	(**Efficiency**)
Accuracy of maintaining bottomhole pressure	±0.5 (MPa)	±0.05 (MPa)	Increase by 10 times

Speed of response to changes	15–30 min	1–3 min	Increase by 10–15times
Reducing the risk of seizures	–	60–70%	Significant improvement

Based on the results in Table 1, we can conclude that the use of MPD technologies provides a significant improvement in pressure control accuracy and reduces the risk of sticking due to the system's high responsiveness to changes in drilling conditions [13].

Figure 2 illustrates the specifics of well pressure control technology, specifically Managed Pressure Drilling (MPD).

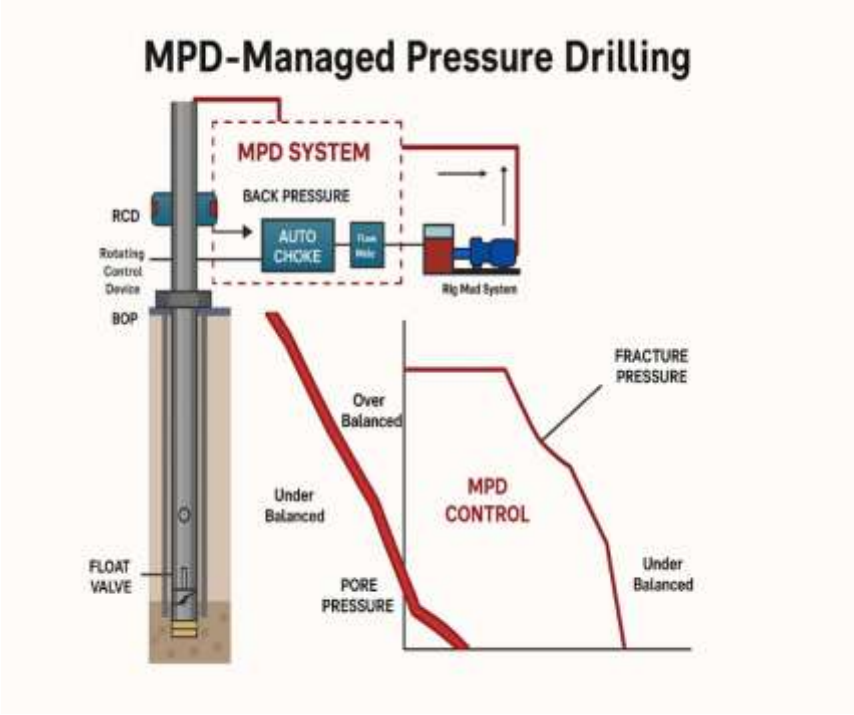

Fig 2 – Well Pressure Management Technologies (MPD – Managed Pressure Drilling)

The diagram shows an adaptive well pressure control system, whose key features are: – a closed circulation system with an automatic choke (Auto Choke) ensures precise backpressure control; – a bottomhole pressure control system maintains an optimal balance between pore pressure and hydraulic fracturing pressure; – automated control minimizes human error and increases drilling safety; – the technology is particularly effective when drilling in conditions with a narrow drilling fluid density window [16].

The results [17] indicate that the development of new types of drilling fluids is aimed at creating systems with minimal interaction with rock formations. In this regard, new-generation polymer fluids are characterized by low filtration, high inhibiting capacity, and environmental safety. Nanotechnological additives (SiO_2, Al_2O_3 nanoparticles) are promising in engineering applications, allowing the formation of an ultra-thin impermeable crust on the walls of the wellbore.

Technical means of eliminating stuck pipes

Mechanical methods remain the primary means of eliminating stuck pipes and include the use of impact devices. These mechanisms include hydraulic/mechanical impactors, which deliver an impulse to the stuck pipe with a force of up to 1000 kN.

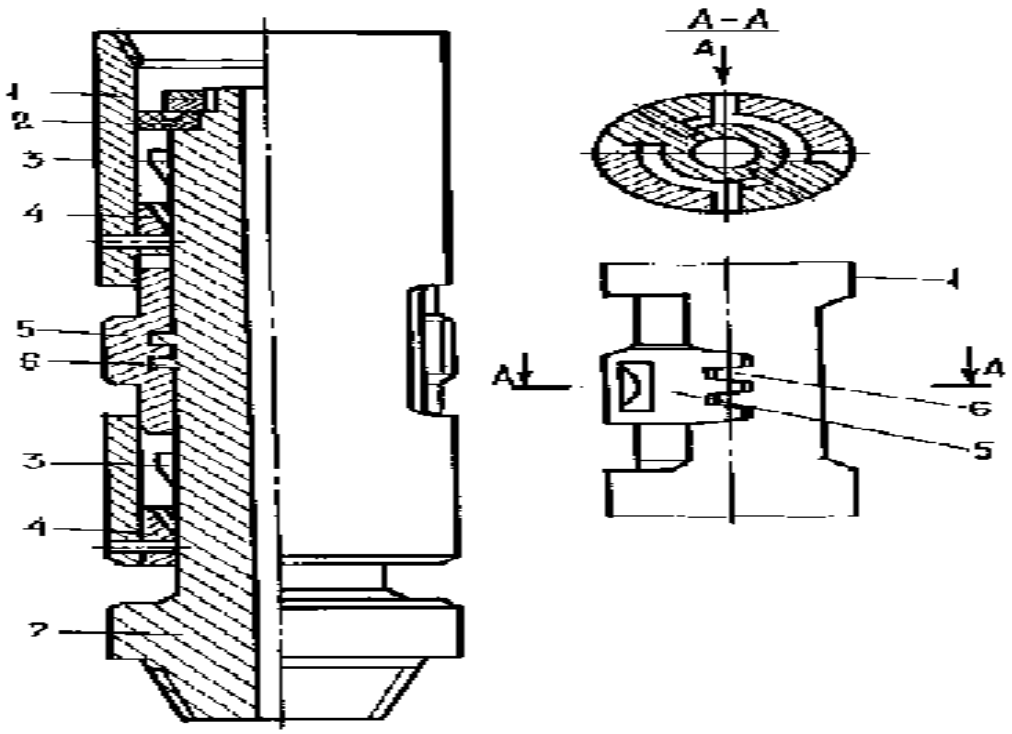

Fig 3. Device for Eliminating Stuck Pipe – ULP-190-1

1. Body 2. Piston 3. Seal 4. Spring 5. Valve 6. Guide

7. Tip / Nozzle / End cap

Chemical Methods

The use of specialized chemical reagents for the elimination of pipe sticking includes the following (Table 2):

Table 2. Use of special chemical reagents to eliminate weld spatter

Reagent type	**Mechanism of action**	**Exposure time**	**Efficiency, %**

Oil baths	Reduced friction, softened crust	6-12 hours	65-75
Acidic compounds	Dissolution of carbonate crust	2-4 hour	70-80
Surface-active substances	Change in wettability	(4-8 hours)	60-70
Combined compositions	Complex impact	(8-16 hours)	80-90

Table 2 shows that combined compositions are the most effective, providing a comprehensive effect on various sticking mechanisms, but requiring a significant amount of time to achieve results. Hydraulic release devices generate pressure pulses of up to 200 MPa, which are transmitted directly to the sticking point through the drilling fluid [10]. Electrical impulse systems are capable of generating powerful electrical discharges in the drilling fluid, creating shockwaves that destroy the sticking zone. Additionally, thermal methods focus on local heating of the sticking zone to 200-300°C, which alters the physicochemical properties of the contacting media.

Comparative analysis of technology effectiveness

Based on an analysis of statistical data on 500 cases of blowouts at various fields, a summary table of the effectiveness of elimination methods has been compiled:

Table 3. **Efficiency of elimination methods**.

Method of elimination	**Number of cases**	**Successful eliminations**	**Efficiency, %**	**Average time, hours**
Mechanical shocks	180	126	70	8-12
Chemical baths	150	105	70	12-24
Vibration methods	80	64	80	4-8
Combined methods	90	81	90	16-32

Table 3 shows that combined methods demonstrate the highest efficiency (90%), but require the most time. Vibration methods show the optimal ratio of efficiency and time required to perform operations [4].

Economic efficiency

An analysis of the economic efficiency of various technologies shows (Table 4):

Table 4. Economic efficiency.

(**Technology**)	**Implementations, thousand $**	**Снижение ущерба от**	**Payback period, months**

		прихватов, %	
MPD systems	800–1200	60–70	12–18
Preventive supplements	50–100	30–40	3–6
Modern drummers	200–300	40–50	6–9
Chemical compositions	20–50	25–35	2–4

Table 4 suggests that chemical compounds and preventive additives offer the fastest return on investment, while MPD systems provide maximum damage reduction with a longer payback period [11].

Promising areas for development include [19] the implementation of: – artificial intelligence systems for predicting sticking based on real-time data analysis. This opens up new opportunities for preventive risk management, such as early warning systems based on machine learning algorithms. They are capable of analyzing a variety of drilling parameters and predicting the probability of sticking with an accuracy of 85–90%. Automated control systems ensure the instant adjustment of drilling parameters when prerequisites for sticking are detected. Additionally, nanotechnologies are utilized in drilling fluids. This opens up fundamentally new opportunities for creating drilling fluids with unique properties.

Conclusion

The systematic study conducted in accordance with the objective of the work allows us to draw the following conclusions:

1. The most effective approach to solving the problem of sticking is a comprehensive strategy that includes preventive measures and modern technical means of elimination.

2. Pressure management technologies (MPD) reduce the risk of stuck pipes by 60–70% at a relatively high capital cost.

3. Combined methods of stuck pipe removal are most effective (up to 90%), but require a significant amount of time.

4. Vibration-based release methods demonstrate an optimal balance between effectiveness and speed of operation.

5. Promising areas for development include digital forecasting technologies, nanotechnological drilling fluids, and robotic systems.

6. The economic efficiency of preventive technologies exceeds the cost of eliminating the consequences of sticking by 3–5 times.

Further research should be aimed at developing integrated intelligent drilling process control systems with forecasting and automatic accident prevention functions [21].

REFERENCES

1. Tyuleneva T, Kabanov E, Moldazhanov M, Plotnikov E. Improving the professional risk management system for methane and coal dust explosions using a risk-based approach. E3S Web of Conferences [Internet]. 2021 Jan 1;278:01027. Available from: https://doi.org/10.1051/e3sconf/202127801027

2.Kenzhetaev Z, Nurbekova M, Togizov K, Abdraimova M, Toktaruly B. Methods for intensification of borehole uranium mining at the fields with low filtration characteristics of ores. Mining of Mineral Deposits [Internet]. 2021 Sep 1;15(3):95–101. Available from: https://doi.org/10.33271/mining15.03.095

3 .Re E.,Vi R. Optimizatsiya naklonno-napravlennogo bureniya na osnove geomekhanicheskogo modelirovaniya s ispol'zovaniem seysmicheskikh dannykh, Burenie & Neft′.2024, no. 10, pp. 50–54. doi: 10.62994/2072-4799.2024.58.84.008.

4. Dmitrievsky A. N., Eremin N. A., Chernikov A. D., and Borozdin S. O. Intelligent complication prevention systems for safe well construction. Occupational Safety in Industry . 2022, no. 6, pp. 7–13. doi: 10.24000/0409-2961-2022-6-7-13.

5. Al-Obaidi, S. S., Evan, D., Kharlamov, S. N. (2024). Progress on clay swelling inhibitors: a comprehensive review. Bulletin of the Tomsk Polytechnic University Geo Assets Engineering, 335(10), 146–166. https://doi.org/10.18799/24131830/2024/10/4868

6. Al-Obaidi S.S, Kharlamov S.N. Analysis of pipe sticking at well drilling in the South Iraqi limestone and sandstone reservoirs. Bulletin of the Tomsk Polytechnic University. Geo Assets

Engineering [Internet]. 2024;335(8):91–111. Available from: https://doi.org/10.18799/24131830/2024/8/4703

7. Ерменов С. М., Эфендиев Г. М., Садырбаева А. С., Жантасов М. К., Байботаева С. Е. Буровые растворы на основе отходов для бурения скважин в осложненных условиях, КазУТБ .2024, vol. 4, no. 25. doi: 10.58805/kazutb.v.4.25-457.

8. Yavorskiy M. A., Romanova N. V., Spiridonova I. A. Problems and Trends of Development Technical and Forensic Support of the Preliminary Investigation.Vestnik Samarskogo Iuridicheskogo Instituta .2023, no. 2(53), pp. 101–107. doi: 10.37523/sui.2023.53.2.014.

9. Kharlamov S. N., Dzhanhorbani M. Optimization of Rheological Properties of Drilling Fluid Enhancing Transport and Cleaning of Horizontal Wells from Cuttings. Bulletin of the Tomsk Polytechnic University Geo Assets Engineering .2022, vol. 333, no. 8, pp. 91–108. doi: 10.18799/24131830/2022/8/3751.

10. Al-Obaidi S. S., Evan D., Kharlamov S. N. Progress on clay swelling inhibitors.a comprehensive review. Bulletin of the Tomsk Polytechnic University Geo Assets Engineering. 2024, vol. 335, no. 10, pp. 146–166. doi: 10.18799/24131830/2024/10/4868 .

11.Mamedov S. R. N. M., Dzhaniev E. D. E. Application of Modern Navigation Systems in Drilling of Inclined and Horizontal Wells.Pahtei - Proceedings of Azerbaijan High Technical Educational Institutions .2023, vol. 34, no. 11, pp. 150–157. doi: 10.36962/Pahtei34112023-150.

12. Ad Sh., Vg V., Vg K. Practical experience in maintaining the stability of clay formations. the example of drilling lateral wellbores in Western Siberia. Burenie & Neft′. 2024, no. 11, pp. 30–34. doi: 10.62994/2072-4799.2024.48.43.010.

13. Selivanov N. S., Komarov S. A., Chudinova I. V. Analysis of methods to prevent sticking of the drill string at the Kharasavey Gas-Condensate Field. Advances In Current Natural Sciences (Успехи Современного Естествознания). 2022, no. 8, pp. 133–138. doi: 10.17513/Use.37879.

14. Kuzmin V. N. Practical recommendations for the prevention and elimination of geological and technological complications during well drilling. Neftânaâ Provinciâ. 2020, no. 1(21). doi: 10.25689/np.2020.1.44-55.

15. Akhymbayeva BS. Analysis of the use of hydraulic shock technology in drilling of hard rocks. Neft I Gaz [Internet]. 2024 Oct 30;143(5):132–42. Available from: https://doi.org/10.37878/2708-0080/2024-5.10

16. Salnikova O. L., Chernykh I. A., Martyushev D. A., Ponomareva I. N. Features of determining filtration parameters of complex carbonate reservoirs at their operation by horizontal wells. Bulletin of the Tomsk Polytechnic University Geo Assets Engineering. 2023, vol. 334, no. 5, pp. 138–147. doi: 10.18799/24131830/2023/5/3970.

17 Popov S. V., Sadykov R. M., Smirnov I. A. New approaches to drilling fluids at the wells drilling operation in Western Siberia. Burenie & Neft′. 2024, no. 5, pp. 18–22. doi: 10.62994/2072-4799.2024.66.35.003.

18. Regotunov A. S. Methodological approach to the evaluation and selection of technical solutions for adapting drilling operations to changing conditions in quarries. Problemy Nedropol′zovaniâ. 2024, no. 4(39). doi: 10.25635/2313-1586.2023.04.089.

19. ON B., SA K. Elimination of sticking during well drilling. Upravlenie Tehnosferoj. 2023, vol. 6, no. 1. doi: 10.34828/udsu.2023.87.80.002.

20. Sulavko A. E., Vasilyev V. I., Klinovenko S. A., Lozhnikov P. S., Suvirin G. A., Guzaírov M. B. Review of Neural Network Models for Solving the Problems of Predicting Emergency Situations and Ensuring the Safe Operation of Oil and Gas Wells. Modelirovanie.Optimizaciâ i Informacionnye Tehnologii. 2024, vol. 12, no. 1(44), p. 17. doi: 10.26102/2310-6018/2024.44.1.017

21. Gabitov S. I., Gotsulyak A. S., Chebyshev I. S., Mukhamadiev R. V. Support of drilling high-technological wells based on the integration of geomechanics and geosteering. Oil and Gas Business. 2020, vol. 18, no. 2., pp. 15–23. doi: 10.17122/Ngdelo-2020-2-15-23.

Effect of ZNO and Vitamin C Supplementation on IFN-a Serum Levels in X-ray-Irradiated Female Rats: A Dose-Response Study

Zainab Mohammed Madfoon[1], Doaa Falah Razzaq[2], Naeema Hadi Ali[3], Noor A.Al-quraishi[4].

College of Science Biology department[1], Department of Physics- Faculty of Science - University of Kufa[1,2,3,4]

zainabm.algeubori@uokufa.edu.iq[1],doaaf.aldabbag@uokufa.edu.iq[2],

Naemah.abbood@uokufa.edu.iq[3], noora.alqurashi@uokufa.edu.iq[4]

Abstract:

Ionizing radiation, consisting of X-rays, interacts with the immune system in complicated ways, impacting numerous cells through a mechanism related to oxidative stress. The purpose of the current study was to examine the potential therapeutic impact of ZnO-nano and vitamin C supplementation on immunity-toxicity caused by X-ray irradiation in female rats. The experiment was conducted using five groups, each consisting of 6 female rats. Group 1: X-ray non-irradiated control female rats (G1), while groups 2 and 3 received a single dose of 4 Gy (G2, G4) and 6 Gy (G3, G5) X-ray radiation using a linear accelerator. The animals in groups 4 and 5 (G4, G5) were treated with ZnO-nano and vitamin C supplementation at 0.01 mg/kg/day (5 mg) of ZnO-nano and 0.4 mg/kg/day (180 mg) of vitamin C for 14 consecutive days, starting the day after irradiation. The results revealed that exposing rats to X-ray irradiation caused a decrease in interferon-alpha (IFN-a) levels in rats exposed to 4 Gy (G2) and 6 Gy (G3) of radiation. It also

shows that both zinc oxide nanomaterials (ZnO-nano) and Vitamin C supplementation can provide radioprotective effects, and they work synergistically. Vitamin c Supplementation has been proven to protect against radiation-induced harm, while ZnO-nano can reduce oxidative stress and inflammation related to radiation. Combining dietary ZnO-nano with Vitamin C supplementation should undoubtedly enhance these protective effects, such as regulating IFN-a, which is involved in the immune response radiation. It can be concluded that ZnO-nano and Vitamin C supplementation should undoubtedly enhance protective effects, such as regulating IFN-a, which is involved in the immune response to radiation by combating free radical generation and boosting antioxidant defenses mechanisms.

Keywords:

ZNO, Vitamin C Supplementation, IFN-a, X-ray, Female Rats.

Introduction

Numerous functions of cytokines are especially pertinent to research on radiation. Proinflammatory cytokines are the main components of immediate early gene responses and can be rapidly activated following tissue irradiation. They both produce loose radicals, such as reactive oxygen and nitrogen species (ROS/RNS), which is how they converge with the effects of ionizing radiation. "Self" molecules secreted or released from cells after irradiation feed the identical paradigm by way of signaling for ROS and cytokine production. As a result,

multilayered feedback manage circuits can be generated that perpetuate the radiation tissue damage reaction. The seasoned-inflammatory phase lasts until situations that are thought to be demanding on host integrity are eliminated. Antioxidant, anti-inflammatory cytokines then act to repair homeostasis. (Nasiri, 2023)

A glycoprotein called IFN-a is produced by peripheral blood B-lymphocytes. It contains antiviral and antiproliferative properties and, for this reason anti-tumor effect. It has modulating results on the immunological system. (Salkowski et al., 1995) (Dawood, 2021). IFN is usually well tolerated and results in long-lasting complete cytogenetic responses as a treatment for hematological relapse following BMT (Lee Chung, 2017).

Nanotechnology has been advanced in lots of areas over the past a long time, one of the maximum important regions of this technology is nanomaterial area, which performs a vital position in biomedical applications (Ramos, Cruz, Tovani, & Ciancaglini, 2017). Zinc oxide nanoparticles (ZnO-nano) are highly utilized materials in biomedical applications due to their ability to penetrate barriers and target cells effectively in various dis Zinc oxide nanoparticles (ZnO-nano) are highly utilized materials in biomedical applications due to their ability to penetrate barriers and target cells effectively in various diseases (Sharma, 2019) .

Vitamin C Supplementation is a water-soluble compound used as widely as possible to consist of beauty, pharm cortical, and agricultural fields because of its biological antioxidant properties (Pehlivan, 2017) .

Early biochemical modifications, which occur during radiation risk or shortly after, had been notion to be answerable for most of the results of ionizing radiation in mammalian cells. The present work was carried out and devoted for studying the Zinc oxide nanoparticles (ZnO-nano) are highly utilized materials in biomedical applications due to their ability to penetrate barriers and target cells effectively in various diseases..ZnO-nano's effectiveness in reversing irradiation-induced changes in IFN-a levels. Furthermore, ZnO nanoparticles were prepared at the nanoscale for oral administration to female rats (Ali, Sari, Nowruzi, & Porzani, 2024).

Material & Methods

Animals

Inbred of female rats (1–2 weeks old, one 150 –157 g) procured from the animal breeding colony of the Faculty of Science – University of Kufa, Najaf, Iraq were acclimatized beneath preferred laboratory conditions for 1 week prior to the experiment. Animals were housed in polycarbonic ate cages and maintained at room temperature below stand arid laboratory situations. Animals have been stored on everyday weight loss program and water advert libitum. This take a look at turned into completed after the approval of Institutional Ethics Committee (approval no. 17569).

Irradiation of female rats

Female rats have been housed in Perspex containers for the irradiation procedure. A total of 30 rats had been exposed to complete-frame irradiation using X-rays. Of these, 12 female rats obtained an excessive dose of four Gy, whilst another 12 female rats obtained a dose of 6Gy. The

tactics took place at Amal Alhayat Hospital in Najaf and Alamal National Hospital for Cancer Management in Baghdad, the use of a linear accelerator (LINAC). The 4Gy organization's irradiation dose fee was three Gy/min, while the 6Gy group's was five Gy/min. Each female rats become uncovered to irradiation for 1.2mins.

ZnO-nano and Vitamin C Supplementation Treatment

Sky Spring Nanotechnology in Texas, USA, supplied the ZnO nano (white nanopowder, product properties: D50 10-30 nm, SSA 20-30 m^2/g, product number: 8410DL, product properties: purity). 99.8%). Vitamin C supplement (meals supplement with sweeteners, lemon-flavored, 180 mg per tablet) was changed to be purchased from Mer Avit; Merpharmagmbh Germany. An aggregate of five mg of ZnO-nano debris and one hundred eighty mg of Vitamin C supplementation was dissolved in deionized water at a volume of 1 L, and mixed using a magnetic stirrer (Hotplate Stirrer, Lab Tec, Italy) for 15 minutes at a stirring speed of 7 rpm. The rats have been administered this combination each day through oral gavage at doses of 0.01 mg/kg/day (5 mg) of ZnO-nano and 0.4 mg/kg/day (one hundred eighty mg) of Vitamin C Supplementation for 14 consecutive days. The doses of ZnO-nano and Vitamin C supplementation were administered to the irradiated rats 24 hours after irradiation and were below the median lethal dose (LD50 > 5×10^3 mg/kg), with no signs or symptoms of toxicity observed (SAINI, 2020).

.

Experimental Design

(1L) for 14 days. Group three (G_3, n All female rats were divided into five groups (n = 5). Group 1 (G1, n = 6) served as the control group. Group 2 (G2, n = 6) consisted of female rats that were irradiated with a high dose of 4 Gy for whole-body irradiation and received daily supplementation of ZnO-nano and Vitamin C. 6) Additionally, this group consisted of female rats that were irradiated with a single dose of four Gy and received the same daily doses of ZnO-nano and Vitamin C for 14 days. Group four (G4, n = 6) included protected female rats that were irradiated with a high single dose of 6 Gy for whole-body irradiation. Finally, Group five (G5, n = 6) was produced from female rats that had been irradiated with a single excessive dose of 6 Gy and received daily doses of ZnO-nano and Vitamin C supplementation for 14 days, as shown in Fig(1).

Fig (1). Show female rats that had been irradiated with a high unmarried dose stage of four Gy and 6Gy for complete-body publicity the use of X-rays from a linear accelerator (LINAC).

Preparation of Samples

All female rats in the experimental groups have been injected with ketamine and xylazine at doses of 90 mg/kg and 10 mg/kg, respectively, as recommended in the study by Kumar and Clover on the intraperitoneal co-management of low-dose urethane with xylazine and ketamine for prolonged surgical anesthesia in female rats (Kumar & Clover, 2015) .These marketers have been

mixed with low-dose urethane to facilitate prolonged surgical anesthesia throughout the test. After collecting the blood, allow it to clot undisturbed at room temperature for about 15 minutes. Remove the clot using a centrifuge set at 2,000 rpm for 15 minutes. If any precipitates appear during storage, the sample must be centrifuged again.

Immunological Investigation of Interferon-alpha (INF-α): TNF-α levels in serum from female rats were measured using the Rat Interferon Alpha (INF-α) ELISA Kit from SunLong Biotech Co., LTD (Hanley & Haydon, 1998).

Statistical Analysis

Statistical comparisons of the data were performed using the SPSS software. The results were analyzed with ANOVA followed by post hoc comparisons using Tukey's multiple comparisons test. The statistical values are presented as mean ± SD. Adjusted P values were set at $P < .05$.

Results & Discussion

Results

Reduction in cytokine INF-alpha levels due to radiation exposure was observed in full-body female rats (G2, G3, and G5) irradiated with X-ray at 4 Gy and 6 Gy, with significant decreases in INF-alpha levels in G5 compared to controls (Table 1 & 2). Oral supplementation with ZnO-nano and Vitamin C improved inflammatory factors considerably compared to the irradiated

group, but their activity and levels still differed significantly from the control, as shown in table (2) and Fig (2).

Presents the adjusted significant P value of INF-a levels in serum female rats set at (P= 0.0347< .05*) for (G4) (Dose 4Gy + ZnO-NPs and Vit.C) compared to the control (G1), and also shows that the adjusted P values are (ns) for INF-a levels in serum female rats groups (G2, G3, & G5) compared to the control (G1), as shown in Table (2) and Fig. (2).

Table 1: Mean ± SD are shown for Control (G1), Dose 4 Gy (G2), Dose 6 Gy (G3), Dose 4 Gy + Nano-ZnO and Vit-C (G4), and Dose 6 Gy + Nano-ZnO and Vit-C (G5).

Groups	**Mean ± SD**
Control (G_1)	7.79± 4.98
Dose 4G(G_2)	6.33 ± 2.49
Dose 6G(G_3)	3.66 ± 0.9
Dose 4G + Nano Zn and Vit C(G_4)	2.85 ± 1.01
Dose 6G + Nano Zn and Vit C(G_5)	5.05 ± 2.22

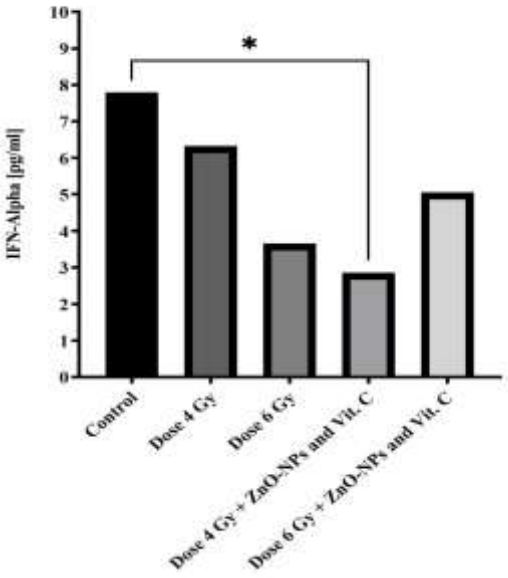

Fig(2): Shows the effect of ZnO-nano and Vitamin C supplementation on IFN-α levels in serum of female rats across various groups. Results are expressed as Mean ± SD (n = 5). P = 0.0347< .05*for (G4) (Dose 4Gy + ZnO-NPs and Vit.C) compared to control (G1). The adjusted P values are non-significant (ns) for INF-α levels in serum across groups (G2, G3, G5) compared to control (G1).

Table 2: Presents the adjusted P value of INF-alpha levels in serum of female rats set at (P < .05*), for groups G1, G2, G3, G4, and G5. The results show significance for the following comparisons: G1 vs G2 (ns), G1 vs G3 (ns), G1 vs G5 (ns), and a highly significant difference between G1 and G4 at (P ≤) .05).

Tukey's multiple comparisons test	**Summary**	**Adjusted P Value**
Control vs. Dose 4 Gy	ns	0.8851
Control vs. Dose 6 Gy	ns	0.1006
Control vs. Dose 4 Gy + ZnO-NPs and Vit. C	*	0.0347
Control vs. Dose 6 Gy + ZnO-NPs and Vit. C	ns	0.4382
Dose 4 Gy vs. Dose 6 Gy	ns	0.4151
Dose 4 Gy vs. Dose 4 Gy + ZnO-NPs and Vit. C	ns	0.1803
Dose 4 Gy vs. Dose 6 Gy + ZnO-NPs and Vit. C	ns	0.9150
Dose 6 Gy vs. Dose 4 Gy + ZnO-NPs and Vit. C	ns	0.9832
Dose 6 Gy vs. Dose 6 Gy + ZnO-NPs and Vit. C	ns	0.8843
Dose 4 Gy + ZnO-NPs and Vit. C vs. Dose 6 Gy + ZnO-NPs and Vit. C	ns	0.5990

Discussion

Radiation can affect a wide range of tissues, especially those with high rates of cell division, leading to infection and necrosis as key factors in the damage caused by high doses of radiation (Stone, Coleman, Anscher, & McBride, 2003). Several physiological processes may also cause cell damage under irradiation, but the formation of oxygen free radicals following lipid peroxidation is likely a major part of this cascade of events. The reactive oxygen species (ROS) interact with cellular molecules, including DNA, lipids, and proteins(Juan, Pérez de la Lastra, Plou, & Pérez-Lebeña, 2021) .

The current paper clarifies that exposure to X-rays can result in decreased interferon-alpha (IFN-α) levels in rats exposed to 4 Gy (G2) and 6 Gy (G3) of radiation, as well as changes in the physiological response volume to oral gavage of ZnO-nano and vitamin C supplementation in groups G4 (4 Gy) and G5 (6 Gy), probably due to radiation-induced immune system alterations. This decrease may be part of a broader spectrum of immune system changes, where high doses of ionizing radiation may lead to immunosuppressive outcomes. Ionizing radiation, including X-rays, interacts with the immune system in complex ways, impacting various cells and soluble factors. (Al-Qabandi & Alshammary, 2022).

IFN-α is a type of cytokine known for its role in modulating the immune system and inducing antiviral innate immune responses. It also plays a role in antitumor activity (Li, Liu, Zhou, & Su, 2009), as well as in inflammation that can disrupt the normal functioning of the immune system, potentially leading to a decrease in IFN-α production (Ryff & Pestka, 2013). Low doses of

ionizing radiation may cause subtle changes in immune function, while higher doses are more likely to be immunosuppressive. (Rückert, Flohr, Hecht, & Gaipl, 2021).

The effect of mixed ZnO-nano and Vitamin C supplementation on interferon-alpha (IFN-a) levels in female rats exposed to X-ray radiation has not been immediately studied. However, this research shows that both ZnO-nano and Vitamin C supplementation can provide radioprotective effects, and they work synergistically. Vitamin C has been proven to protect against radiation-induced harm, while ZnO-nano can reduce oxidative stress and inflammation associated with radiation. Co-administration of dietary ZnO-nano and Vitamin C supplementation should likely enhance these protective effects, such as the regulation of IFN-a, which is involved in the immune response to radiation. (Ali, Sari, Nowruzi, & Porzani, 2024) .

Conclusion:

From the results obtained, high-dose X-ray exposure can cause cell damage and infection, which could disrupt the regular functioning of the immune system, doubtlessly leading to a decrease in IFN-α production. Although there is no direct examination of diet ZnO-nano and Vitamin C supplementation on IFN-α levels after X-ray radiation, this paper suggests that their combined use may offer significant radioprotective benefits. This is likely due to the individual antioxidant and anti-inflammatory properties of both substances, and possibly through synergistic interactions that impact the immune response, including IFN-α levels.

References

Nasiri, B. (2023). Immunomodulation Strategies in Vascular Tissue Engineering: Monocyte Recruitment for Improved Endothelialization and Regeneration of Acellular Tissue-Engineered Vessels, State University of New York at Buffalo.

Salkowski, C. A., et al. (1995). "Effect of liposome-mediated macrophage depletion on LPS-induced cytokine gene expression and radioprotection." The Journal of Immunology 155(6): 3168-3179. http://doi.org/10.4049/jimmunol.155.6.3168.

Dawood, A. (2021). Immune System Modulation by Low-Dose Ionizing Radiation. http://hdl.handle.net/11375/27073

Lee Chung, B. (2017). Theranostic Nanoparticles for Managing Inflammatory Diseases and Conditions, Massachusetts Institute of Technology. http://hdl.handle.net/1721.1/112504.

Salkowski, C. A., et al. (1995). "Effect of liposome-mediated macrophage depletion on LPS-induced cytokine gene expression and radioprotection." The Journal of Immunology 155(6): 3168-3179. https://doi.org/10.4049/jimmunol.155.6.3168.

Sharma, P. (2019). Application of ZnO Nanowires for Intracellular Delivery of Biomacromolecules and Cancer Immunotherapy, Seoul National University Graduate School. https://hdl.handle.net/10371/162261.

Pehlivan, F. E. (2017). "Vitamin C: An Antioxidant Agent." Vitamin C 2: 23-35. http://dx.doi.org/10.5772/66058

SAINI, S. (2020). Effect of Zinc Oxide Nanoparticles on Growth, Fruit Yield, and Quality Attributes of Strawberry (Fragaria x ananassa Duch.), Dr. Yashwant Singh Parmar University of Horticulture and Forestry.

Al-Temimei, F. A., et al. (2024). "A DFT Study of Cenobamate and Its New Isomers as Effective Medical Treatments for Epilepsy." Ukrainian Journal of Physics 69(5): 314-314.

Ali, N. H., et al. (2024). "Evaluation of Cold Plasma Treatment Technology in Biosynthesized Silver Nanoparticles Encapsulated With Chitosan by Aliinostoc Persicum SA14 Against HepG-2." The Microbe 4: 100148. https://doi.org/10.1016/j.microb.2024.100148

Kumar, A. H., and A. J. Clover (2015). "Intraperitoneal Co-Administration of Low-Dose Urethane With Xylazine and Ketamine for Extended Duration of Surgical Anesthesia in Rats." Laboratory Animal Research 31(4): 174-179. https://doi.org/10.5625/lar.2015.31.4.174

Hanley, J. P., and G. H. Haydon (1998). "The Biology of Interferon-α and the Clinical Significance of Anti-Interferon Antibodies." Leukemia & Lymphoma 29(3-4): 257-268. https://doi.org/10.3109/10428199809068563.

Stone, H. B., et al. (2003). "Effects of Radiation on Normal Tissue: Consequences and Mechanisms." The Lancet Oncology 4(9): 529-536.

Al-Qabandi, M., and J. Alshammary (2022). Ionizing Radiation: Biological Effects and Essential Cell Biology. The Pathophysiologic Basis of Nuclear Medicine, Springer: 11-37. https://doi.org/10.1007/978-3-030-96252-4_2.

Ryff, J.-C., and S. Pestka (2013). Interferons and Interleukins. Pharmaceutical Biotechnology: Fundamentals and Applications, Springer: 413-437. https://doi.org/10.1007/978-1-4614-6486-0_21

Rückert, M., et al. (2021). "Radiotherapy and the Immune System: More Than Just Immune Suppression." Stem Cells 39(9): 1155-1165. https://doi.org/10.1002/stem.3391

Ali, N. H., et al. (2024). "Evaluation of Cold Plasma Treatment Technology in Biosynthesized Silver Nanoparticles Encapsulated With Chitosan by Aliinostoc Persicum SA14 Against HepG-2." The Microbe 4: 100148.

G-2." The Microbe **4**: 100148. https://doi.org/10.1016/j.microb.2024.100148.

The Lomax (Pareto Type II) Distribution Shape Parameter Bayesian estimation under [Singly Type II Censored Samples]

Moslem A. S. Qasim[1]

[1]Directorate General of Education in Holy Karbala Province, Al-Khandaq International School,

Email_muslim.abed@yahoo.com

م.م. مسلم عبد الستار قاسم – المديرية العامة لتربية كربلاء المقدسة

Abstract:

This study employed a Bayesian estimation of the shape parameter (ϑ) of the Lomax distribution (also known as Pareto Type II) under a revised version of the singularly censored sample method-firstly,using non-informative prior and secondly,using an informative prior **[Quasi and Exponential]**;where three different loss functions **[Quadratic**(**QLF**),**Degroot** (**DLF**), **and Precautionary**(**PLF**)**]**were used six simulation experiments were conducted at various sample sizes.The results from each trial were then compared using the mean squared error[M.S.E.] criterion.

1.Introduction:

In many different circumstances, the Lomax (1954)[12]. A Pareto distribution of type II, also called Lomax, was originally developed for the statistical modeling of commercial failures. However, it has evolved to model reliability, life-testing, and in the medical field, as well as the size distribution of files stored on server computers. The Lomax distribution has proved useful for

developing new classes of distributions and for being the basis of many generalizations that involve adding parameters to a well-established class of distributions,[11]. D.K. Dey estimated the Lomax distribution's parameters and reliability function (complex life) from complete and type (II) censored samples in (1992)[6]. In 2002, Hatem A.Howlader applied Lindlley's theory to Bayesian estimate of the survival function Lomax distribution[8]. In (2011), Panahi.A.computed the (stress-strength),parameter p(y<x), where y and x are independent and both have a Lomax distribution.[14].In (2015),Dr. Nadia AL-Noor looked into an evaluation on (Lomax) the estimation of parameters by employing various methods of Bayesian analysis and non-Bayesian estimation techniques such as non-Bayesian Maximum Likelihood Estimation (MLE)[1]. Also, an opportunity was afforded through this paper to implement a parametric estimation procedure on the shape (ϑ) of the Lomax distribution, assuming that the scale parameter (β) was known and equal to 2. As such, the following presents the results of the analysis conducted.

The objective of the study. Here the Bayes approach was utilized to obtain the shape parameter(ϑ),for the Lomax probability distribution; through **[Quadratic (QLF),Degroot(DLF),precautionary(PLF)]**loss functions with Priors:**[Quasi and Exponential]** functions and used the mean square error or (MSE) to determine which prior function performed best with respect to the loss function yielded by the simulations used to obtain an optimal estimate for the shape estimator(ϑ), for the Lomax distribution(L.D).

2.Aim of research:

The goal of this study is to identify a superior estimator based on the mean square error(M.S.E.)criterion, for the shape parameter (ϑ) of the Lomax distribution (L.D.), with two different prior functions and three different loss functions, using Type (II) censoring data.

3.Defintion of the distribution:

A vital lifetime distribution in survival analysis is the Lomax distribution which was first identified and described by Lomax in 1954[3]. The cumulative of this distribution (CDF) from an experiential perspective was published by[7]: $F(x;\vartheta,\beta) = 1 - \left(1+\frac{x}{\beta}\right)^{-\vartheta}$

Afterwards, the probability density function (PDF) is:

$$f(x;\vartheta,\beta) = \frac{\vartheta}{\beta}(1+\frac{x}{\beta})^{-(\vartheta+1)} \quad , \quad x > 0 \ \ and \ \ \vartheta,\beta > 0$$

Where is : (ϑ,β) are the shape and scale parameters respectively .

❖ *The characteristics of the Lomax (Pareto type II)distribution [12]:*

Here are several Lomax distribution(L.D),characteristics accordingly:

- Mean = $\frac{\beta}{\vartheta-1} \quad , \vartheta > 1$
- Median = $\beta(\sqrt[\vartheta]{2}-1)$
- variance → $V(X) = \frac{\vartheta\beta^2}{(\vartheta-1)^2(\vartheta-2)} \quad , \ \vartheta > 2$
- Mode = 0
- Standard deviation = $\frac{\sqrt{\vartheta}\beta}{(\vartheta-1)\sqrt{(\vartheta-2)}} \quad , \vartheta > 2$

- Skewnes = $\frac{2(1+\vartheta)}{(\vartheta-3)}\sqrt{\frac{\vartheta-2}{\vartheta}}$ $,\vartheta > 3$

- Kurtosis = $\frac{6(\vartheta^3+\vartheta^2-6\vartheta-2)}{\vartheta(\vartheta-3)(\vartheta-4)}$ $,\vartheta > 4$

- Coefficient of variance = $\sqrt{1-\frac{\vartheta}{2}}$ $,\vartheta \leq 2$

Simulating the scale parameter (β), in this study is recognized equal to(2).So the (PDF) and (CDF), respectively:

$$f(x;\vartheta) = \frac{\vartheta}{2}(1+\frac{x}{2})^{-(\vartheta+1)} \quad , \quad x > 0 \ and \ \vartheta > 0 \qquad \dots\dots(1)$$

$$F(x;\vartheta) = 1-\left(1+\frac{x}{2}\right)^{-\vartheta} \qquad \dots\dots(2)$$

4. Censored samples [10]:

There are some conditional limits on the number of samples we are able to test through life testing that would be impractical to do. Some of these limits could include monetary costs or sample quantity, meaning that we will either have to limit how much we spend during life testing or limit how many samples we test..

4.1. Singly type (II) censored samples [4]:

In cases where there are (n) units to be censored and we desire to censor (r) of those (n) units, such that(r < n),we will need to stop the testing to obtain the censoring of (r) units. The reason

being is that a random variable cannot be formed. The following is the(LF),Likelihood function for this one kind of samples accordingly

$$L_H(\vartheta|\underline{x}) = \left(\frac{n!}{(n-r)!}\right).\left(1-\mathbb{F}(x_r)\right)^{(n-r)}.\prod_{(i=1)}^{r}\mathfrak{f}(x_i,\vartheta) \qquad \dots\dots(3)$$

Such as : $0 < x_{(1)} < x_{(2)} < x_{(3)} \dots < x_{(r)} < \cdots < x_{(n-1)} < x_{(n)}$.

5. Standard Bayesian estimation:

So be it, $x_{(1)}, x_{(2)}, \dots, x_{(n)}$ iid. , $\mathfrak{f}(x;\vartheta)$, the posterior density allows you to revise your beliefs concerning the unknown parameter, (ϑ). In Bayesian methodology, the density for each data observation is treated as if it were a conditional density associated with the posterior. Due to calculating the posterior density we can update our beliefs related to the parameter (ϑ). The Bayesian perspective on each observation observed data contain the density as a conditional density. [9] as: $\varphi(\vartheta|\underline{x}) = \frac{L_H\,(\underline{x}|\vartheta)g(\vartheta)}{\int_0^\infty L_H(\underline{x}|\vartheta)\,g(\vartheta)\,d\vartheta}$ $\dots\dots(4)$

Such as : $L_H\,(\underline{x}|\vartheta)$, is the probability of a density function, and $g(\vartheta)$ is the function that stands before a shape parameter (ϑ).

6. The loss function[18]:

A loss function $L(\hat{\vartheta},\vartheta)$represents losses incurred when we estimate the parameter (ϑ) by $\hat{\vartheta}$. The loss functions using in this research as:

6.1. Quadratic- loss function(QLF) [16]:

Which is type is symmetric as provided by:

$$L(\hat{\vartheta},\vartheta)=\left(\frac{\hat{\vartheta}-\vartheta}{\vartheta}\right)^2$$

And estimate to the parameter using Bayesian methods (ϑ) as :

$$\hat{\vartheta}_q=\frac{E(\vartheta^{-1}|\underline{x})}{E(\vartheta^{-2}|\underline{x})} \quad \dots\dots(5)$$

6.2.Degroot– loss function(DLF)[15]:

Given that it is of the asymmetric type:

$$\mathrm{L}(\hat{\vartheta},\vartheta)=\left(\frac{\vartheta-\hat{\vartheta}}{\hat{\vartheta}}\right)^2$$

Then one that uses Bayes to estimate parameter (ϑ) as : $\hat{\vartheta}_D=$

$$\frac{E(\vartheta^2|\underline{x})}{E(\vartheta|\underline{x})} \quad \dots\dots(6)$$

6.3.Precautionary –loss function(PLF)[13]:

Additionally, that asymmetric kind is provided by:

$$L(\hat{\vartheta},\vartheta)=\frac{(\vartheta-\hat{\vartheta})^2}{\hat{\vartheta}}$$

So the Bayesian approach of estimating parameter (ϑ) as:

$$\hat{\vartheta}_P=\sqrt{E(\vartheta^2|\underline{x})} \quad \dots\dots(7)$$

7. Bayes analysis with a single type 2 sample with censoring:

For this kind of data, a likelihood function(LF),given by equation(3), may be found as :

- $\left(1-\mathrm{F}(x_r)\right)^{(n-r)}$, by eq.(2) we get :

$$\left(1-\mathrm{F}(x_r)\right)^{(n-r)}=\left[1-\left[1-(1+\frac{x_r}{2})^{-\vartheta}\right]\right]^{(n-r)}=\left[(1+\frac{x_r}{2})^{-\vartheta}\right]^{(n-r)}$$

$$= (1+\frac{x_r}{2})^{-\vartheta(n-r)} = e^{-\vartheta(n-r)\ln(1+\frac{x_r}{2})}$$

$$\therefore \left(1-\mathrm{F}(x_r)\right)^{(n-r)} = e^{-\vartheta(n-r)\ln(1+\frac{x_r}{2})} \quad \ldots\ldots(8)$$

Now to find $\prod_{i=1}^{r} f(x_i, \vartheta)$, by eq.(1) we get:

❖ $$\prod_{i=1}^{r} f(x_i, \vartheta) = \prod_{(i=1)}^{r}\left[\frac{\vartheta}{2}(1+\frac{x_i}{2})^{-(\vartheta+1)}\right]$$

$$= \frac{\vartheta^r}{2^r}\prod_{(i=1)}^{r}(1+\frac{x_i}{2})^{-(\vartheta+1)} = \frac{\vartheta^r}{2^r}\prod_{(i=1)}^{r} e^{-(\vartheta+1)\ln(1+\frac{x_i}{2})}$$

$$= \frac{\vartheta^r}{2^r} e^{-(\vartheta+1)\sum_{i=1}^{r}\ln(1+\frac{x_i}{2})} = \frac{\vartheta^r}{2^r} e^{-\vartheta\sum_{i=1}^{r}\ln(1+\frac{x_i}{2})} e^{-\sum_{i=1}^{r}\ln(1+\frac{x_i}{2})}$$

$$\therefore \prod_{(i=1)}^{r} f(x_i, \vartheta) = \frac{e^{-\Psi_1(x)}}{2^r}\,\vartheta^r e^{-\vartheta\Psi_1(x)} \quad \ldots\ldots(9)$$

Such that: $\Psi_1(x) = \sum_{i=1}^{r}\ln(1+\frac{x_i}{2})$

Substitute equations (8) and (9) in equation (3) we get:

$$L_H(\vartheta/\underline{x}) = \frac{n!}{(n-r)!}\, e^{-\vartheta(n-r)\ln(1+\frac{x_r}{2})}\, \frac{e^{-\Psi_1(x)}}{2^r}\, \vartheta^r e^{-\vartheta\Psi_1(x)}$$

$$= \frac{n!}{(n-r)!}\, \frac{e^{\Psi_1(x)}}{2^r}\, \vartheta^r\, e^{-\vartheta\left[(n-r)ln\left(1+\frac{x_r}{2}\right)+\Psi_1(x)\right]}$$

$$\therefore L_H(\vartheta/\underline{x}) = \Psi_2(x)\ \vartheta^r\, e^{-\vartheta\Psi_3(x)} \quad \ldots\ldots(10)$$

where: $\Psi_2(x) = \frac{n!}{(n-r)!}\, \frac{e^{-\Psi_1(x)}}{2^r}$

And $\Psi_3(x) = \left((n-r)ln\left(1+\frac{x_r}{2}\right)+\Psi_1(x)\right)$

7.1. The Quasi-Prior posterior distribution[17]:

The definition of the quasi-prior is:

$$g(\vartheta) = \frac{1}{\vartheta^t}\ ; \qquad \vartheta > 0,\ \ t > 0 \qquad \ldots\ldots(11)$$

By equations(10)and(11)are substituted in equation(4)to obtain a posterior distribution with quasi-prior.

$$\varphi_{s_Q}\left(\vartheta\middle|\underline{x}\right) = \frac{\Psi_2(x)\ \ \vartheta^{r-t}\ \ e^{-\vartheta\Psi_3(x)}}{\int_0^\infty \Psi_2(x)\ \ \vartheta^{r-t}\ \ e^{-\vartheta\Psi_3(x)} d\vartheta}$$

$$= \frac{\vartheta^{r-t}\ \ e^{-\vartheta\Psi_3(x)}}{\frac{\Gamma(r-t+1)}{(\Psi_3(x))^{r-t+1}}} \quad , \quad \therefore \varphi_{s_Q}\left(\vartheta\middle|\underline{x}\right) = \frac{(\Psi_3(x))^{r-t+1}}{\Gamma(r-t+1)}\ \theta^{r-t}\ \ e^{-\vartheta\,\Psi_3(x)} \qquad \ldots\ldots\ (12)$$

Where : $\varphi_{s_Q}\left(\vartheta\middle|\underline{x}\right) \sim Gamm.[r-t+1\,, \Psi_3(x)]$

All Bayes estimator to a shape parameter (ϑ), utilizing the three unlike functions of loss is expressed as follows:

7.1.1. ***Quadratic-loss function(QLF)****:*

From equation(5); estimate using Bayes for (ϑ) given by $(\hat{\vartheta}_{QQ_S})$, can be obtain as follows:

$$E\left(\vartheta^{-1}\middle|\underline{x}\right) = \int_0^\infty \vartheta^{-1}\ \varphi_{s_Q}\left(\vartheta\middle|\underline{x}\right) d\vartheta \qquad \ldots\ldots(13)$$

Substitute the equations (12) in equation (13), we get:

$$E\left(\vartheta^{-1}\middle|\underline{x}\right) = \int_0^\infty \vartheta^{-1}\ \frac{(\Psi_3(x))^{r-t+1}}{\Gamma(r-t+1)}\ \vartheta^{r-t}\ \ e^{-\vartheta\,\Psi_3(x)}\ \ d\vartheta$$

$$= \frac{(\Psi_3(x))^{r-t+1}}{\Gamma(r-t+1)} \int_0^\infty\ \vartheta^{r-t-1}\ \ e^{-\vartheta\,\Psi_3(x)}\ \ d\vartheta$$

$$= \frac{(\Psi_3(x))^{r-t+1}}{\Gamma(r-t+1)} \frac{\Gamma(r-t)}{(\Psi_3(x))^{r-t}} = \frac{\Psi_3(x)}{(r-t)} \quad \dots\dots(14)$$

$$And \quad E(\vartheta^{-2}|\underline{x}) = \int_0^{\infty} \vartheta^{-2} \varphi_{s_Q}(\vartheta|\underline{x}) d\vartheta \quad \dots\dots(15)$$

Substitute the equations (12) in equation (15), we get:

$$E(\vartheta^{-1}|\underline{x}) = \int_0^{\infty} \vartheta^{-2} \frac{(\Psi_3(x))^{r-t+1}}{\Gamma(r-t+1)} \vartheta^{r-t} e^{-\vartheta \Psi_3(x)} d\vartheta$$

$$= \frac{(\Psi_3(x))^{r-t+1}}{\Gamma(r-t+1)} \int_0^{\infty} \vartheta^{r-t-2} e^{-\vartheta \Psi_3(x)} d\vartheta$$

$$= \frac{(\Psi_3(x))^{r-t+1}}{\Gamma(r-t+1)} \frac{\Gamma(r-t-1)}{(\Psi_3(x))^{r-t-1}} = \frac{(\Psi_3(x))^2}{(r-t)(r-t-1)} \quad \dots\dots(16)$$

Then by equations (14 and 16); Here is the formula to the Bayes estimator of a shape parameter (ϑ):

$$\therefore \hat{\vartheta}_{QQ_S} = \frac{E(\vartheta^{-1}|\underline{x})}{E(\vartheta^{-2}|\underline{x})} = \frac{r-t-1}{\Psi_3(x)} \quad \dots\dots(17)$$

7.1.2.Degroot-loss function(DLF):

According to equation(6);estimate using Bayes for (ϑ) given by $(\hat{\vartheta}_{DQ_S})$, can be obtain as follows:

$$E(\vartheta^2|\underline{x}) = \int_0^{\infty} \vartheta^2 \varphi_{s_Q}(\vartheta|\underline{x}) d\vartheta \quad \dots\dots(18)$$

Substitute the equations (12) in equation (18), we get:

$$E(\vartheta^2|\underline{x}) = \int_0^{\infty} \vartheta^2 \frac{(\Psi_3(x))^{r-t+1}}{\Gamma(r-t+1)} \vartheta^{r-t} e^{-\vartheta \Psi_3(x)} d\vartheta$$

$$= \frac{(\Psi_3(x))^{r-t+1}}{\Gamma(r-t+1)} \int_0^{\infty} \vartheta^{r-t+2} e^{-\vartheta \Psi_3(x)} d\vartheta$$

$$= \frac{(\Psi_3(x))^{r-t+1}}{\Gamma(r-t+1)} \frac{\Gamma(r-t+3)}{(\Psi_3(x))^{r-t+3}} = \frac{(r-t+2)(r-t+1)}{(\Psi_3(x))^2} \quad \dots\dots(19)$$

$$And \quad E(\vartheta|\underline{x}) = \int_0^\infty \vartheta \ \varphi_{s_Q}(\vartheta|\underline{x}) \, d\vartheta \quad \dots\dots(20)$$

Substitute the equations (12) in equation (20), we get:

$$E(\vartheta|\underline{x}) = \int_0^\infty \vartheta \ \frac{(\Psi_3(x))^{r-t+1}}{\Gamma(r-t+1)} \ \vartheta^{r-t} \ e^{-\vartheta \Psi_3(x)} \ d\vartheta$$

$$= \frac{(\Psi_3(x))^{r-t+1}}{\Gamma(r-t+1)} \int_0^\infty \vartheta^{r-t+1} \ e^{-\vartheta \Psi_3(x)} \ d\vartheta$$

$$= \frac{(\Psi_3(x))^{r-t+1}}{\Gamma(r-t+1)} \ \frac{\Gamma(r-t+2)}{(\Psi_3(x))^{r-t+2}} = \frac{(r-t+1)}{\Psi_3(x)} \quad \dots\dots(21)$$

By equations (19 and 21); then provide the following to the Bayes estimated of a shape parameter (ϑ) as:

$$\therefore \hat{\vartheta}_{DQ_S} = \frac{E(\vartheta^2|\underline{X})}{E(\vartheta|\underline{X})} = \frac{r-t+2}{(\Psi_3(x))} \quad \dots\dots(22)$$

7.1.3.Precautionary-loss function(PLF):

Using the equation(7), estimate using Bayes for (ϑ) given by $(\hat{\vartheta}_{PQ_S})$, can be obtain as follows:

$$E(\vartheta^2|\underline{x}) = \int_0^\infty \vartheta^2 \ \varphi_{s_Q}(\vartheta|\underline{x}) \, d\vartheta \quad \dots\dots(23)$$

Substitute the equations (12) in equation (23), we get:

$$E(\vartheta^2|\underline{x}) = \int_0^\infty \vartheta^2 \ \frac{(\Psi_3(x))^{r-t+1}}{\Gamma(r-t+1)} \ \vartheta^{r-t} \ e^{-\vartheta \Psi_3(x)} \ d\vartheta$$

$$= \frac{(\Psi_3(x))^{r-t+1}}{\Gamma(r-t+1)} \int_0^\infty \vartheta^{r-t+2} \ e^{-\vartheta \Psi_3(x)} \ d\vartheta$$

$$= \frac{(\Psi_3(x))^{r-t+1}}{\Gamma(r-t+1)} \frac{\Gamma(r-t+3)}{(\Psi_3(x))^{r-t+3}} = \frac{(r-t+2)(r-t+1)}{(\Psi_3(x))^2} \quad \ldots\ldots(24)$$

By equation(24);then provide the following to the Bayes estimated of a shape parameter (ϑ) as:

$$\therefore \hat{\vartheta}_{PQ_S} = \sqrt{E(\vartheta^2|\underline{x})} = \left(\frac{(r-t+2)(r-t+1)}{(\Psi_3(x))^2}\right)^{\frac{1}{2}} \quad \ldots\ldots(25)$$

7.2. The Exponential–Prior posterior distribution [2]:

The previous exponential is defined as:

$$g(\vartheta) = \mu e^{-\mu\vartheta} \quad , \quad \mu, \vartheta > 0 \quad \ldots\ldots(26)$$

By equations(10)and(26)are substituted in equation(4)to obtain a posterior distribution with Exponential -prior.

$$\varphi_{S_E}(\vartheta|\underline{x}) = \frac{\mu\Psi_2(x)\ \vartheta^r\ e^{-\vartheta(\mu+\Psi_3(x))}}{\int_0^\infty \mu\Psi_2(x)\ \vartheta^r\ e^{-\vartheta(\mu+\Psi_3(x))}d\vartheta}$$

$$= \frac{\vartheta^r\ e^{-\vartheta(\mu+\Psi_3(x))}}{\frac{\Gamma(r+1)}{(\mu+\Psi_3(x))^{r+1}}}$$

$$\therefore \varphi_{S_E}(\vartheta|\underline{x}) = \frac{(\mu+\Psi_3(x))^{r+1}}{\Gamma(r+1)}\ \vartheta^r\ e^{-\vartheta(\mu+\Psi_3(x))} \quad \ldots\ldots(27)$$

Such that : $\varphi_{S_E}(\vartheta|\underline{x}) \sim Gamm\,[r+1, \mu+\Psi_3(x)]$

All Bayes estimator to a shape parameter (ϑ), utilizing the three unlike functions of loss is expressed as follows:

7.2.1. Quadratic–loss function(QLF):

From equation(5);estimate using Bayes for (ϑ) given by $(\hat{\vartheta}_{QE_S})$, can be obtain as follows:

$$E\left(\vartheta^{-1}|\underline{x}\right) = \int_0^{\infty} \vartheta^{-1}\ \varphi_{s_E}\left(\vartheta\middle|\underline{x}\right) d\vartheta \qquad \ldots\ \ldots (28)$$

Substitute the equations (27) in equation (28), we get:

$$E\left(\vartheta^{-1}\middle|\underline{x}\right) = \int_0^{\infty} \vartheta^{-1}\ \frac{(\mu+\Psi_3(x))^{r+1}}{\Gamma(r+1)}\ \vartheta^{r}\ \ e^{-\vartheta(\mu+\Psi_3(x))}\ d\vartheta$$

$$= \frac{(\mu+\Psi_3(x))^{r+1}}{\Gamma(r+1)} \int_0^{\infty}\ \vartheta^{r-1}\ \ e^{-\vartheta(\mu+\Psi_3(x))}\ d\vartheta$$

$$= \frac{(\mu+\Psi_3(x))^{r+1}}{\Gamma(r+1)}\ \ \frac{\Gamma(r)}{(\mu+\Psi_3(x))^{r}} = \frac{\mu+\Psi_3(x)}{r} \qquad \ldots\ \ldots (29)$$

$$And \qquad E\left(\vartheta^{-2}|\underline{x}\right) = \int_0^{\infty} \vartheta^{-2}\ \varphi_{s_E}\left(\vartheta\middle|\underline{x}\right) d\vartheta \qquad \ldots\ \ldots (30)$$

Substitute the equations (27) in equation (30), we get:

$$E\left(\vartheta^{-2}\middle|\underline{x}\right) = \int_0^{\infty} \vartheta^{-2}\ \frac{(\mu+\Psi_3(x))^{r+1}}{\Gamma(r+1)}\ \vartheta^{r}\ \ e^{-\vartheta(\mu+\Psi_3(x))}\ d\vartheta$$

$$= \frac{(\mu+\Psi_3(x))^{r+1}}{\Gamma(r+1)} \int_0^{\infty}\ \vartheta^{r-2}\ \ e^{-\vartheta(\mu+\Psi_3(x))}\ d\vartheta$$

$$= \frac{(\mu+\Psi_3(x))^{r+1}}{\Gamma(r+1)}\ \ \frac{\Gamma(r-1)}{(\mu+\Psi_3(x))^{r-1}} = \frac{(\mu+\Psi_3(x))^{2}}{r(r-1)} \qquad \ldots\ \ldots (31)$$

Then by equations (29 and 31); Here is the formula to the Bayes estimator of a shape parameter (ϑ) as:

$$\therefore \hat{\vartheta}_{QE_S} = \frac{E\left(\vartheta^{-1}\middle|\underline{x}\right)}{E\left(\vartheta^{-2}\middle|\underline{x}\right)} = \frac{r-1}{\mu+\Psi_3(x)} \qquad \ldots\ \ldots (\ 32\ )$$

7.2.2.Degroot-loss function(DLF):

From equation(6); estimate using Bayes for (ϑ) given by ($\hat{\vartheta}_{DE_S}$), can be obtain as follows:

$$E\left(\vartheta^2|\underline{x}\right) = \int_0^\infty \vartheta^2 \ \varphi_{s_E}\left(\vartheta|\underline{x}\right) d\vartheta \quad \ldots\ldots(33)$$

Substitute the equations (27) in equation (33), we get:

$$E\left(\vartheta^2|\underline{x}\right) = \int_0^\infty \vartheta^2 \ \frac{(\mu+\Psi_3(x))^{r+1}}{\Gamma(r+1)} \ \vartheta^r \ e^{-\vartheta(\mu+\Psi_3(x))} \ d\vartheta$$

$$= \frac{(\mu+\Psi_3(x))^{r+1}}{\Gamma(r+1)} \int_0^\infty \vartheta^{r+2} \ e^{-\vartheta(\mu+\Psi_3(x))} \ d\vartheta$$

$$= \frac{(\mu+\Psi_3(x))^{r+1}}{\Gamma(r+1)} \ \frac{\Gamma(r+3)}{(\mu+\Psi_3(x))^{r+3}} = \frac{(r+2)(r+1)}{(\mu+\Psi_3(x))^2} \quad \ldots\ldots(34)$$

$$And \quad E\left(\vartheta|\underline{x}\right) = \int_0^\infty \vartheta \ \varphi_{s_E}\left(\vartheta|\underline{x}\right) d\vartheta \quad \ldots\ldots(35)$$

Substitute the equations (27) in equation (35), we get:

$$E\left(\vartheta|\underline{x}\right) = \int_0^\infty \vartheta \ \frac{(\mu+\Psi_3(x))^{r+1}}{\Gamma(r+1)} \ \vartheta^r \ e^{-\vartheta(\mu+\Psi_3(x))} \ d\vartheta$$

$$= \frac{(\mu+\Psi_3(x))^{r+1}}{\Gamma(r+1)} \int_0^\infty \vartheta^{r+1} \ e^{-\vartheta\,(\mu+\Psi_3(x))} \ d\vartheta$$

$$= \frac{(\mu+\Psi_3(x))^{r+1}}{\Gamma(r+1)} \ \frac{\Gamma(r+2)}{(\mu+\Psi_3(x))^{r+2}} = \frac{(r+1)}{\mu+\Psi_3(x)} \quad \ldots\ldots(36)$$

By equations (34and 36); then provide the following to the Bayes estimated of a shape parameter (ϑ) as:

$$\therefore \hat{\vartheta}_{DE_S} = \frac{E\left(\vartheta^2|\underline{x}\right)}{E\left(\vartheta|\underline{x}\right)} = \frac{r+2}{\mu+\Psi_3(x)} \quad \ldots\ldots(37)$$

7.2.3.Precautionary–loss function(PLF):

Using the equation(7), estimate using Bayes for (ϑ) given by $(\hat{\vartheta}_{PE_S})$, can be obtain as follows:

$$E\left(\vartheta^2|\underline{x}\right) = \int_0^\infty \vartheta^2 \ \varphi_{s_E}\left(\vartheta|\underline{x}\right) d\vartheta \quad \ldots\ldots(38)$$

The Exp.	ϑ	μ

Substitute the equations (27) in equation (23), we get:

$$E\left(\vartheta^2\middle|\underline{x}\right) = \int_0^\infty \vartheta^2 \ \frac{(\mu+\Psi_3(x))^{r+1}}{\Gamma(r+1)} \ \vartheta^r \ e^{-\vartheta(\mu+\Psi_3(x))} \ d\vartheta$$

$$= \frac{(\mu+\Psi_3(x))^{r+1}}{\Gamma(r+1)} \int_0^\infty \vartheta^{r+2} \ e^{-\vartheta\,(\mu+\Psi_3(x))} \ d\vartheta$$

$$= \frac{(\mu+\Psi_3(x))^{r+1}}{\Gamma(r+1)} \ \frac{\Gamma(r+3)}{(\mu+\Psi_3(x))^{r+3}} = \frac{(r+2)(r+1)}{(\mu+\Psi_3(x))^2} \qquad \ldots\ldots(40)$$

By equation(40);then provide the following to the Bayes estimated of a shape parameter (ϑ) as:

$$\therefore \hat{\vartheta}_{PE_S} = \sqrt{E\left(\vartheta^2\middle|\underline{x}\right)} = \left(\frac{(r+2)(r+1)}{(\mu+\Psi_3(x))^2}\right)^{\frac{1}{2}} \qquad \ldots\ldots(41)$$

8. Discussion of Simulation:

To find the best estimator for the shape parameter (ϑ),of the Lomax distribution(L.D) ,using simulation techniques were used on different sample sizes (small n=15, medium n=65, and large n=100) in six experiments, where each experiment was repeated (T=1000), using (CDF), it is Equation (2), to generate different random values(X_i), V=F(X_i), with (V) being a random variable in the interval (0,1), Where: $x_i = 2\left[(1-V)^{\frac{-1}{\vartheta}} - 1\right]$ ……(42)

Here, the Monte- Carlo method [5], was used to generate random data according to the values of (r=5,45and 95),and (t=1.5),and the default values used in Table (1) below.

***Table1**: The parameters the initial settings* (ϑ, μ)

1	*0.5*	*3*
2	*0.5*	*5*
3	*1.5*	*3*
4	*1.5*	*5*
5	*2.5*	*3*
6	*2.5*	*5*

Next, using (M.S.E.),their best estimation to a shape parameter (ϑ), is compared as follows:

(MSE $\hat{\vartheta}$) = $\frac{1}{T}\sum_{i=1}^{n}\left(\hat{\vartheta}-\vartheta\right)^2$ ……(43) As an

T=[1000], with(M.S.E.),to estimators using equations:(17),(22),(25),(32),(37) and (41), as seen in the tables below:

n , r	***Quasi-prior.***	***The Best***

Table2*:(M.S.E.) to estimate*(ϑ), *for L.D./ Exp.1*

Such that*:* $\boldsymbol{\vartheta = 0.5\ ,\ \mu = 3}$

	Q_Q	D_Q	P_Q	
15 , 5	*0.0639*	*0.1819*	*0.1344*	Q_Q
65 , 45	*0.0055*	*0.0063*	*0.0060*	Q_Q
100 , 95	*0.0025*	*0.0026*	*0.0025*	Q_Q, P_Q
	Exponential–prior.			
	Q_E	D_E	P_E	
15 , 5	*1.1325*	*1.4991*	*1.4847*	Q_E
65 , 45	*1.0986*	*1.1195*	*1.1160*	Q_E
100 , 95	*0.9351*	*0.9795*	*0.9720*	Q_E

Table3:*(M.S.E.)to estimate*(ϑ), *for L.D. / Ex.2*

Such that: $\vartheta = 0.5$, $\mu = 5$

n , r	***Quasi–prior***.	***The Best***

Table4:*(M.S.E.)to estimate*(ϑ) , *for L.D./ Exp.3*

Such that: $\vartheta = 1.5$, $\mu = 3$

	Q_Q	D_Q	P_Q	
15 , 5	*0.2006*	*2.2774*	*1.8138*	Q_Q
65 , 45	*0.0584*	*0.8067*	*0.7617*	Q_Q
100 , 95	*0.0233*	*0.0254*	*0.0233*	Q_Q ,P_Q
	Exponential–prior.			
	Q_E	D_E	P_E	
15 , 5	*0.3896*	*2.6098*	*2.0824*	Q_E
65 , 45	*0.0929*	*1.1598*	*1.1485*	Q_E
100 , 95	*0.0687*	*0.8555*	*0.8242*	Q_E

Table5:*(M.S.E.)to estimate*(ϑ), *for L.D./ Exp.4*

n , r	***Quasi–prior***.			***The Best***
	Q_Q	D_Q	P_Q	
15 , 5	*2.8965*	*3.4548*	*3.8328*	Q_Q
65 , 45	*1.0375*	*1.5596*	*1.4639*	Q_Q
100 , 95	*0.0659*	*0.0684*	*0.0671*	Q_Q
	Exponential–prior.			
	Q_E	D_E	P_E	
15 , 5	*0.5950*	*0.8950*	*0.0211*	P_E
65 , 45	*0.3816*	*0.2006*	*0.0458*	P_E

Such that: $\vartheta = 1.5$, $\mu = 5$

100 , 95	*0.1527*	*0.1377*	*0.0150*	P_E

n , r	***Quasi–prior***.			***The Best***
	Q_Q	D_Q	P_Q	
15 , 5	*2.5635*	*2.6104*	*4.5598*	Q_Q
65 , 45	*1.3676*	*1.8283*	*1.7463*	Q_Q
100 , 95	*0.0261*	*0.0255*	*0.0255*	D_Q , P_Q
	Exponential–prior.			
	Q_E	D_E	P_E	
15 , 5	*0.0231*	*0.0648*	*0.0231*	Q_E , P_E
65 , 45	*0.0294*	*0.0477*	*0.0199*	P_E
100 , 95	*0.0189*	*0.0261*	*0.0098*	P_E

Table6:*(M.S.E.)to estimate* (ϑ), *for L.D,/ Exp.5*

Such that: $\vartheta = 2.5$, $\mu = 3$

n , r	***Quasi-prior***.			***The Best***
	Q_Q	D_Q	P_Q	
15 , 5	*4.7742*	*3.0786*	*2.4951*	P_Q
65 , 45	*3.6718*	*2.9341*	*1.7093*	P_Q
100 , 95	*0.0781*	*0.0720*	*0.0705*	P_Q
	Exponential-prior.			
	Q_E	D_E	P_E	

Table7*:(M.S.E.)to estimate* (ϑ), *for L.D./Exp.6*

Such that*:* $\vartheta = 2.5$, $\mu = 5$

15 , 5	*1.5709*	*1.4068*	*1.2260*	P_E
65 , 45	*0.9935*	*0.2464*	*0.1696*	P_E
100 , 95	*0.7694*	*0.1350*	*0.0240*	P_E

Where:

Q_Q: The loss function is ***Quadratic***, with ***Quasi-prior***.

D_Q : The loss function is ***Degroot***, with ***Quasi-prior***.

P_Q: The loss function is ***precautionary***, with ***Quasi-prior***.

Q_E: The loss function is ***Quadratic***, with ***Exponential-prior***.

D_E : The loss function is ***Degroot***, with ***Exponential-prior***.

P_E: The loss function is ***precautionary***, with ***Exponential-prior***.

9.Conclusions:

Results from Tables(2,3and4),for all three experiments(1,2 and 3),show that the Bayes estimator for shape parameter(ϑ) has a minimal mean square error (M.S.E.) when using a **Quadratic** loss function with a sample size of (n=15) and (n=65); however, when using (n=100) there is also a minimum mean square error using **Quadratic and Precautionary** loss functions. In Table (5), for experiment number (4),it appears that the optimal Bayes estimator based on a **Quadratic** and **Precautionary** loss functions is when (n=15), and under **Precautionary** (n=65) and (n=100). Tables (6 and 7), from Experiment (5) and Experiment (6), indicate that in general the optimal

Bayes estimator for the shape parameter (ϑ) under type II single censoring will always be based on a **Precautionary** loss function, regardless of whether the sample size used for estimating the Bayes estimator is n=15, n=65, and n=100.

References:

[1] Al - Noor Nadia H. and S. S. Akwan,(2015), "Non - Bayes and Empirical Bayes estimators for the shape parameter of Lomax distribution", Mathematical theory and modelling, Vol.5, No.2, ISSN:2224 – 5804.

[2] A.F.Saieed(2012), "Maximum likelihood and Bayes estimation under generalized order statistics" ,Applied Math. Sciences Journal Vol. 6 , No. 49.

[3] A.M. Hamad and B.B. Salam,(2021), "Different Estimation Methods of the Stress-Strength Reliability Restricted Exponentiated Lomax Distribution" Mathematical Modelling of Engineering problems, Vol. 8, No. 3, pp. 477-484.

[4] Andrade, Thiago, Rodrigues, B.M and C.G (2015), "The Exponentiated Generalized Gumbel Distribution" Volume 38, Issue 1, pp. 123 -143.

[5] Bulut Y.M.,Dogru F.Z., and Asrslan O.,Alpha,(2021),"power Lomax distribution properties and application" ,journal of Reliability and statistical Studies, Vol.14 , 17-32.

[6] Day.D.K.,(1992), "Bayes compution parameter life testing and reliability estimation", Browse Journals of magazines , Vol.4, no:4, pp. 621 – 626 .

[7] Hamdy,M.Salem, (2014), "The Exponential Lomax distribution different Estimation methods", American Journal of Applied Mathematics and Statistics, p: 364 – 368 .

[8] Hawleder, Hatem A. and Hassan Anwar, (2002), "Bayesian Survival estimation of Pareto dist. Of the second kind based on failure censored data analysis", pp.301 – 314.

[9] Jayanta ,K.G.Mohan, D, and Tapas,S.(2006), "An introduction to Bayesian analysis theory and methods" ,/Springer Science+Business media/New York.USA.

[10] Kasim, Ahmed (2014), "Bayes Estimators of the Shape parameter of Exponentiated Rayleigh Distribution" Master thesis, Department of Mathematics, Al-Mustansiriyah University.

[11] Kumar, Shestha ,(2014), "Bayesian analysis of extended Lomax dist.", Int. Jour. Of mathematical trands and technology, Vol.7,No.1. **[12]** Lomax K.S.,(1954), "Business Failure another example of the analysis data", JASA, No.49, pp. 847 – 852.

[13] Nadarajah ,Saralees and Sumuel Kotz (2004) "The Bata Gumbel Distribution" Comm .stat.,No.4 .

[14] Panahi, H. and Asadi, S. (2011), "Inference of stress – strength model for Lomax dist."Engineering and technology, International Jour. Of Mathematical computational physical electrical, Vol.5 No.7 .

[15] Rezooky ,Awatif ,(2016), " Bayes Reliability Estimation for Lomax Distributions " International Journal of Advanced Scientific and Technical Research ,Issue 6, Vol 4, p:78-92

[16] Rostami, Mohammad and Bakri, Mohd,(2013), "Analyses of Prior Selections for Gumbel Distribution "Department of Mathematical Sciences, Volume 29, Number 1, 95–107.

[17] Sindhu, T.N., Feroze, N. and Aslam M.,(2013), "Bayesian Analysis of the Kumaraswamy Distribution under Failure Censoring Sampling Scheme" International Journal of Advanced Science and Technology, Vol. 51, 39-58.

[18]Surles ,J.G.and Padgett,W.J.,(2001),"Inference for reliability and stress strength for a scale Burr Type x distribution"/Lifetime data analysis, Vol.7, p 187-200.

برعاية كريمة واشراف السادة الافاضل

الأستاذ الدكتور أسامة إسماعيل المشهداني رئيس جامعة نينوى.
الأستاذ الدكتور كوسار محمد علي رئيس جامعة السليمانية.
الأستاذ الدكتور وسام صلاح عبد الحسين رئيس جامعة قرطبة.
الأستاذ الدكتور حاتم هذال عبدالحميد مدير عام دائرة البحوث والدراسات.
الأستاذ رباح إبراهيم آل جعفر مدير عام دائرة التعليم الديني والدراسات الإسلامية.
الأستاذ الدكتور صالح عبد المهدي الخالدي عميد كلية ابن خلدون الجامعة.
الأستاذة الدكتورة سوزان صابر حيدر عميد كلية الإدارة والاقتصاد - جامعة السليمانية.
الدكتور علي مهدي كاظم عميد كلية العلوم - جامعة قرطبة.
الدكتور علاء ثابت جاسم رئيس مؤسسة أجيال الرافدين لتطوير التعليم.
الأستاذ المساعد الدكتور علي عبودي نعمة المدير التنفيذي لمؤسسة أجيال الرافدين لتطوير التعليم.
الدكتور أحمد جميل مجيد المدرس مدير مركز وعي للاستشارات وبناء القدرات.

الرقيم السومري
للنشر والتوزيع
Scriptum Synthesis Publisher (SSSP)

+964 0777 52 62 892
IRAQ - DAIYALA - BAGHUBA
ISBN: 978-9922-7961-61
email : manager@sss-publisher.com
https://doi.org/10.62909/978.9922.7961.61
Sumerian scriptum synthesis publisher (SSSP)